Laboratoire Charles Fabry
Institut d'Optique
Ecole doctorale Ondes et Matière

THÈSE

pour l'obtention du grade de Docteur en sciences de l'Université Paris XI

présentée par

Fred JENDRZEJEWSKI

Quantum transport of ultracold atoms in disordered potentials:

Anderson Localization in three dimensions

Coherent Backscattering

thèse soutenue le 6 Novembre 2012 devant le jury composé de :

M. Frédéric Chevy	Rapporteur
M. Robin Kaiser	Rapporteur
M. Pierre Pillet	Examinateur
M. Immanuel Bloch	Examinateur
M. Philippe Bouyer	Directeur de thèse
M. Vincent Josse	Examinateur
M. Alain Aspect	Membre invité
M. Laurent Sanchez-Palencia	Membre invité

Remerciements

There are so many people that made the last three years possible that it will be impossible for me to give them all the attention they merit. So, I will start it was a huge thank you to everyone I worked with during the last three years. Thanks to their support, I was introduced into the scientific way of life and it was a blast.

The CNRS was kind enough to support my PhD work financially, which allowed me to get my feet wet in the field of fundamental research. I had to great pleasure to make this first experience in the very professional environment of the Atom Optics group at the Laboratoire Fabry at the Institut Optique. The group leaders, Alain Aspect and Patrick Bouyer, have built up a group, which breathes the passion for experimental physics.

During this time I learned a lot, most importantly that I am probably wrong whenever I think that I understood my experiments "well". At the beginning of my PhD I was naive enough to think that things would work the way they are supposed to work. In the end they did, but I had no idea of how to difficult it is to get our experiments working properly. Luckily, I had a great team of teachers in Alain Bernard and Patrick Cheinet that thought me a lot of the things I know about now. Patricks love for details and Alains' creative solutions for fixing things, which often enough involved some paper and scotch tape, are attributes I really learned to appreciate.

And if even Alain and Patrick would have some doubts, we had our team leader Vincent Josse. Vincent guided the evolution of this experiment and my studies with a lot of personal investment. Vincent has a lot of the properties, I now think are essential for being a great physicist. He teached me the patience it takes to get the experiment running properly and to find a clean signature of the things that were going on. His impressive ability to explain complicated things in an intuitive way, has helped me a lot in order to understand what we were doing. This drive to explain things in a pedagogical way also made it a pleasure to write down to the results we had obtained. Alain Aspect and Vincent, teached us younger team members how to write clear papers.

Unfortunatly, Alain and Patrick had to leave the team, when the most exiting results started come in. It was a pleasure to have Kilian joining our team. He was a great partner, who never lost his calm and kindness, even after months of problems. But the team "Pince" is only a tiny part of the big Atom Optics group with all its great permanent members and fun to be with PhD students.

Additionally to my first experience in research, I teached for my first time at the Institut d'Optique. I thank all my collaborators from the Polarization and Electronics team for the great team spirit and their patience with me.

Finally I have to thank my family and friends. Given the energy it takes to do a PhD, I would not have been able to go through with it without the help of my wife, my family and my friends. They allowed me get the necessary distance after some intense weeks of work and come back with fresh enthusiasm.

Contents

1 Introduction **9**

2 Wave propagation in disorder **15**
2.1 Interference and disorder . . . 15
2.1.1 Interferences in electron transport in disordered media . . . 16
2.2 From weak localization... . . . 17
2.2.1 Experiments on weak localization and backscattering . . . 19
2.3 ... to the suppression of transport - Anderson Localization . . . 20
2.3.1 Experiments on Anderson Localization . . . 22
2.4 Experiments with ultracold atoms . . . 23
2.5 Conclusion - Towards higher dimensions and interacting bosons . . . 24

3 Production of coherent matter waves **25**
3.1 Generalities about Bose-Einstein condensates . . . 25
3.1.1 Bose-Einstein condensation and the Gross-Pitaevskii Equation . . . 25
3.1.2 The Thomas-Fermi Regime . . . 26
3.1.3 Expansion of a BEC: time-of-flight experiments . . . 27
3.1.3.1 The scaling approach . . . 28
3.1.3.2 Ballistic expansion . . . 28
3.1.3.3 Expansion from an isotropic trap . . . 29
3.2 Manipulation of the atoms . . . 29
3.2.1 Magnetic potentials . . . 29
3.2.2 Optical potentials . . . 29
3.2.2.1 The gaussian beam . . . 31
3.3 The preparation of a cloud of ultracold atoms . . . 32
3.3.1 Imaging . . . 33
3.3.1.1 Absorption in the cooling chamber . . . 34
3.3.2 Cooling . . . 34
3.3.3 Transport with an optical tweezer . . . 35
3.4 The second chamber . . . 36
3.4.1 Imaging in the second chamber . . . 38
3.4.2 Evaporation in an optical dipole trap . . . 40
3.4.2.1 The crossed dipole trap . . . 41
3.4.2.2 The evaporation scheme . . . 42
3.4.2.3 Characteristics of the cloud during the evaporation . . . 44
3.4.3 The magnetic levitation . . . 44
3.4.3.1 A model of our levitation . . . 46

3.4.3.2 Experimental implementation . . . 48
3.4.4 Expansion of the BEC . . . 49
3.5 Conclusion . . . 51

4 Characteristics of a three-dimensional speckle disorder 53
4.1 The speckle - a well-controlled, correlated disorder . . . 53
4.1.1 Simple model of the speckle as an diffraction picture . . . 54
4.1.2 Physical model of the speckle . . . 55
4.1.3 Intensity distribution . . . 55
4.1.4 Spatial properties and dimensions of a speckle grain . . . 56
4.1.4.1 Auto-correlation function . . . 56
4.1.4.2 Transverse direction . . . 57
4.1.4.3 Longitudinal direction . . . 57
4.1.4.4 The power spectral density . . . 58
4.2 Realization of a three-dimensional speckle disorder . . . 58
4.2.1 Intensity distribution . . . 59
4.2.2 Correlation function . . . 60
4.2.3 Experimental setup . . . 61
4.3 Conclusion . . . 62

5 Some notions of diffusion and localization of matter waves 65
5.1 From diffusion in a weak disorder... . . . 65
5.1.1 Diffusion as a random walk in a disordered potential . . . 66
5.2 ...to localization in a strong disorder . . . 67
5.2.1 Weak localization . . . 67
5.2.2 The Thouless criterion . . . 68
5.3 Scaling theory . . . 70
5.3.1 Consequences of scaling theory - Localization of all states in one and two dimensions . . . 71
5.3.2 The existence of a mobility edge in 3D . . . 72
5.3.3 The critical region . . . 73
5.4 Microscopic quantaties - Energy scales . . . 73
5.4.1 The scattering time . . . 74
5.4.2 The energy spread and the weak disorder condition . . . 75
5.4.3 The transport length . . . 76
5.4.4 The correlation energy - from classical to quantum disorder . . . 77
5.4.5 The mobility edge in the quantum disorder regime . . . 77
5.4.6 The mobility edge in the classical disorder regime . . . 78
5.4.7 The classical percolation threshold . . . 79
5.4.8 Percolation in an anisotropic 3D speckle . . . 80
5.4.9 The self-consistent theory of localization . . . 81
5.5 Summary - a generic phase diagram in 3D . . . 83

6 Experiments on 3D Localization 85
6.1 Localization in a weak disorder in 1D . . . 85
6.1.1 Key features 1D localization in a speckle disorder . . . 86
6.1.2 Experimental observations . . . 87

6.2 Transposing the 1D scheme to 3D . . . 88
6.2.1 The quantum regime . . . 88
6.2.2 Persistence of the diffusive component at arbitrarily strong disorder 89
6.2.3 Properties of the diffusive component . . . 90
6.2.4 Properties of the localized component . . . 91
6.2.5 Intermediate summary . . . 91
6.3 Expansion of ultra-cold atoms in a strong speckle disorder in 3D . . . 92
6.3.1 The experimental setup . . . 92
6.3.2 Observations . . . 94
6.3.3 Phenomenological model . . . 95
6.3.4 The diffusive component . . . 95
6.3.5 The localized component . . . 97
6.3.6 Trapped fraction . . . 98
6.3.7 Summary of the experimental observations . . . 99
6.4 Comparision to the theoretical model . . . 100
6.4.1 The localized shape and fraction . . . 100
6.4.2 The diffusive component . . . 102
6.4.3 The profiles . . . 103
6.4.4 Conclusions . . . 103
6.5 First studies on the influence of the disorder properties . . . 104
6.5.1 Expansion in an incoherently crossed speckle . . . 104
6.5.2 Modification of the correlations in the disorder . . . 105
6.6 Towards a better control of the energy distribution . . . 106
6.6.1 Experiments on the momentum distribution . . . 106
6.6.2 Ramped scheme . . . 107
6.7 Conclusions . . . 108

7 Experiments on Coherent Backscattering 111
7.1 The coherent backscattering mechanism . . . 111
7.2 The experimental sequence . . . 113
7.2.1 Delta-kick cooling . . . 114
7.2.2 The 2D configuration in an elongated disorder . . . 115
7.3 Investigations of the momentum distribution . . . 116
7.3.1 The scattering time . . . 118
7.3.2 The transport time . . . 119
7.3.3 Analysis of the CBS peak . . . 119
7.4 Dependence on the microscopic properties . . . 121
7.4.1 The scattering time . . . 121
7.4.2 The transport time . . . 123
7.4.3 The CBS signal . . . 124
7.5 Conclusions . . . 125

8 Conclusion 127

A Atom losses during the expansion in the disorder 129

B Publications 131

Bibliography **132**

CHAPTER 1

Introduction

Modern laser cooling [Cohen-Tannoudji 98a, Phillips 98, Chu 98] and evaporative cooling made it possible to observe in 1995 [Ketterle 02, Cornell 02] the accumulation of a macroscopic number of alkaline atoms in a single quantum state, called Bose-Einstein condensation [Einstein 27]. Today, these systems provide a very precise control of the experimental parameters [Bloch 08]:

- The control of the trapping potential makes it possible to let the atoms evolve in different geometries. This is especially interesting in order to study low-dimensional systems. For example it was possible to observe a gas of bosons in the Tonks-Giradeau regime in one dimension (1D) [Kinoshita 04, Paredes 04] and the Berezinskii-Kosterlitz-Thouless (BKT) transition in two dimensions (2D) [Hadzibabic 06].
- Inter-particle interactions are well controlled by Fano-Feshbach resonances, which can be controlled by magnetic fields [Chin 10].
- The atomic density profile can be directly imaged, either by measuring the absorption of a resonant laser traversing the cloud or by measuring the fluorescence emitted by the illuminated atoms.

Therefore, it is now possible to realize ideal systems, which allow us to simulate complex theoretical problems from Condensed Matter Physics. Two emblematic examples perfectly illustrate this possibility: the realization of the Mott transition in the Bose-Hubbard model, which describes the competition between inter-atomic interactions and hopping in the lattice [Greiner 02], and the observation of the BEC-BCS crossover, see [Greiner 03, Bourdel 04] and references therein.

In this context, the group of Pr. Alain Aspect has pioneered another type of quantum simulators: the study of ultracold atoms in controlled disordered potentials [Clément 05, Sanchez-Palencia 07, Billy 08]. Studying such disordered systems is of utmost interest: they lie at the heart of many fundamental phenomena, such as Anderson localization in disordered electronic conductors [Anderson 58], superfluidity in porous media [Reppy 92], and possibly high-Tc superconductivity [Goldman 98]. In spite of extensive studies, the understanding of such systems remains an exciting but formidable task, many issues still being unresolved or even controversial (see e.g.[Weichman 08, Aspect 09, Lagendijk 09, Sanchez-Palencia 10, Burmistrov 12]).

When I arrived in the end of 2008, the team had just proven the potential of their experimental setup with the landmark experiments in which they observed the celebrated Anderson Localization (AL) in one dimension [Billy 08, Roati 08] shown in Fig. 1.1. AL is the most emblematic effect of disorder, describing the appearance of localized states due to interference between many scattering amplitudes associated with the diffusion of a single quantum particle. Motivated by the success of those experiments we aimed to

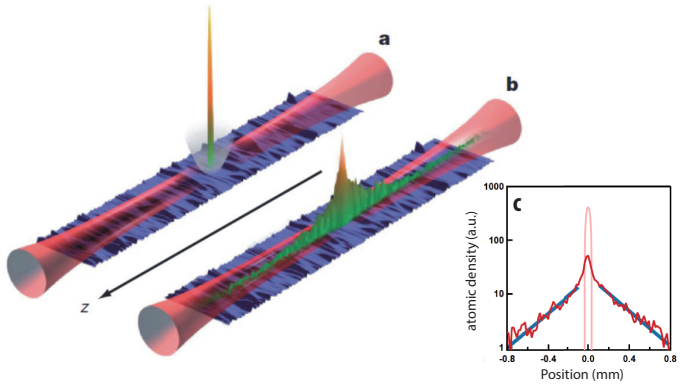

Figure 1.1: **Anderson Localization in 1D** [Billy 08]. a) A very dilute condensate is created in a hybrid trap (The magnetic field is present in grey). b) When the magnetic trap is switched off, the condensate propagates along the optical guide in the presence of a weak disorder and stops after $\sim 1s$. c) Profile in a semilogarithmic scale once the stationary localized regime has been reached. The exponential decay, emblematic for AL, is clearly visible.

first refine our understanding of AL in one dimension (1D) and then to transpose the set-up to the higher dimensional case. In fact, AL depends strongly on the dimension of the system [Abrahams 79]. A quantum phase transition around a mobility edge is predicted in three dimensions (3D). This mobility edge corresponds to an energy threshold separating localized from extended states. Determining the value of that mobility edge and exploring the critical regime around it remains a challenge for microscopic theory, numerical simulations, and experiments [Lagendijk 09]. Nowadays, the originally very abstract concept of AL has even gained some importance for possible applications in optical fibers [Karbasi 12] and possibly even the optimization of the efficiency of solar panels [Vynck 12].

Thesis

This thesis was realized in the Atom Optics group, led by Alain Aspect, in Palaiseau. The results presented in the following were only made possible by the shared effort of all the team members, that I had the pleasure to work with; most importantly Vincent Josse (our team leader), Alain Bernard, Kilian Müller (the PhD students) and Patrick Cheinet (the PostDoc).

At the beginning of my PhD, we substantially improved our setup of a guided atom laser [Bernard 11]. The first goal was to further study 1D AL by making measurements analogous to conductance measurements in condensed matter physics. With the improved apparatus, such studies seemed possible, but we saw a higher possible impact by an investigation of AL in three dimensions (3D) and in the following focused our work on this new subject.

To investigate 3D AL, we transposed the successful scheme that allowed for the observation of one-dimensional Anderson Localization to the three dimensional case. Therefore, we designed a new magnetic levitation and created a very fine-grained disorder by the co-

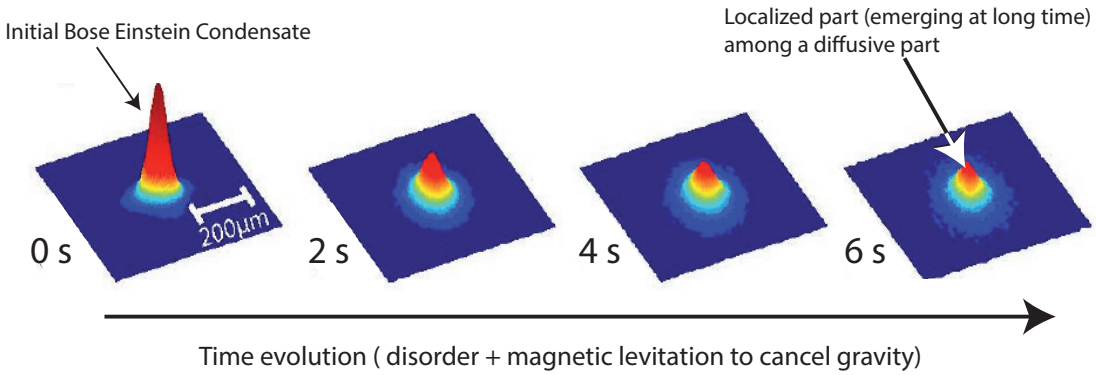

Figure 1.2: **Evidence of 3D localization** (from [Jendrzejewski 12a]). By monitoring (via in-situ fluorescence imaging) the time evolution of the atomic density in a strong disorder, we observe the emergence of a localized fraction among a slowly diffusing part.

herent superposition of two laser speckle fields. At the point where we were finally able to start our experiments on Anderson Localization in 3D, Alain and Patrick sadly had to leave our team on their chase for new challenges. Luckily the newest team member Kilian Müller arrived in this very exciting period. In these experiments, we monitored the three-dimensional expansion of an initial BEC in the presence of a quasi-isotropic laser speckle disorder and observed an atomic cloud composed of two components: a localized and a diffusive part (see Fig. 1.2). The comparison of those experiments to theoretical predictions led to a close and very fruitful collaboration with our theory team of Marie Piraud, Luca Pezzé and Laurent Sanchez-Palencia.

Clear as those experiments on AL in 1D and 3D were, none of these experiments includes a direct evidence of the role of quantum interferences. Interestingly, a first order manifestation of coherence even in a weak disorder is observable. The interference between multiple scattering paths leads to the phenomenon of coherent backscattering (CBS), *i.e.* the enhancement of the scattering probability in the backward direction, due to a quantum interference of amplitudes associated with two opposite multiple scattering paths [Watson 69, Tsang 84, Akkermans 86, Langer 66, Gor'kov 79, Abrahams 79].

In the last part of my PhD we worked on the direct observation of such a CBS peak, which is a direct signal of the role of quantum coherence in quantum transport in disordered media. A cloud of non-interacting ultra-cold atoms was launched with a narrow velocity distribution in an elongated laser speckle disordered potential. Time of flight imaging, after propagation time t in the disorder, directly yield the momentum distribution shown in Fig. 1.3. The most important feature for us is the large visibility peak, which builds up in the backward direction, as it corresponds to the CBS signal.

Outline of the manuscript

- **Chapter 2**: In this introductory chapter, we start the discussion of the coherent propagation of waves, i.e. ultracold atoms, in disordered potentials. In this chapter

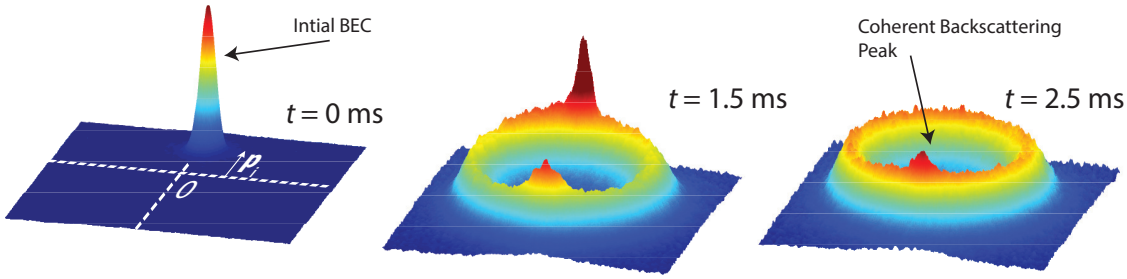

Figure 1.3: **Coherent backscattering** (from [Jendrzejewski 12b]). We monitor the time evolution of the momentum distribution (via time of flight imaging) of a BEC launched initially with a narrow velocity distribution. We observe a ring that corresponds to a redistribution of the momentum directions, due to the scattering on a conservative disordered potential. In the backwards directions a large visibility peak, corresponding to the coherent backscattering signal, builds up.

we intend to show the fundamental importance of interference phenomena on the transport properties of the system, as it can lead to the suppression of transport known as Anderson Localization. We further provide the larger overview of experimental achievements on AL in the different fields of physics, from classical waves over condensed matter to ultracold atoms.

- **Chapter 3**: In this second chapter we present the apparatus, which we constructed in order to perform experiments on Anderson Localization in 3D. We give an overview over the experimental techniques used to produce and to control a cloud of ultracold atoms. We discuss the magnetic levitation and the evaporation in the dipole trap, which were finished in this PhD, in some detail.

- **Chapter 4**: At this point we characterize the properties of the disordered light potential applied to the atoms. It is provided by a speckle potential created by the diffraction of a laser on a rough surface. We show that this disorder is particularly well-controlled and understood as we can completely describe it by its well know correlation length and disorder amplitude. Finally, we discuss how a three-dimensional fine-grained disorder is created by the coherent superposition of two perpendicular speckle fields.

- **Chapter 5**: Having presented the essential ingredients of our experiments, we turn our attention to the most important notions which are necessary for the discussion of our experiments on 3D AL. In the first part we introduce a phenomenological description of the disorder strength. The discussion of the celebrated scaling theory allows us to show that all states are localized in infinite 1D and 2D systems. Further it demonstrates that there is a mobility edge in 3D between the diffusive high energy states and the localized low energy states, which are embedded in the strong disorder. In the second part of this chapter, we discuss the microscopic quantities governing the quantum transport of ultracold atoms.

- **Chapter 6**: At this point we have introduced all the tools needed for the discussion

of our expansion experiments on 3D Localization. In a first step, we point out the key points of those experiments in 1D and how we transposed them into our 3D set-up. We then discuss throughout the rest of the chapter in depth our experiments on 3D Localization.

- **Chapter 7**: We end this manuscript with our findings on Coherent Backscattering of ultracold atoms. After a quick introduction, we explain how we can extract from the evolution of the momentum distribution of the cloud in the disorder important transport quantities, like the scattering time and the transport time. We analyze the time evolution of the Coherent Backscattering signal and end the chapter with first results on the energy dependance of the different transport quantities.

CHAPTER 2

Wave propagation in disorder

Quantum transport differs from classical transport by the crucial role of coherence effects. In the case of disordered media, it can lead to the complete cancelling of transport when the disorder is strong enough: this is the celebrated Anderson localization (AL) [Anderson 58]. We briefly discuss how interferences can lead to weak localization, which is a precursor of AL, and give a short review of some important experiments on the subject. We then discuss some general properties of AL and the state-of-the-art of the experimental findings on this fascinating and rapidly evolving subject.

2.1 Interference and disorder

Whenever a monochromatic wave is diffracted, interference patterns arise. For example, an interference pattern behind a circular aperture exhibits a set of concentric rings, alternating between bright and dark, resulting from constructive or destructive interference (see Fig. 2.1 a). According to Huygens' principle, this interference picture is obtained from the coherent sum over all possible paths through the aperture. The phase associated with each amplitude is proportional to the path length of the scattered wave divided by its wavelength λ.

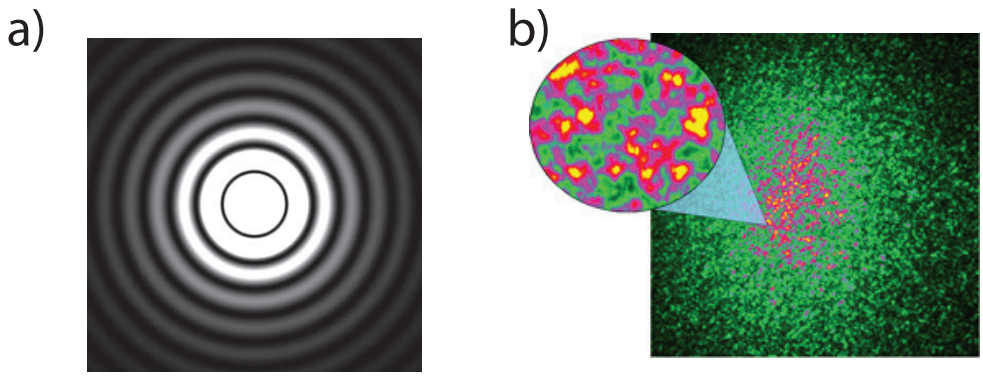

Figure 2.1: **Diffraction patterns**. a) Diffraction pattern of a monochromatic wave on a circular hole. (Image from [Akkermans 07]) b) The diffraction of a monochromatic wave on a thick disorder diffuser yields the presented speckle pattern.

Let us now turn to the diffraction of a coherent source by a thin obstacle whose density

fluctuates in space on a scale comparable to the wavelength of the incoming wave. The resulting interference pattern consists of a random distribution of bright and dark areas, as seen in Figure 2.1 b), called a speckle. As long as the obstacle is thin enough, a wave scatters only once in the random medium on its way to the screen. In a thick medium on the other hand, the wave undergoes multiple scattering. Even after this multiple scattering the phase associated to each path is well determined, coherence preserved and the speckle pattern persists.

This interference pattern might be destroyed in different ways. For an incoherent source, the point sources are out of phases for distances larger than the coherence length L_ϕ. When we illuminate the aperture by an incoherent source of coherence length much smaller than the size of the aperture, the diffraction patterns of the point sources have to be summed incoherently and the interference pattern on the screen disappears. On the other hand, it is possible to employ a coherent light source and rapidly move the obstacle in its plane in a random fashion. In this case, it is the persistence of the detector that averages over many different displaced diffraction patterns and the interference pattern disappeares. These are examples of how interference effects may vanish as the information about the phase gets washed out upon averaging.

2.1.1 Interferences in electron transport in disordered media

The previous idea of wave propagation through a disordered medium also applies to the transport of electrons in metals. In this case, the impurities in the metal are analogous to the scatterers in the optical medium, and the quantity analogous to the intensity is the electrical conductivity. In most cases transport has to be studied for macroscopic samples, with a size bigger than the coherence length L_ϕ, where one expects interference to be washed out. This makes it possible to treat physical phenomena, such as electrical or thermal transport, employing an essentially classical approach, where we neglect the interference between different paths. The enormous success of this classical approach, developed by Drude, led to the belief that coherent effects would be of no importance for the understanding of transport experiments.

In the 1980s a series of experiments allowed to test these coherence properties for the transport of electrons in more detail. Webb et al. observed the influence of a homogenous magnetic field on the conductance of a very fine metal ring [Webb 85]. Changing the strength of the field changes the relative phase between the top and bottom path through the ring(see picture 2.2 a). The shift of this relative phase and the resulting modified interference pattern manifests itself in oscillations of the conductivity . This is the celebrated Aharonov-Bohm effect [Aharonov 59].

One can also perform the experiment with a cylinder that is much longer than the coherence length, instead of a thin wire. The measured signal after this cylinder can then be interpreted as an average over an ensemble of identical, uncorrelated rings from the experiments by Webb. The experiments by Sharvin and Sharvin, performed in this configuration, showed (Fig. 2.2 b) that even after this ensemble average the observed signal was not flat, but oscillating with a period half as long as in the previous experiments. [1]

[1] It is interesting that things went historically the inverse way. In 1981, the observations by Sharvin and Sharvin were no surprise to the experimentalists and "only" confirmed theoretical predictions of the weak localization phenomena. In 1985, Webb et al. even argued that a merit of their experiment was to *not* observe the effect of this weak localization.

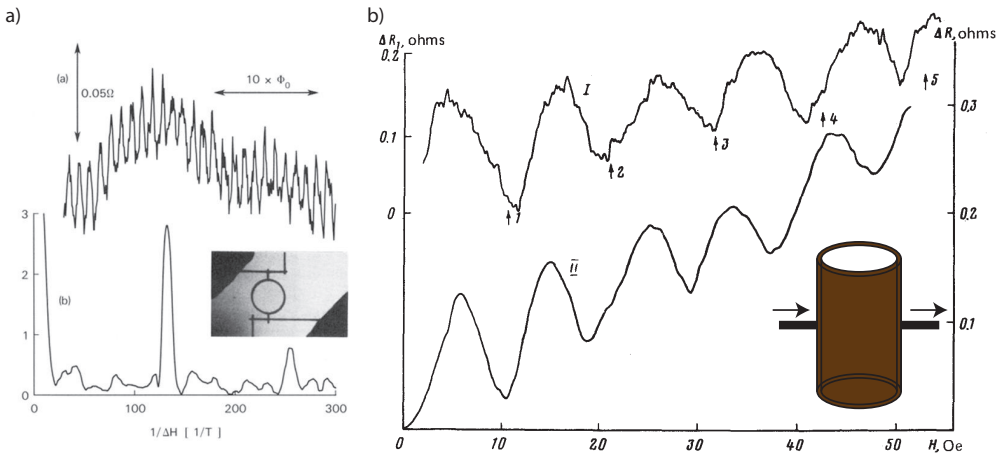

Figure 2.2: **Phase coherence effects in disordered conductors**. a) The experiments by Webb et al. on the conductance oscillations in a thin ring [Webb 85]. The oscillation period as a function of the flux in the ring is h/e. b) The experiments by Sharvin and Sharvin in a very long cylinder. Oscillations in conductance through this macroscopic sample persist, but their frequency has halve to $h/2e$ [Sharvin 81].

Those experiments have shown that quantum interference effects due to disorder can have important manifestations even on a macroscopic scale after ensemble averaging.

2.2 From weak localization...

To understand the nature of these coherence effects, we will consider the propagation of a wave in a disordered medium, modeled by an random ensemble of point scatterers. We

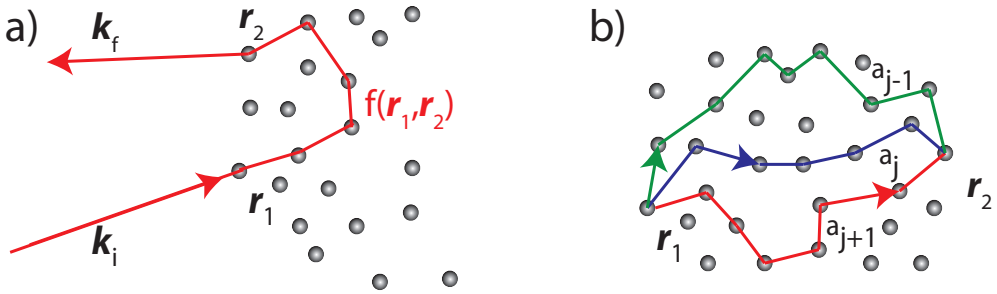

Figure 2.3: **Propagation in the disorder**. a) The initial wave $\mathbf{k}_i$ enters the disorder at the point $\mathbf{r}_1$. It travels to the endpoint $\mathbf{r}_2$ with some amplitude $f(\mathbf{r}_1, \mathbf{r}_2)$ and leaves the disorder with a wave vector $\mathbf{k}_f$. b) Schematic representation of the amplitude $f(\mathbf{r}_1, \mathbf{r}_2)$:The propagation from the initial point to the end point can be done on one of the trajectories a_j. On each of them the wave accumulates a phase δ_j.

are then interested in the amplitude corresponding to the diffraction from the initial plane wave $\mathbf{k}_i$ into another wave $\mathbf{k}_f$ after the propagation in the medium (as shown in Fig. 2.3 a). It may be written in the form

$$A(\mathbf{k}_f, \mathbf{k}_i) = \sum_{\mathbf{r}_{1,2}} f\left(\mathbf{r}_1, \mathbf{r}_2\right) e^{i(\mathbf{k}_i \cdot \mathbf{r}_1 - \mathbf{k}_f \cdot \mathbf{r}_2)} \ , \tag{2.1}$$

where $f(\mathbf{r}_1, \mathbf{r}_2)$ is the amplitude associated with the propagation from $\mathbf{r}_1$ to $\mathbf{r}_2$ (Fig 2.3 b) and without loss of generality $\Delta\phi = (\mathbf{k}_i \cdot \mathbf{r}_1 - \mathbf{k}_f \cdot \mathbf{r}_2)$ is the phase difference between the incoming and outgoing wave. The wave propagates between these endpoints on various trajectories. Each of these trajectories has a certain amplitude $|a_j|$ and an associated phase δ_j. We can then express $f(\mathbf{r}_1, \mathbf{r}_2)$ as a sum of those different paths

$$f(\mathbf{r}_1, \mathbf{r}_2) = \sum_j |a_j| e^{i\delta_j} \tag{2.2}$$

Finally, the probability associated to $A(\mathbf{k}_f, \mathbf{k}_i)$ is given by

$$P(\mathbf{k}_f, \mathbf{k}_i) = |A(\mathbf{k}_f, \mathbf{k}_i)|^2 \tag{2.3}$$

$$= \sum_{\mathbf{r}_{3,4}} \sum_{\mathbf{r}_{1,2}} f\left(\mathbf{r}_1, \mathbf{r}_2\right) f^*\left(\mathbf{r}_3, \mathbf{r}_4\right) e^{i(\mathbf{k}_i \cdot \mathbf{r}_1 - \mathbf{k}_f \cdot \mathbf{r}_2)} e^{i(\mathbf{k}_f \cdot \mathbf{r}_4 - \mathbf{k}_i \cdot \mathbf{r}_3)} \tag{2.4}$$

We now have to apply the ensemble average, noted by $\overline{\ldots}$, over different disorder realizations to Eq. (2.4). We note that most of the terms in the product $\overline{f\left(\mathbf{r}_1, \mathbf{r}_2\right) f^*\left(\mathbf{r}_3, \mathbf{r}_4\right)}$ average to zero due to the random phase accumulated on the different trajectories. The only contributing terms are those for which the relative phases vanish. This can only occur for pairs of trajectories, with exactly the same sequence of scattering events, either in the same or in the opposite direction (Fig. 2.4).

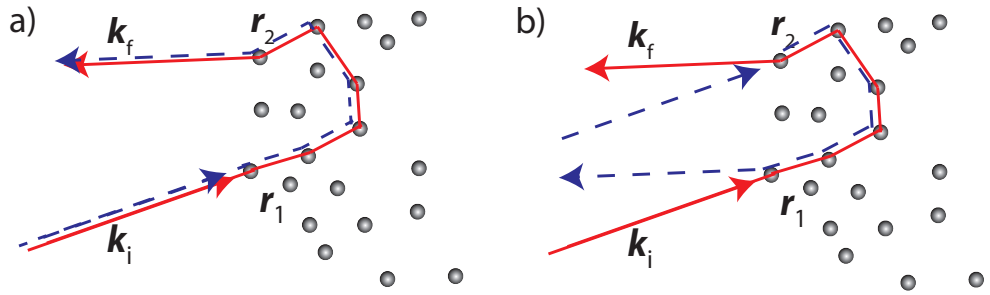

Figure 2.4: **Trajectories with vanishing relative phase**. a) Both trajectories are travelled through in the same direction. This contribution is the classical intensity. b) The trajectories are passed through in opposite directions. This term is at the origin of the weak localization and the coherent backscattering effect.

This leaves only two contributions to the ensemble-averaged probability. For the co-propagating path it implies directly that $\mathbf{r}_1 = \mathbf{r}_3$ and $\mathbf{r}_2 = \mathbf{r}_4$, and for the counter-propagating paths we find $\mathbf{r}_1 = \mathbf{r}_4$ and $\mathbf{r}_2 = \mathbf{r}_3$. Hence, the average probability is given by

$$\overline{P(\mathbf{k}_f, \mathbf{k}_i)} = \overline{\sum_{r_{1,2}} |f(\mathbf{r}_1, \mathbf{r}_2)|^2 (1 + e^{i(\mathbf{k}_f + \mathbf{k}_i) \cdot (\mathbf{r}_1 - \mathbf{r}_2)})} \ , \tag{2.5}$$

where the $\Delta\phi = (\mathbf{k}_f + \mathbf{k}_i) \cdot (\mathbf{r}_1 - \mathbf{r}_2)$ in the second term is the phase difference of the counter-propagating trajectories. This phase factor depends on the scattering positions $\mathbf{r}_{1,2}$ and vanishes in general upon ensemble averaging. There are two very interesting and important exceptions to this.

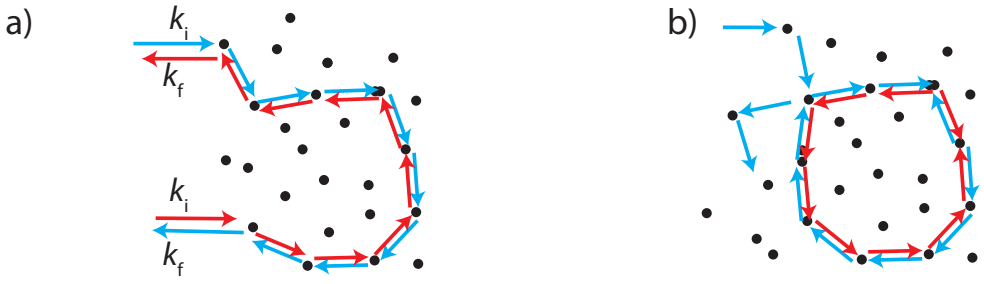

Figure 2.5: **The weak localization and coherent backscattering trajectories**. a) The CBS peak appears in the backwards direction. b) The weak localization correction.

- **Coherent Backscattering (CBS)**: Constructive interferences persist, if

$$\mathbf{k}_f = -\mathbf{k}_i \ . \tag{2.6}$$

  This means that the probability of scattering in the direction opposite to the incident one, is doubled to any other direction (Fig.2.5 a).[2] This phenomena is known as coherent backscattering is discussed in detail in Ch. 7

- **Weak Localization (WL)**: The other very interesting exception are the terms for which

$$\mathbf{r}_1 = \mathbf{r}_2 \ . \tag{2.7}$$

  They correspond to closed multiple scattering trajectories as shown in Fig. 2.5 b). They probability of return to the origin is therefore enhanced by these quantum interferences. This increased return probability will diminish the ability of the wave to travel through the disorder and diminish the conductivity, a phenomena known as weak localization.

2.2.1 Experiments on weak localization and backscattering

The discussed mechanism of weak localization and coherent backscattering was initially proposed by several theoretical groups. Interestingly, those ideas were developed in parallel in the distinct physical fields we have discussed; in optics [Watson 69, de Wolf 71, Barabanenkov 73, Tsang 84, Akkermans 86] and at the same time in the context of condensed matter physics [Langer 66, Gor'kov 79, Abrahams 79]. In condensed matter, the weak localization phenomenon (see e.g. [Altshuler 82, Akkermans 07]) is responsible for the anomalous resistance of thin metallic films [Dolan 79, Bishop 80, Van Den Dries 81]

[2] Actually, the CBS has a finite width as we will explain in Ch. 7.

and its variation with an applied magnetic field [Bergmann 84]. For example, studies on the magnetoresistance of thin Mg films showed convincing proof of weak localization (Fig. 2.6 a). In such experiments the applied magnetic field dephases the counter-propagating paths. This diminishes the effect of WL and leads to the observed decrease of the resistance. It seems very difficult to directly observe CBS of electrons and we are not aware any experiments on this.

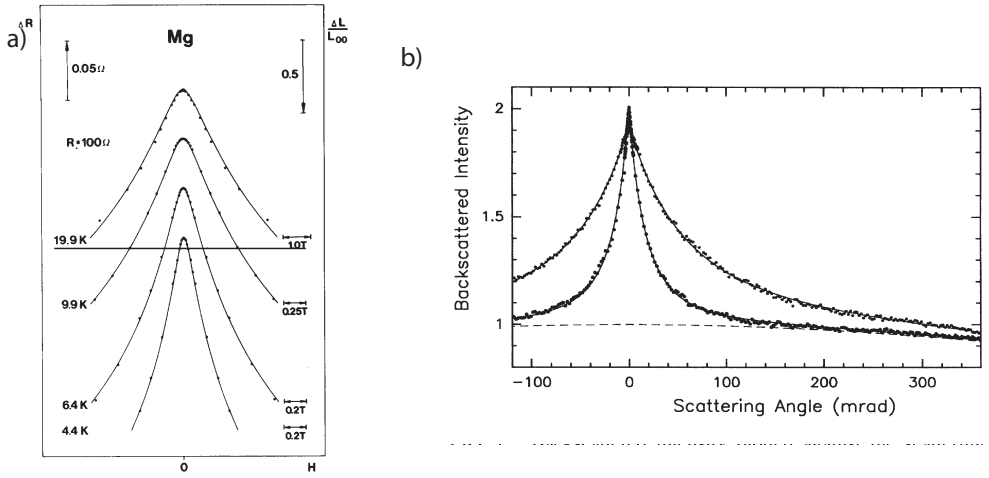

Figure 2.6: **Experiments on WL and CBS**. a) Measurements of the magnetoresistance of Mg films [Bergmann 84]. The magnetic field dephases the loops and diminishes the effect of the WL, which leads to the observed decrease of the resistance. b) The backscattered intensity is observed and yields an enhancement factor of 2[Wiersma 95]. The continuous black line is the theoretical prediction for the shape of the CBS peak [Akkermans 86].

As WL is ubiquitous to wave physics the theoretical predictions triggered considerable experimental efforts to observe further direct signatures of weak localization in classical waves. Shortly thereafter, coherent backscattering was observed in optics [Kuga 84, van Albada 85, Wolf 85]. Still, it took another ten years after the first observation of coherent backscattering until the doubling of the backscattered amplitude was observed by Wiersma et al. in 1995 [Wiersma 95] (see Fig. 2.6 b). In the following, CBS of light has been observed in a numerous situations of multiple scattering: in suspensions of liquid diffusers [Kuga 84, Wolf 85], on cold atoms [Labeyrie 99], with speckle fields [van Tiggelen 90], and even with incoherent light like the light from the sun [Okamoto 96, Lenke 97]. Nowadays, the study of CBS was extended to other systems of classical waves like acoustics [Bayer 93, Tourin 97] and seismology [Larose 04].

2.3 ... to the suppression of transport - Anderson Localization

The presented theoretical and experimental studies are the first order manifestation of interference effects on quantum (or wave) transport through disorder media. They clearly showed that quantum transport differs from classical transport by the crucial role of

coherence effects. They can even lead to the complete suppression of transport when the disorder is strong enough: the famous Anderson localization [Anderson 58]. In this localized regime, the propagation is inhibited and the wave (or quantum particle) remains localized around its initial position. Anderson showed further that the localized wave function has a spatial exponential decay from the point of localization with a localization length ξ.

As so often in physics, the historical development of localization did not follow the logics of how localization is often presented nowadays. Initially predicted by P.W. Anderson for spins or electrons in "certain random lattices" in 1958, the importance of AL was underestimated for a long time. This was probably due to the complexity of the paper and the absence of a clear physical mechanism giving rise to localization.[3]

For some years, it was Mott[4] and coworkers, who sustained the study of Anderson Localization. They gave a qualitative criterion of when the localization should arise. As the influence of the disordered medium is increased, the approach outlined in the previous section breaks down when the wavelength λ_{dB} of the incident wave becomes of the same order of magnitude as the mean free path l, the typical distance between successive scattering events. Then the particle is continuously scattered by the disorder and can not propagate anymore. Effectively, a transition from the diffusive regime to the strongly or Anderson localized regime, where the transport stops, takes places. The position of this transition, called *mobility edge*, is given by the Ioffe-Regel criterion $kl \approx 1$ [Ioffe 60].

Only in the 70s and 80s, twenty years after Anderson's pioneering paper, the interest in localization increased considerably and our current picture of localization emerged. At this point, people understood that localization should highly depend on the dimensionality of the system. Initial pioneering works by Langer [Langer 66], Wegner [Wegner 76], Thouless [Thouless 77], and Gorkov [Gor'kov 79] layed then the ground for the scaling theory by Abrahams, Anderson, Licciardello and Ramakrishnan [Abrahams 79]; the so-called "gang of four". From the scaling theory the importance of interferences for localization became clearer [Lee 85] and the previously presented experimental investigations on weak localization started. Further, it was shown in this context that all states are localized in a one dimensional systems even in the presence of very weak disorder [Landauer 70]. This is also the case in 2D, although here the localization length increases exponentially when the influence of disorder decreases.[5] In 3D, the behavior is quite different: there is a real phase transition between a diffusive regime and a localization regime. Here the critical exponents (s and ν) characterizing the transition can be defined in part by the evolution of the characteristic parameters of the system around the transition, namely the diffusion constant and the localization length:

$$D \propto |E - E_C|^s \text{ for } E \geq E_C \tag{2.8}$$

$$\xi \propto |E_C - E|^{-\nu} \text{ for } E \leq E_C \ , \tag{2.9}$$

where E is the wave energy and E_C the critical energy corresponding to the transition. In the community there is now general agreement, based on numerical simulations,

[3] An excellent review on AL in general and its historical evolution can be found in the book "50 years of Anderson Localization" edited by E. Abrahams [Anderson 10].

[4] The father of the celebrated Mott transition.

[5] The possible existence of a mobility edge in 2D, strongly supported by Mott, had been subject of a long going debate before.

[Kramer 93] that both exponents are $s = \nu = 1.58$. But even 50 years after the pioneering work of Anderson, there is still no analytical prediction for the position of the mobility edge and an experimental determination of the critical exponents remains a major challenge.

2.3.1 Experiments on Anderson Localization

Anderson localization has of course been the subject of numerous experimental studies [Lee 85, Kramer 93]. Originally predicted in the context of condensed matter, the first studies have been conducted in electronic systems. The study of the consequences of weak localization were therefore extended to the ones of strong localization regime. Measurements of the conductivity and dielectric susceptibility of 2D disordered semiconductors, silicon doped [Rosenbaum 83] and $Al_xGa_{1-x}As$ [Katsumoto 87], allowed the first observations of the metal-insulator transition in the 80's. However, interactions between electrons and the presence of thermal excitations made quantitative measurements in such electronic systems very delicate and better controlled systems were needed. One actually had to wait until 1997 to have experimental evidence for Localization in 1D electronic conductors [Gershenson 97].

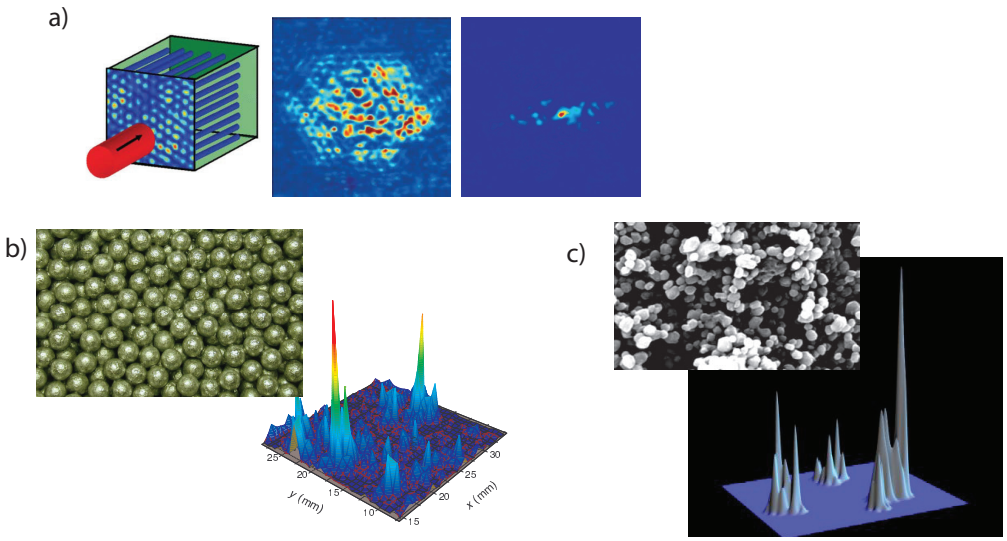

Figure 2.7: **Anderson localization of classical waves**. Anderson Localization of classical waves has been observed, for example, with a) photonic crystals [Schwartz 07] b) ultrasound [Hu 08] and c) light [Wiersma 97].

Since the 90s, Anderson Localization is therefore also studied outside of the field of condensed matter in other systems, which are easier to monitor (see Fig. 2.7). Being linked to the presence of interferences, AL is observable in all wave systems: as well classical as quantum. In particular, the previously mentioned observations of CBS in the 1980s and a proposal of S. John [John 88] in 1988 have stimulated intense research around Anderson Localization of acoustic or electromagnetic waves, such as μ-waves [Hauser 92] and light waves [Wiersma 97] (see Fig. 2.7). Although these systems are *a priori* more easily controlled, especially because of the absence of interactions, the obtained results

were controversial. In such experiments it is difficult to differentiate between the signatures of localization of those of absorption: both lead to an exponential decrease of the wave function as a function of the thickness of the scattering medium. However, this problem was overcome by measuring the fluctuations of the transmission [Chabanov 00] or by studying its dynamics [Chabanov 03, Störzer 06, Lagendijk 09]. Finally, recent experiments in disordered photonic crystals [Schwartz 07, Lahini 08], μ-waves [Laurent 07] and ultrasound [Hu 08] have directly observed the localized wave functions.

2.4 Experiments with ultracold atoms

Only relatively recently cold atoms have been proposed to study the problem of localization [Damski 03]. Ultracold atoms have proven to be a formidable system for the study of condensed matter physics [Bloch 08]. They allow to implement systems in any dimension; the control of the interatomic interactions, either by density control or by Feshbach resonances, the possibility to design well-controlled and phonon-free disordered potentials, the application of synthetic magnetic fields [Lin 09], and the opportunity to measure in situ atomic density profiles via direct imaging.

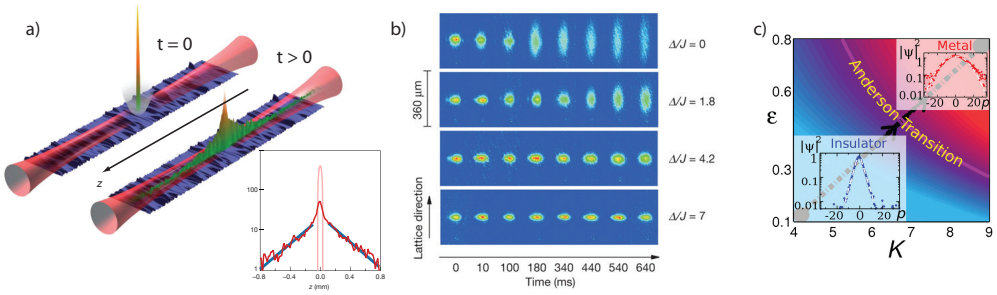

Figure 2.8: **1D systems showing Anderson localization of ultracold atoms**. First observation on 1D localization of ultracold atoms by a) the Aspect group [Billy 08] b) the Inguscio group [Roati 08]. c) The Anderson transition was investigated using the kicked rotor systems in the Garreau group [Chabé 08].

The first experiments, conducted in 2005 [Schulte 05, Fort 05, Clément 05], with a disorder created by a optical speckle pattern, however, were inconclusive, partly because of too strong interatomic interactions. Theoretical work that followed [Sanchez-Palencia 07, Fallani 08, Sanchez-Palencia 08] provided a better understanding of the regime which was necessary to reach. In 2008, Anderson localization was finally observed in one dimension (Fig. 2.8) by our team [Billy 08]. In parallel, the Inguscio group in Florence had meanwhile highlighted the phenomenon in a one-dimensional bichromatic lattice, reproducing the Aubry-André model, which exhibits a transition to a localized regime [Roati 08].

Cold atoms have also been used to demonstrate Anderson Localization in momentum space for kicked rotor systems. The Hamiltonian of these systems can be mapped on the Hamiltonian describing the Anderson localization, by replacing the direct space coordinates by coordinates in momentum space [Casati 89]. With these systems it is also possible to explore with Anderson Localization in different dimensions by adding kicks at

incommensurable frequencies. The experiments were performed in 1D [Moore 94], and 3D in the team of Jean-Claude Garreau in Lille [Chabé 08, Lemarié 10, Lopez 12].

2.5 Conclusion - Towards higher dimensions and interacting bosons

The success of the experiments in 2008 proved the utility of ultracold atoms to investigate disordered systems. It was then the logical next step to use these systems for the investigation of more complex systems. These efforts focus nowadays on two important properties: the influence of dimensionality and interactions.

With interactions the simple wave picture breaks down rapidly and the problem gets extremely difficult to treat. A particular interest has been put on the "dirty bosons" problem, which is still a major challenge for theory and experiment, see i.e. [Lugan 07, Paul 07, Falco 09a] and references therein. Especially the conditions for the appearance of an insulating phase called *Bose glass* [Giamarchi 88, Fisher 89] remain controversial [Roux 08, Roscilde 08, Pollet 09, Gurarie 09]. Recently the first experimental results for disordered, weakly interacting bosons in 1D were published by the groups of Inguscio [Deissler 10], and of Randall Hulet in Houston [Dries 10]. First experiments on the influence of disorder on the BKT transition in 2D were presented by the Krub experiment in our group [Allard 12] and the Rolston group in Washington [Beeler 12]. The observed shift of the critical temperature awaits now to be confronted to different theories [Lopatin 02, Pilati 08, Pilati 10]. Meanwhile, the group of Brian DeMarco at Urbana has developed an experimental system to achieve the disordered Bose-Hubbard model, and thus to probe the regime of strong interactions [White 09, Pasienski 10].

In the non-interacting case, it is extremely interesting to investigate higher dimensions and target the investigation of the critical region around the mobility edge. First results on diffusion in 2D where obtained by our the 2D experiment of our group [Robert-de Saint-Vincent 10]. With the kicked rotor system refined measurements of the critical exponents were performed. The measured value of $\nu = 1.63 \pm 0.05$ is very close to the expected value [Kramer 93]. To our knowledge, this is the only experimental observation of the critical exponents in agreement with numerical predictions up to today. The precise determination of these critical exponents in a disorder is therefore still an issue for which cold atoms could be used [Sanchez-Palencia 10], and is one of the objectives of the experiment described in this manuscript. In 2012, two groups published on the observation of 3DLocalization of ultracold atoms. We demonstrated evidence for localization of bosons in a speckle disorder [Jendrzejewski 12a], while the deMarco group reported on studies on the expansion of a Fermi gas in a very anisotropic disorder [Kondov 11].

The main part of this manuscript is then devoted to our efforts leading towards a precise investigations of the critical region. We discuss general important notions on Localization in more detail in Ch. 5 and our experimental findings on Anderson Localization of ultracold atoms in three dimensions in Ch. 6. Convincing as existing experiments on AL with ultracold atoms are, they do no provide a direct proof of coherence. We will present in the last chapter of this manuscript our results on CBS of ultracold atoms [Jendrzejewski 12b], see Ch. 7, obtained simultaneously with the Labeyrie group in Nice [Labeyrie 12]. Those experiments provide a first direct observation of phase coherent transport with ultracold atoms.

CHAPTER 3

Production of coherent matter waves

Bose-Einstein condensates (BEC) of dilute atomic clouds provide unique opportunities for exploring quantum phenomena on a macroscopic scale. They have first been realized in 1995 in the Boulder group with rubidium atoms [Anderson 95] and only months later in the Ketterle group at the MIT with sodium atoms [Davis 95a]. In these experiments a dilute cloud is cooled to temperatures in the nano-kelvin regime. At a critical temperature the wave packets of the different bosonic atoms overlap and a Bose-Einstein condensate develops. In such a condensate the lowest energy state gets collectively occupied by a macroscopic number of atoms. With our experimental apparatus we prepare condensate with several 10^4 atoms at some nK as a starting points for our subsequent experiments with ultracold atoms in a disordered speckle potential.

We begin this chapter with a short introduction to the theoretical description of Bose-Einstein condensates. We then describe the experimental set-up for the production of the Bose-Einstein condensate.

3.1 Generalities about Bose-Einstein condensates

In this section we will discuss some important theoretical results about Bose-Einstein condensates that we will use in the following to describe our experiments. We will only present some major results here and leave out their derivation. For more details we refer the reader to the detailled reviews on Bose-Einstein condensates [Dalfovo 99, Ketterle 99, Castin 01, Leggett 01].

3.1.1 Bose-Einstein condensation and the Gross-Pitaevskii Equation

Bose-Einstein condensation [Dalfovo 99] corresponds the the accumulation of a macroscopic number of bosons, integer-spin particles, in the lowest energy state of the quantum system. Qualitatively, it occurs when the wave packets describing the individual bosons start to overlap. In other words, the atoms condense in the fundamental state once the de Broglie wavelength λ_{dB} is at the order of magnitude or bigger than the inter-particle distance $d \sim n^{-1/3}$.

$$D = n\lambda_{dB}^3 \sim 1 \text{ with } \lambda_{dB} = \sqrt{\frac{2\pi\hbar^2}{mk_BT}} \ , \tag{3.1}$$

where D is the phase-space density, m the mass of the atoms, T their temperature and n is the density of the cloud. In the experiment we work with a three-dimensional harmonic trap with curvatures $\omega_{x,y,z}$. The phase-space-density in such a harmonic trap is given by

[Dalfovo 99]

$$D = \left(\frac{\hbar\overline{\omega}}{k_B}\right)^3 \frac{N}{T^3} \ , \tag{3.2}$$

where $\bar{\omega} = (\omega_z\omega_y\omega_z)^{1/3}$ and N is the total number of atoms. Then, the condition for condensation Eq. (3.1) can be translated into a critical temperature

$$T_c = 0.94\frac{\hbar\bar{\omega}}{k_B}N^{1/3} \ . \tag{3.3}$$

Below the transition temperature the atoms accumulate in the ground state of the trap and clouds with high atomic densities are obtained. Because of these high densities, interactions via two-body collisions are very frequent and have to be taken into account for the description of the ground state. These collisions are well characterized by the scattering length a, which describes the effective size of the atoms for s-wave scattering [Chikkatur 00][1]. In our experiments we use the repulsively interacting ^{87}Rb with a scattering length of $a = 5.3$nm.

Because we work with very dilute gases ($na^3 \ll 1$) , we can use a mean-field description for the interactions $V_{int}(\mathbf{r}) = g \cdot n(\mathbf{r})$ with the coupling constant $g = \frac{4\pi\hbar^2}{m}a$. The evolution of the wave function $\psi(\mathbf{r}, t)$ of such a weakly-interacting condensate with N atoms in an external potential $V(\mathbf{r})$ is driven by the time-dependent Gross-Pitaevskii Equation

$$i\hbar\frac{\partial}{\partial t}\psi(\mathbf{r}, t) = \left[-\frac{\hbar^2}{2m}\Delta + V(\mathbf{r}) + g|\psi(\mathbf{r}, t)|^2\right]\psi(\mathbf{r}, t) \ . \tag{3.4}$$

In the stationary regime, we can write the wave function as $\psi(\mathbf{r}, t) = \phi_0(\mathbf{r})e^{-i\mu/\hbar t}$. $|\phi_0(\mathbf{r})|^2 = n(\mathbf{r})$ is the spatial density and μ the chemical potential of the condensate, which describes the increase of the total energy by adding an atom to the condensate with N atoms. The leads to the stationary Gross-Pitaevskii equation

$$\left[-\frac{\hbar^2}{2m}\Delta + V(\mathbf{r}) + g|\phi_0(\mathbf{r})|^2\right]\phi_0(\mathbf{r}) = \mu\phi_0 \ . \tag{3.5}$$

The first term on the left-hand side of the equation describes the kinetic energy of the condensate, the second one its potential energy and the third one the interaction energy.

3.1.2 The Thomas-Fermi Regime

We can estimate the kinetic and interaction energy of a condensate in a harmonic trap using the size of the harmonic oscillator $\sigma = \sqrt{\hbar/m\omega}$

$$E_{kin} \sim N\frac{\hbar^2}{2m\sigma^2} \tag{3.6}$$

$$E_{int} = N^2\frac{g}{2}\frac{3}{4\pi\sigma^3} \ . \tag{3.7}$$

[1] Scattering in higher order orbitals like d and g -wave are negligible in our experiments due to the very low energies we are working at [Thomas 04, Buggle 04]

When the number of atoms is large $N \gg \sigma/a$, we can neglect the kinetic energy in comparison to the interaction energy. In this *Thomas-Fermi regime*, the spatial density takes the simple form

$$n(\mathbf{r}) = \max\left(\frac{\mu - V(\mathbf{r})}{g}, 0\right) \tag{3.8}$$

$$n_{trap}(x,y,z) = \max\left(\mu/g - \sum_{i=x,y,z} \frac{m\omega_i^2}{2g} r_i^2, 0\right) , \tag{3.9}$$

where the second quantity describes the profile in a harmonic trap. It is an inverted parabola with radius

$$r_{TF,i} = \sqrt{\frac{2\mu}{m\omega_i^2}} , \tag{3.10}$$

where $i = x, y, z$ indicates the direction. Via the normalization of $n(\mathbf{r})$ we determine the chemical potential

$$\mu = \frac{1}{2}\left(15aN\hbar^2\bar{\omega}^3\right)^{2/5} m^{1/5} . \tag{3.11}$$

We can rewrite the condition for the validity of the Thomas-Fermi approximation as $\mu \gg \hbar\omega_i$. In our experiment we have typical chemical potentials of $\mu/h \sim 50$Hz with trapping frequencies of $\omega_i/2\pi \sim 5$Hz. Hence, our trapped condensates are in the Thomas-Fermi regime, where we can neglect the kinetic energy and their interaction energy is given by [Dalfovo 99]

$$E_{int} = \frac{g}{2}\int d\mathbf{r}\; n(\mathbf{r})^2 \tag{3.12}$$

$$\Rightarrow E_{int,TF} = \frac{2}{7}\mu . \tag{3.13}$$

The most common way to characterize those Bose-Einstein-condensates are the time-of-flight experiments we are going to present in the following.

3.1.3 Expansion of a BEC: time-of-flight experiments

The experiments presented in this manuscript use the BEC as a source of matter waves to study their transport properties. The easiest way to let these matter waves propagate, is to cut the trap suddenly and let the atoms expand freely. During this expansion the interaction energy E_{int} is transformed into kinetic energy E_{kin}. We will use this technique in order to create a cloud of non-interacting atoms with a certain velocity distribution as described in the following.

At the beginning of the expansion the kinetic energy is negligible and the only contribution to the total energy, called the release energy, is the interaction energy

$$E_{rel} = E_{int,TF} = \frac{2}{7}\mu . \tag{3.14}$$

After a time of several $1/\omega_i$, the interaction energy is transformed into kinetic energy. We thus have created a non-interacting wave packet with a typical energy spread on the order of μ. Given the simplicity of these so called *time-of-flight* (TOF) experiments, they are a commonly used tool to characterize the properties of the condensate.

The dynamics of the condensate can be studied in the framework of the time-dependent Gross-Pitaevskii equation 3.4. In the approximation of the Thomas-Fermi regime it can be shown that the condensate is following some scaling laws that we are going to discuss now.

3.1.3.1 The scaling approach

It was shown that the expansion of a BEC is described by a rescaling of the initial parabolic shape of the cloud [Kagan 96, Castin 96]. Hence, the atomic density in the direction i evolves over time with

$$n(r_i,t) = \frac{1}{b_x(t)b_y(t)b_z(t)} \cdot n(r_i/b_i(t),0) \tag{3.15}$$

$$\text{with } \frac{d^2b_i(t)}{dt^2} = \frac{\omega_i^2}{b_ib_xb_yb_z} - \omega_{res,i}^2 b_i(t) \ , \tag{3.16}$$

where $\omega_{res,i=x,y,z}(t)$ are residual frequencies after the switch-off [2]. The $b_i(t)$ are the rescaling functions with initial conditions $b_i(0)=1$ and $\dot{b}_i(0)=0$.

For very long expansion times, where the size of the expanding cloud is much bigger than the initial size, the observed profile $n(r,t)$ gives the velocity distribution of the atoms by $n(v_i = r_i/t)$ [3]. Thus, we can calculate the velocity distribution from Eq. 3.16

$$n(v_x,v_y,v_z,t) = \max\left(\frac{15N}{8\pi\bar{v}^3}\left(1-\sum_i \frac{v_i^2}{v_{i,max}^2(t)}\right),0\right) \ , \tag{3.17}$$

where $\bar{v} = (v_{x,max}(t)v_{y,max}(t)v_{z,max}(t))^{1/3}$ is the average speed and $v_{i,max}(t) = \dot{b}_i(t)\cdot r_{TF,i}$ is the maximum velocity.

In general, the maximum velocity has to be determined from the equations (3.16). The analytical solution of these equations are only known in several limiting cases.

3.1.3.2 Ballistic expansion

A common situation is the free expansion, where the residual frequencies are negligible $\omega_{i,res}=0$.[4]

From Eq. (3.16) we see that the typical time scale of the evolution is $1/\omega_i$. After this time the released energy is given by the total kinetic energy.

$$E_{rel}(t\to\infty) = E_{kin,tot}(t\to\infty) \tag{3.18}$$

$$= \int d\mathbf{v}\ n(\mathbf{v},t\to\infty)\cdot\frac{m}{2}\mathbf{v}^2 \tag{3.19}$$

Using Eq. (3.17) and (3.14), this leads to the relation

$$E_{kin,max} = \frac{m}{2}\sum_i v_{i,max}^2(t\to\infty) = 2\mu \tag{3.20}$$

[2] In our case coming from the magnetic levitation, see Sec. 3.4.3

[3] This is not the velocity distribution in the trap. The interaction energy has now been converted into kinetic energy

[4] An analytical solution was derived for the case of the release from a very elongated trap in [Castin 96]
.

3.1.3.3 Expansion from an isotropic trap

In our experiment we create a BEC in a quasi-isotropic trap with trapping frequency $\omega_i \simeq \omega_{trap}$ and negligible residual trapping after the switch-off $\omega_{res,i} \simeq 0$. In this case, we can deduce v_{max} directly from Eq. (3.20)

$$\frac{m v_{max}^2(t \to \infty)}{2} = \frac{2\mu}{3} \tag{3.21}$$

$$v_{max}^2 = \frac{4\mu}{3m} \tag{3.22}$$

This relation allows us in the experiments to measure precisely the chemical potential in the trap from TOF-experiments as we will discuss in Sec. 3.4.4.

3.2 Manipulation of the atoms

In the previous section we introduced the most important notions on Bose-Einstein condensates. In this section, we want to describe how we can manipulate neutral atoms with magnetic and optical interactions in order to achieve such Bose-Einstein condensates.

3.2.1 Magnetic potentials

The magnetic momentum $\boldsymbol{\mu}$ of the atoms is coupled to a static magnetic field $\mathbf{B}(\mathbf{r})$ by the potential $V_{mag}(\mathbf{r}) = -\boldsymbol{\mu} \cdot \mathbf{B}(\mathbf{r})$. The energy shift induced by this coupling is described by the Breit-Rabi formula for ^{87}Rb in the $5^2S_{1/2}$ ground-state [Breit 31]:

$$E_{mag,\pm} = \pm \frac{h\Delta\nu}{2} \sqrt{1 + m_F \xi + \xi^2} \text{ with } \xi = 2\frac{\mu_B |\mathbf{B}(\mathbf{r})|}{h\Delta\nu} \ , \tag{3.23}$$

where $\Delta\nu = 6.835$GHz is the splitting between the hyperfine levels $F = 1$ and $F = 2$. m_F is the quantum number which corresponds to the projection off the magnetic moment on the local direction of $\mathbf{B}(\mathbf{r})$. In this Breit-Rabi formula the potential energy depends only on the norm of the magnetic field and not its direction, because the spin of the atoms follows the magnetic field lines adiabatically with the Larmor frequency.

We have pictured the potential energy as a function of the strength of the magnetic field in Fig. 3.1. For weak magnetic fields the induced Zeeman shift is proportional to the norm of the magnetic field $|\mathbf{B}(\mathbf{r})|$:

$$V_{mag,Z}(\mathbf{r}) = g_F \mu_B m_F |\mathbf{B}(\mathbf{r})| \tag{3.24}$$

where g_F is called the Lande factor ($g_{F=1} = -1/2$ and $g_{F=2} = 1/2$). If the field is strong the interaction term dominates the hyperfine energies. In this case, the slope is proportional to the quantum number associated to the fine structure m_J.

3.2.2 Optical potentials

If the atom is interacting with a laser it will experience forces of two different kinds [Cohen-Tannoudji 98b]. We can mostly understand them in terms of a two-level atom with a transition frequency $\omega_0/2\pi$ and lifetime Γ^{-1} of the excited state. We note the

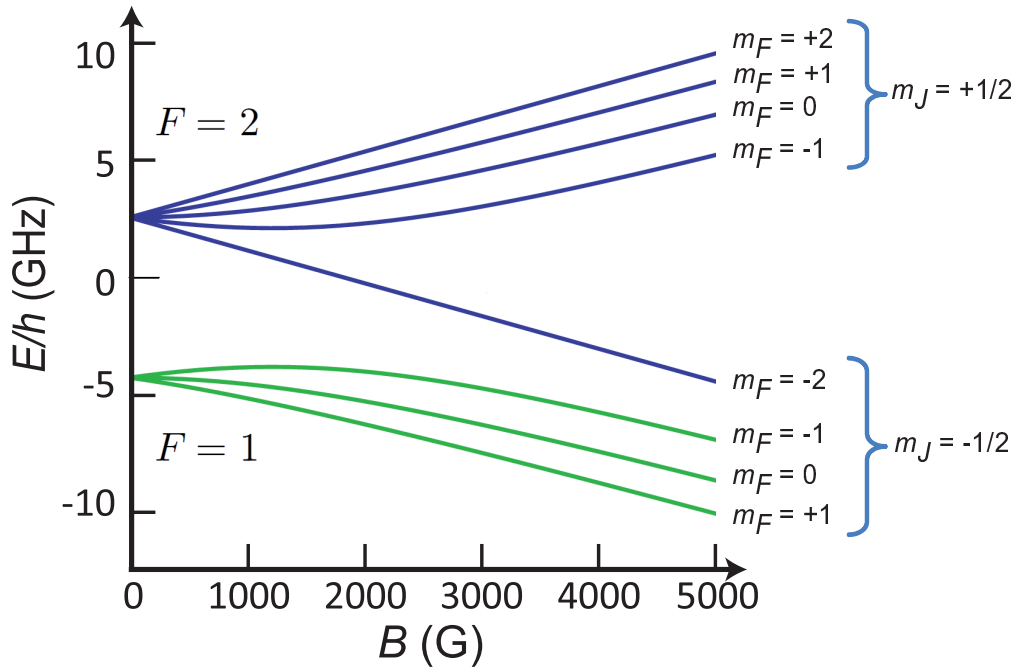

Figure 3.1: **The Breit-Rabi diagram for the Rubidium 87 $5^2S_{1/2}$ ground state** [Steck 06]. For very low magnetic fields $B < 100$ G the Zeeman effect describes well the energy displacement. For higher magnetic fields we need to use the exact formula Eq. (3.23).

wavelength of the laser λ_L, its frequency $\omega_L/2\pi$ and its intensity $I(\mathbf{r})$. The generalized detuning of this laser to the atomic transition is then

$$\tilde{\delta} = \left(\frac{1}{\omega_0 - \omega_L} + \frac{1}{\omega_0 + \omega_L}\right)^{-1} \tag{3.25}$$

Depending on the detuning, the atom experiences different forces:

- **Radiation pressure**: We consider a laser propagating in z-direction at resonance, i.e. $\Gamma \gg \tilde{\delta}$. The atom changes its momentum by $\hbar k_L \mathbf{u}_z$ at each absorption of a photon. Once excited, it emits this photon at a rate Γ_{sc} which is the lifetime of the excited state multiplied by the probability that the atom is in an excited state $\frac{1}{2}\frac{s(\mathbf{r})}{1+s(\mathbf{r})}$, where $s(\mathbf{r})$ is the saturation parameter

$$s(\mathbf{r}) = \frac{I(\mathbf{r})/I_{Sat}}{1 + 4\tilde{\delta}^2/\Gamma^2} \tag{3.26}$$

  and I_{Sat} is the saturation intensity ($I_{Sat} = 1.67 mW/cm^2$ for ^{87}Rb) . As the photon is emitted in a random direction, the repeated cycle will result in a dissipative force of the form

$$\mathbf{F}_{rad}(\mathbf{r}) = \frac{\hbar k_L \Gamma}{2} \frac{s(\mathbf{r})}{1 + s(\mathbf{r})} \mathbf{u}_z \tag{3.27}$$

  This dissipative force is used for laser cooling described in Sec. 3.3.2.

- **Dipole force**: Atoms interacting with an off-resonance laser ($\Gamma \ll \tilde{\delta}$) experience primarily a light shift and spontaneous emission becomes negligeable [Dalibard 85]. This light shift leads to the *dipole potential*, which reads for a two-level atom [Grimm 00]

$$V_{Dip}(\mathbf{r}) = -\frac{3\pi c^2}{2\omega_0^2}\frac{\Gamma}{\tilde{\delta}} I(\mathbf{r}) \tag{3.28}$$

  This force is particularly useful to design conservative potentials, as it is simply proportional to the laser intensity $I(\mathbf{r})$. By convenience, the potential can be chosen to be attractive with a red-detuned laser ($\omega_L < \omega_0$) or repulsive with a blue-detuned laser ($\omega_L > \omega_0$).

It is sometimes useful to express the spontaneous emission rate in terms of the dipole potential by

$$\Gamma_{sc}(\mathbf{r}) = \frac{\Gamma}{\tilde{\delta}}\left(\frac{\omega_L}{\omega_0}\right)^3 \frac{V_{Dip}(\mathbf{r})}{\hbar} \tag{3.29}$$

This relation makes it immediately clear that the influence of spontaneous emission compared to the strength of the the dipole potential becomes negligible at large detuning.

Further, it is in theory necessary for ^{87}Rb atoms to take into account the multi-level structure of the atoms. In practice, the corrections are almost always negligible for the detuning we use. The highest deviation to Eq. (3.28), due to the fine structure, is in the order of 2% for $\lambda_L = 1070$nm .

3.2.2.1 The gaussian beam

The simplest way to create a trap using the dipole potential (3.28) is a far red-detuned ($\Delta > 0$) focused Gaussian beam [Grimm 00]. The intensity distribution of the focused Gaussian beam with power P propagating in z-direction is:

$$I(r,z) = \frac{2P}{\pi w(z)^2}\exp\left(-2\frac{r^2}{w(z)^2}\right) \text{ with } w(z) = w_0\sqrt{1+(z/z_R)^2}\,, \tag{3.30}$$

where r denotes the radial coordinate, w_0 the waist of the beam and $z_R = \pi w_0^2/\lambda$ its Rayleigh length.

The depth of the potential can be calculated from Eq. (3.28) with the maximal intensity of the beam

$$U_0 = -\frac{3\pi c^2}{2\omega_0^2}\frac{\Gamma}{\tilde{\delta}}\frac{2P}{\pi w_0^2} \tag{3.31}$$

A development of the intensity distribution shows us that the laser beam creates a harmonic potential around its focal point. The trapping frequencies are

$$\omega_r = \sqrt{\frac{4U_0}{mw_0^2}} \text{ and } \omega_z = \sqrt{\frac{2U_0}{mz_R^2}} \tag{3.32}$$

It is worth mentioning that the Rayleigh length z_R is typically much bigger than the waist w_0, which means that a trap created by such a simple Gaussian beam is in most cases very elongated in the z-direction.

Such a gaussian beam is used in our experiment as optical tweezer in order to transport the atoms (see Sec. 3.3.3). The dimple beam of our crossed dipole trap is a second example of a gaussian beam used on our experiment (see Sec.3.4.2.1).

3.3 The preparation of a cloud of ultracold atoms

We now continue with a detailed presentation of the experimental setup that allowed us to create freely expanding matter-waves with ultra-cold atoms. The apparatus, sketched in Fig. 3.2, was discussed in great detail in the thesis of A. Bernard [Bernard 10]. So we present only the major steps of the experimental cycle in this manuscript.

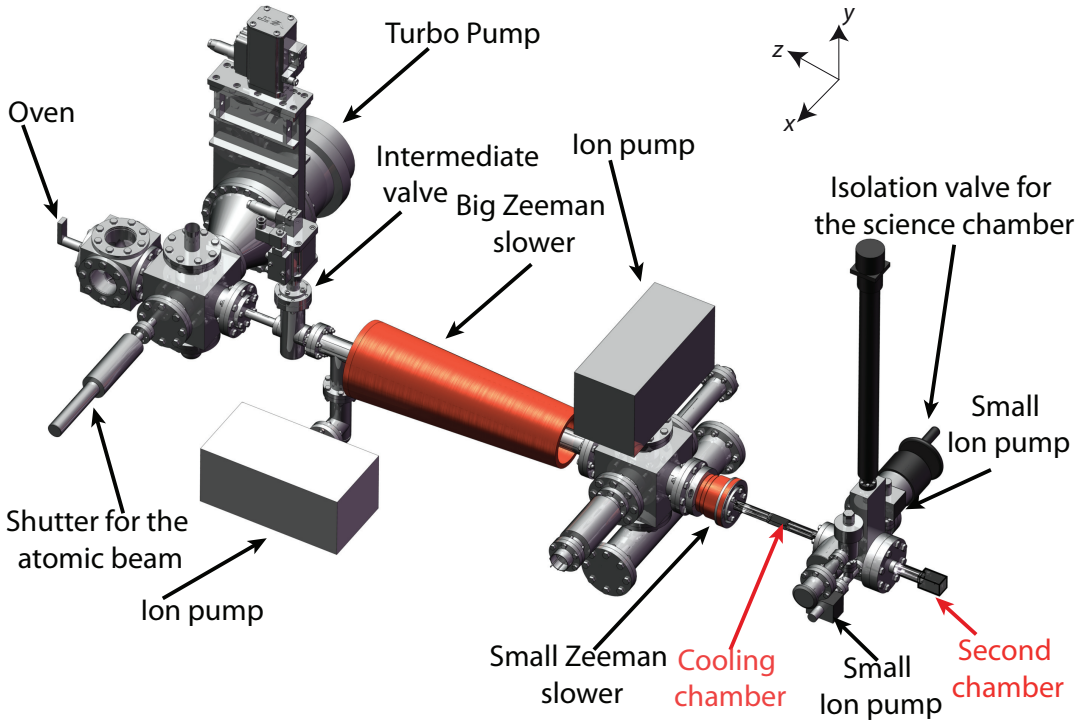

Figure 3.2: **The experimental apparatus**. We work with an ultra high vacuum ($\sim 10^{-11}$ mbar) in the cooling and second chamber to avoid collisions between the background gas and the ultra-cold atoms during the experimental cycle of $\sim$ 1min. First, we slow via the Zeeman slower the Rubidium 87 atoms coming from the oven at 120°C. Behind the slower the atoms are sufficiently slow to be capture in a magneto-optical trap. From there they are transferred into a magnetic trap where they are cooled down to ~ 1 μK by evaporative cooling. At the end of this stage the atoms are cold enough to be loaded into the optical tweezer and transported to the second chamber.

- The cooling of the atoms by laser cooling and evaporative cooling in a magnetic trap is performed in the cooling chamber as discussed in Sec. 3.3.2.
- The cloud is then transported into the second chamber by an optical tweezer, as detailed in Sec. 3.3.3.
- In the second chamber we charge the atoms in an optical dipole trap (Sec. 3.4.2) and cool them down to quantum degeneracy. It is a peculiarity of our experiment

that we can observe the expansion of the cloud after having switched off the trap up to several hundreds of ms under a magnetic levitation (Sec. 3.4.4).

- The whole setup was built in a way that we can shine in an additional fine-grained speckle disorder from two perpendicular directions. This well-controlled disorder is presented in detail in Ch. 4.

In this section we discuss the laser cooling and the evaporative cooling in the magnetic trap. However, we introduce our imaging system, allowing us to observe the atoms, in the cooling chamber at first.

3.3.1 Imaging

We characterize the atomic cloud by imaging it at the end of each experimental cycle. Two different imaging techniques exist: absorption and fluorescence imaging.

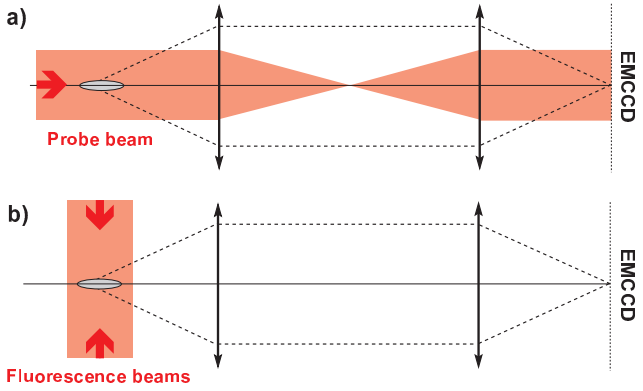

Figure 3.3: **Imaging scheme**.The cloud is imaged on the camera via an image transport. a) Absorption imaging: We measure the absorption of the probe beam at resonance by the atomic cloud. b) Fluorescence imaging: We excite the atoms by the fluorescence beams and collect their fluorescence.

In both cases we illuminate the cloud by a laser resonant with the transition $|F = 2\rangle \rightarrow |F' = 3\rangle$ for a short time: 50 μs in our case. Then, we image the cloud on a EMCCD camera using an imaging system, as shown in Fig. 3.3. This image is directly linked to the density of the of the atomic cloud, integrated over the imaging axis x:

$$n_{2D}(y,z) = \int n(x,y,z)\, dx \tag{3.33}$$

In the cooling chamber, we are using absorption imaging as it is much easier to calibrate the number of atoms with this imaging method than with fluorescence imaging. In the second chamber on the other hand, we are using fluorescence imaging in order to detect very low atomic densities (see Sec. 3.4.1). We refer the reader to the section about imaging in the great review by Ketterle et al. [Ketterle 99] for a detailed discussion of the available imaging techniques for ultracold atoms and to the thesis by Alain Bernard [Bernard 10] for a detailed discussion of the experimental setups.

3.3.1.1 Absorption in the cooling chamber

In the case of absorption imaging (Fig. 3.3 a)), the atoms are illuminated by a collimated probe beam and we measure via the imaging system the shadow created by their absorption. The detected intensity is then given by the Beer-Lambert law :

$$I(y,z) = I_0(y,z)\exp(-\sigma(\delta, I_0)n_{2D}(y,z)) \ . \tag{3.34}$$

The cross section reads

$$\sigma(\delta, I_0) = \mathcal{C}\frac{3\lambda^2}{2\pi}\frac{1}{1+4\tilde{\delta}^2/\Gamma^2}\frac{1}{1+s(\delta)} \ , \tag{3.35}$$

where $s(\delta)$ is the saturation parameter (3.26) and $\mathcal{C}$ takes into account the multi-level structure of the atom [Riou 06]. At zero detuning and weak intensities $I \ll I_{Sat}$ the cross section is approximately constant $\sigma(\delta) \simeq \sigma_0$. We can therefore deduce the column density by dividing the image of the atomic cloud by a reference image without atoms, taken directly after the first image

$$n_{2D}(y,z) = \frac{1}{\sigma_0}\ln\left(\frac{I_{ref}(y,z)}{I_{at}(y,z)}\right) \tag{3.36}$$

We postpone the introduction of the the fluorescence imaging to the presentation of the imaging setup in the second chamber in Sec. 3.4.1 and continue now the presentation of our cooling cycle.

3.3.2 Cooling

To obtain a condensate it is necessary to create an atomic cloud at very low temperature and sufficiently high density. This way it is possible to achieve a phase-space density $n\lambda_{dB}^3$ in the order of 1. Because we start at very low phase-space densities (some 10^{-15}) in the experiment, several consecutive cooling steps are needed, presented in Fig. 3.4. We distinguish three major steps : laser cooling, transfer in a trap and finally evaporative cooling. In our case, the evaporative cooling is started in a magnetic trap and then finished in an optical trap.

Starting point is a jet of atoms, that is extracted from a Rubidium vapor in an oven at 120°C. This beam of atoms is then laser cooled. For this laser cooling we use laser beams that are slightly red-detuned to the $|F=2\rangle \rightarrow |F'=3\rangle$ cycling transition of Rubidium 87.[5] The different laser cooling techniques which we apply consecutively:

- **Zeeman slowing** [Phillips 82]. We slow the jet of Rubidium 87 atoms with a counter-propagating laser beam down to 20 m/s. This allows us to capture the atoms in a magneto-optical trap.
- **Magneto-optical trap (MOT)** [Raab 87]. It consists of three pairs of counter-propagating beams (repumper + trap) and a magnetic gradient. The gradient is created by a printed circuit, leaving place for the coils of the magnetic trap. The

[5] Because the gap between $|F'=2\rangle$ and $|F'=3\rangle$ is small, the probability that the atoms falls into the dark state $|F=1\rangle$ is non-negligable . Therefore, we shine in an additional repump beam that is tuned on the $|F=1\rangle \rightarrow |F'=2\rangle$ transition to each trap beam.

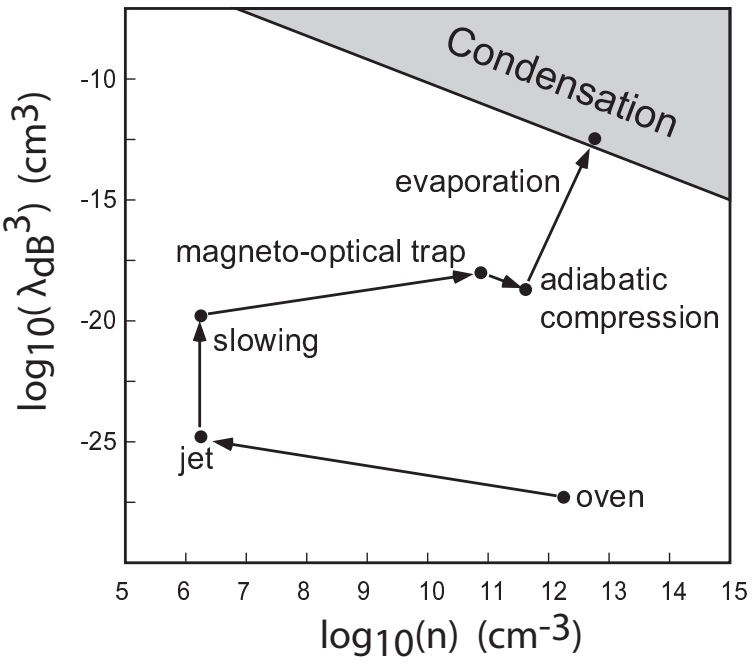

Figure 3.4: Path to condensation in the phase-space

ensemble allows us to capture and cool the atoms. We load the MOT with several 10^9 atoms in 10 s. Its typical temperature is around 500 μK. During the last 500 ms we increase the detuning of the lasers to 100 MHz in order to increase the confinement.

- **Molasses** [Lett 88, Dalibard 89]. We switch off the magnetic gradient and cool the atoms down to 50 μK in 6ms .

- **Evaporation in a magnetic trap**.[Davis 95b, Petrich 95] At the end of the molasses we pump the atoms in the $|F = 1\rangle$ state which can be trapped magnetically[6]. We switch off the laser beams and trap the atoms in the low-field seeking $|F = 1, m_F = -1\rangle$ state in the magnetic trap of Ioffe-Pritchard type [Fauquembergue 05]. We load $\sim 3 \cdot 10^8$ atoms at $T = 280$ μK in the trap (Fig. 3.5). We evaporatively cool the atoms down by effectively lowering the trap depth with a radio frequency field, a so called *rf*-knife. This way, we remove the hottest atoms from the cloud and the remaining atoms rethermalize at a lower temperature[7].

After this first cooling cycle we have created a cloud of $6 \cdot 10^7$ atoms at a temperature of ~ 1 μK.

3.3.3 Transport with an optical tweezer

Once we have finished the first cooling stage, the atomic cloud is cold enough to be trapped in the focal region of the optical tweezer, as shown in Fig. 3.6.

[6]This is done by tuning the laser on the $F = 2 \rightarrow F' = 2$ transition and switching off the repumper. The atoms can fall into the $|F = 1\rangle$ state and are accumulated in this dark state.

[7]See Sec. 3.4.2 for a more detailed discussion of evaporative cooling .

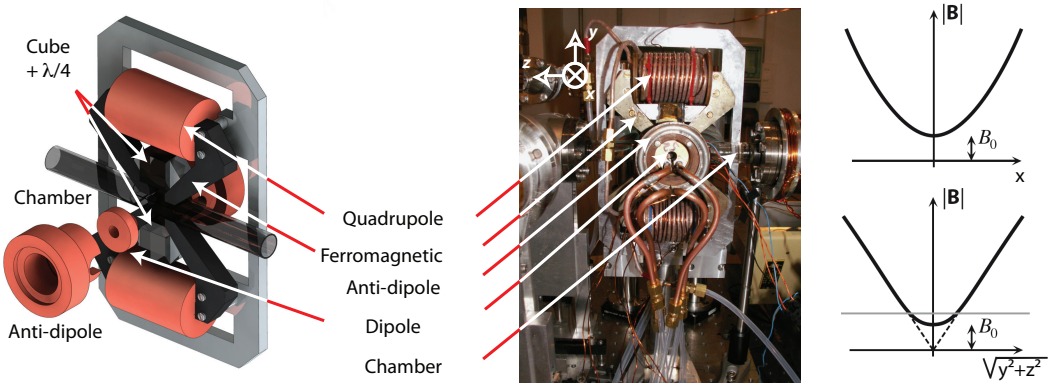

Figure 3.5: **Magnetic trap in the cooling chamber** Installation of the coils generating the Ioffe-Pritchard type. At the right, we show the norm of the magnetic field (proportional to the field felt by the atoms) in the three directions of space.

The beam is taken from a fibered Ytterbium 20W laser at $\lambda = 1070$nm (Keopsys). Here we branch off only 3W for the tweezer, the remaining power is used for the other arm of our optical dipole trap (see Sec. 3.4.2.1). We pass the beam through a single mode optical fiber with an efficiency of $\sim 70\%$ to the focalisation optics, which are mounted on a air borne translation stage (Aerotech ABL80040). The waist of the tweezer is $\omega_{0,Tweezer} = 27$ μm and its Rayleigh length $z_R = 2.4$ mm.

We characterized the tweezer in two different ways. At first we directly observed the laser profile on a camera, providing the previously mentioned waist and Rayleigh length. We can also measure the trapping frequencies in the tweezer directly by observing the dipole oscillation of the atoms in the tweezer (Fig. 3.6 b). We verified the consistency between the to methods by the relations we obtained for the gaussian beam (3.32).

To load the atoms from the magnetic trap in the tweezer, we ramp the tweezer up to $U_0/k_B = 100\mu$K in 100 ms and transfer $6 \cdot 10^6$ atoms without measurable heating into the optical trap. We capture only 10% of the atoms from the magnetic trap in the tweezer because the elongated axes of the two traps are perpendicular to each other. This is a heritage of the fact that the magnetic trap was historically designed for experiments with atom lasers [Guerin 06, Bernard 11].

Finally, we transport the cloud into the second chamber by a displacement of the focal point of the tweezer [Couvert 08, Gustavson 01]. To transport the atoms we ramp up the tweezer to its maximum power and translate it within 2.5s by 35cm. This way we obtain a cloud of $1.5 \cdot 10^6$ atoms at $T = 10\mu$K in the second chamber.[8]

3.4 The second chamber

We have discussed the steps allowing us to transport the atoms into the second chamber, where we perform later on our experiments on the propagation of ultracold atoms in a disordered light potential. This second chamber, shown in Fig. 3.7, has several peculiar

[8]This final temperature is higher than what would be induced by spontaneous emission. We suspect that it is due to mechanical vibrations of the translation stage during the transport.

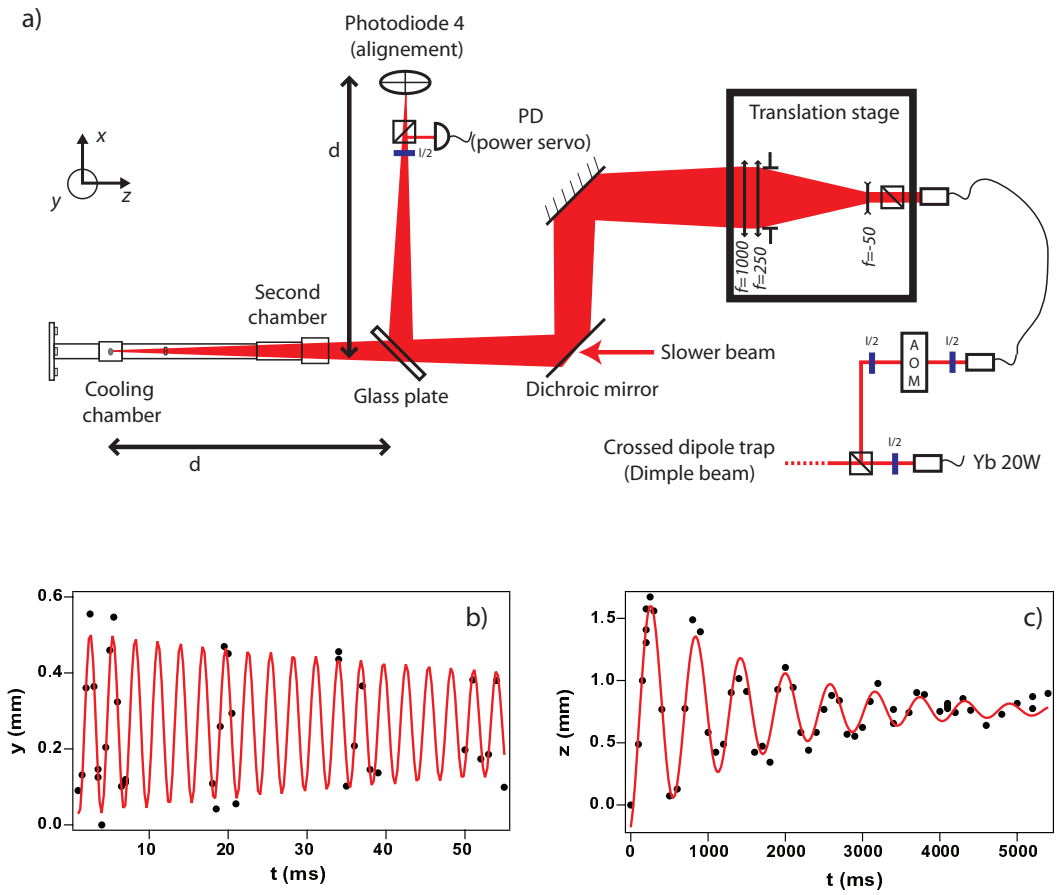

Figure 3.6: **The optical tweezer.** a) The optical path of the optical tweezer. b) Vertical and c) horizontal oscillations in the tweezer at a power of ~ 120 mW. The oscillations are triggered by a rapid switch of the MOT (vertical) or quadropole (horizontal) coils. The fit with an damped sinus provides $\omega_\perp/2\pi \simeq 350$ Hz and $\omega_{||}/2\pi \simeq 1.72$ Hz.

characteristics, which we are going to discuss in this section.

- We installed two high numerical aperture fluorescence imaging systems around the second chamber. They allow us to detect clouds with low atomic densities on two perpendicular optical axes as discussed in Sec. 3.4.1.

- We levitate the freely expanding atoms for several hundred milliseconds with a magnetic levitation (Sec. 3.4.3). Having reduced the gravitational potential by several orders of magnitude, we obtain a clean test environment for expansion in the disorder.

- We install a crossed dipole trap in this second chamber in order to cool the atoms evaporatively. This way we can cool down our atomic clouds to temperatures as low as ~ 3 nK, resulting in a Bose-Einstein condensate with a very narrow velocity distribution.

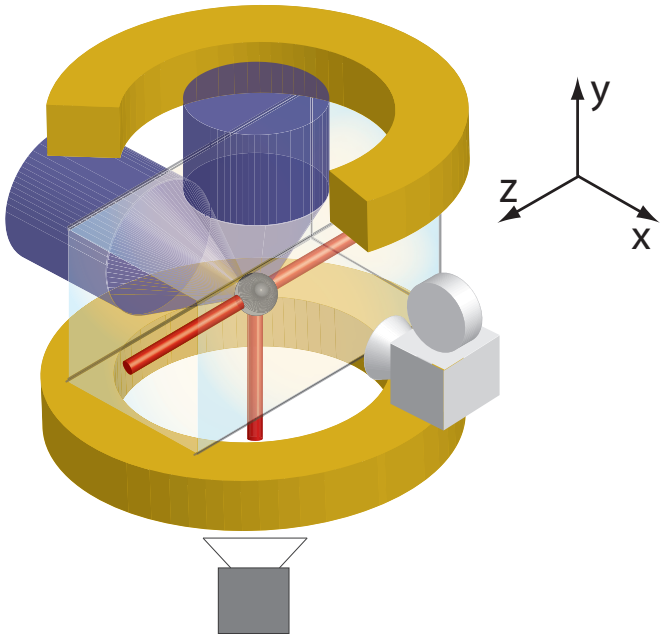

Figure 3.7: **The second chamber**. We transport the atoms in this chamber using the tweezer (horizontal red beam). The cloud is then loaded in the crossed dipole trap (intersection of red beams). We compensate gravity by a magnetic levitation. This levitation is done by 3 sets of coils, symbolized by the yellow circles here. We image the atoms in two perpendicular planes as shown by the two grey cameras. We can shine in a disordered potential, which is created by two crossed speckle fields (blue beams).

- We installed two perpendicular speckle fields around this second chamber (Ch. 4). They allow us to create a well-controlled and fine-grained optical speckle disorder, the cornerstone for our experiments on Anderson Localization.

We are going to present these characteristics in this section, except the speckle disorder which is discussed separately in the next chamber. We will finish the chapter with a characterization of the expanding matter-wave cloud with a narrow velocity distribution.

3.4.1 Imaging in the second chamber

As mentioned above, we have chosen to use fluorescence imaging in the second chamber. In order to do so, we shine in a fluorescence beam, propagating on another axis than the imaging axis (Fig 3.3 b)). The atoms can absorb the photons and reemit them in all directions. We collect the fraction of emitted photons that enters into the imaging setup

$$I_{out}(y,z) = \frac{\Omega}{4\pi}\frac{s(\delta)}{2(1+s(\delta))}\Gamma\hbar\omega_0 n_{2D}(y,z)\ , \tag{3.37}$$

where Ω is the solid angle of collection of the emitted photons. It is proportional to the numerical aperture NA of our imaging system

$$\frac{\Omega}{4\pi} \approx \frac{NA^2}{4} \tag{3.38}$$

In this case one single image of the atomic cloud is sufficient to measure the density of the atomic cloud. In contrast to absorption imaging, it is advantageous to work at high intensity here $I \gg I_{Sat}$. In this regime, the detected intensity is independent of the strength of the fluorescence beams, eliminating a possible source of fluctuations. To maximize the number of collected photons it is advantageous to work with a big NA. Additionally, we use an amplified camera to detect a weak flux of photons per pixel, that is, small atomic densities.

In contrast to absorption imaging it is not possible to relate the detected intensity directly to a number of atoms. The proportionality constant relating the two has to be determined by different measurements

- In a first step, we used the number of atoms measured with the absorption in the first chamber as reference value. Moving the atoms with the optical tweezer into the second chamber and back into the first chamber, we verified that the number of atoms before the transport, in the second chamber and after the transport are consistent.

- It is possible to shine in an absorption beam through the disorder setup. This allows to have an absorption imaging directly in the second chamber. But as the absorption beam passes through a diffuser and its intensity varies strongly this gives only an estimate.

- We can also measure the critical temperature at which a condensed fraction appears in the atomic cloud as discussed in Sec. 3.4.4. Knowing the frequencies of the trap at this point it allows to calculate the number of atoms in the cloud with Eq. (3.3).

Combining the results of those independent methods we estimate the error of our calibration to be $\sim 20\%$.

Around the second chamber we have installed two identical imaging system, which allow us to image the atoms in the x and y direction simultaneously, as presented in Fig. 3.8. For each one, we have a first optical system with a magnification of 2.5. It is constituted by an aspherical lens (focal distance $f_1 = 20mm$ and diameter $d = 22mm$) and a doublet lens ($f_2 = 50mm$). The important numerical aperture of the aspherical lens ($NA \sim 0.5$) allows to collect a high number of the photons emitted by fluorescence. Behind this first image transport we have placed a second one, which is realised by two lenses of focal distance $f_3 = 35mm$. Between these two lenses we have placed a diaphragm that allows us to control the effective numerical aperture of our imaging system.

This imaging system allows us to detect atomic clouds of $\sim 50 \cdot 10^3$ atoms and with a diameter of ~ 500 μm, meaning that we can detect densities as low as $\sim 0.1at/$ μm^2. The resolution of our imaging system should be limited by the diffraction limit ~ 1 μm. Experimentally, we measured the resolution as the size of the cloud in the compressed tweezer, directly after the transport. We obtained a resolution of ~ 6 μm (see Fig. 3.8). Moving the camera out of focus, we can estimate the depth of field to be ~ 100 μm. The effective numerical aperture is therefore < 0.1 and far from the diffraction limit. A first reason for this are certainly the aberrations of our imaging system. To be diffraction limited, we would have to design an objective that takes into account the refraction by the glass of the second chamber. Second, each atom absorbs and reemits ~ 50 photons during the exposure time. This can lead to displacements of the atoms of up to 8 μm

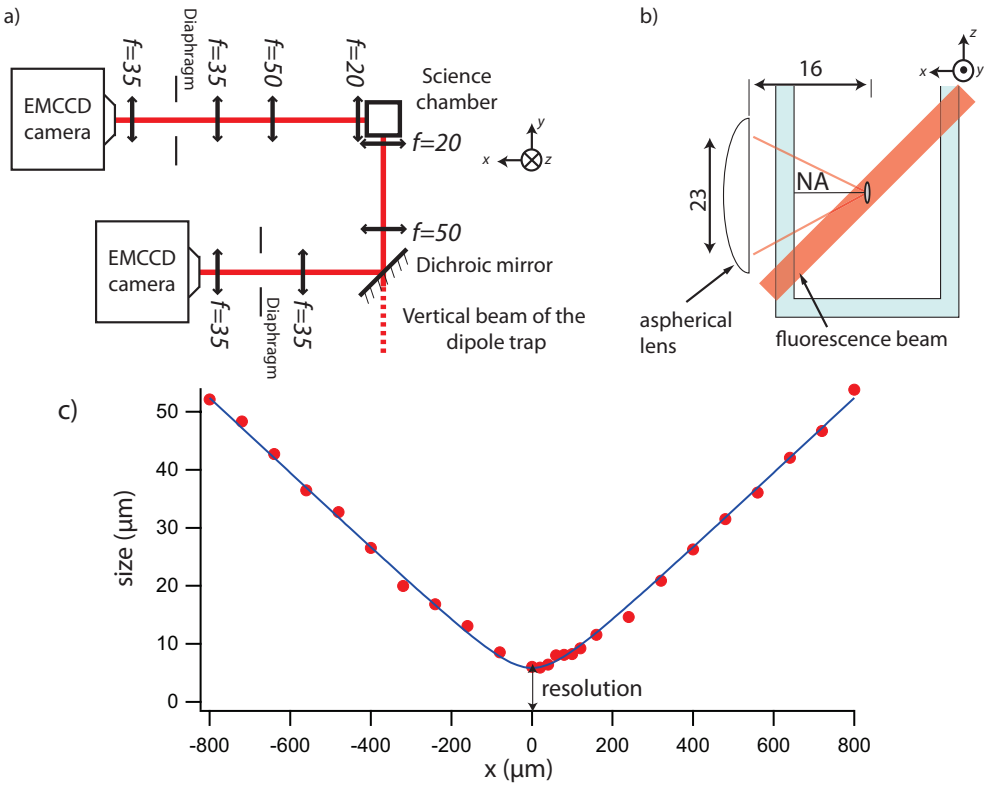

Figure 3.8: **Imaging in the second chamber**. a) Scheme of the two imaging systems in the x and y direction. b) View from top : We only show the upper imaging system here. The fluorescence beam is rotated by $45°$ with respect to the imaging axis. The first image transport introduces a magnification of 2.5 in our imaging system. c) Measured size (red points) of the atomic cloud in the tweezer. Moving the camera out of focus we measured the depth of field. The blue curve is a fit to the datas using the model of a gaussian beam (3.30).

during the exposure because of the recoil transferred by the photons. The last obvious reason is the fact, that the size of each pixel is 3×3 μm and thus only slightly smaller than our resolution. All these limitations our good reasons for the discrepancies between the diffraction limit and the experimentally observed resolution.

A current project on the experiment is the installation of a diffraction limited microscope, that will allow us to greatly increase the resolution of our imaging system.

3.4.2 Evaporation in an optical dipole trap

In order to cool the transported atoms down to a temperature of several nK while keeping a reasonable number of atoms (several 10^4) we recompress the atoms in a crossed optical dipole trap. Finally, we achieve condensation with an all-optical evaporation.

The mechanism of evaporative cooling is encountered in numerous different situations. The most common one in every day life is the cooling of a hot cup of coffee. There, we blow away the hot vapor on the top of the coffee, new vapor is formed and the remaining coffee

is colder. In general physical terms, we remove the particles with the highest energy from the system. The system of the remaining particles has a lower average-energy per particle. Once the system has gone back to thermal equilibrium, it has a lower temperature.

In our case we want to cool the atoms in a dipole trap by removing its hottest members [Hess 86, Masuhara 88, Davis 95b, Petrich 95]. We use the common approach of doing this by continuously lowering the depth of the trap [Barrett 01, Kinoshita 05, Beaufils 08, Gross 08, Clément 09, Brantut 09]. The atoms with the highest energy can escape the trap and fly away from the trapping region.

3.4.2.1 The crossed dipole trap

The crossed dipole trap consists of the superpositions between a large elongated "dimple" beam with the optical tweezer.

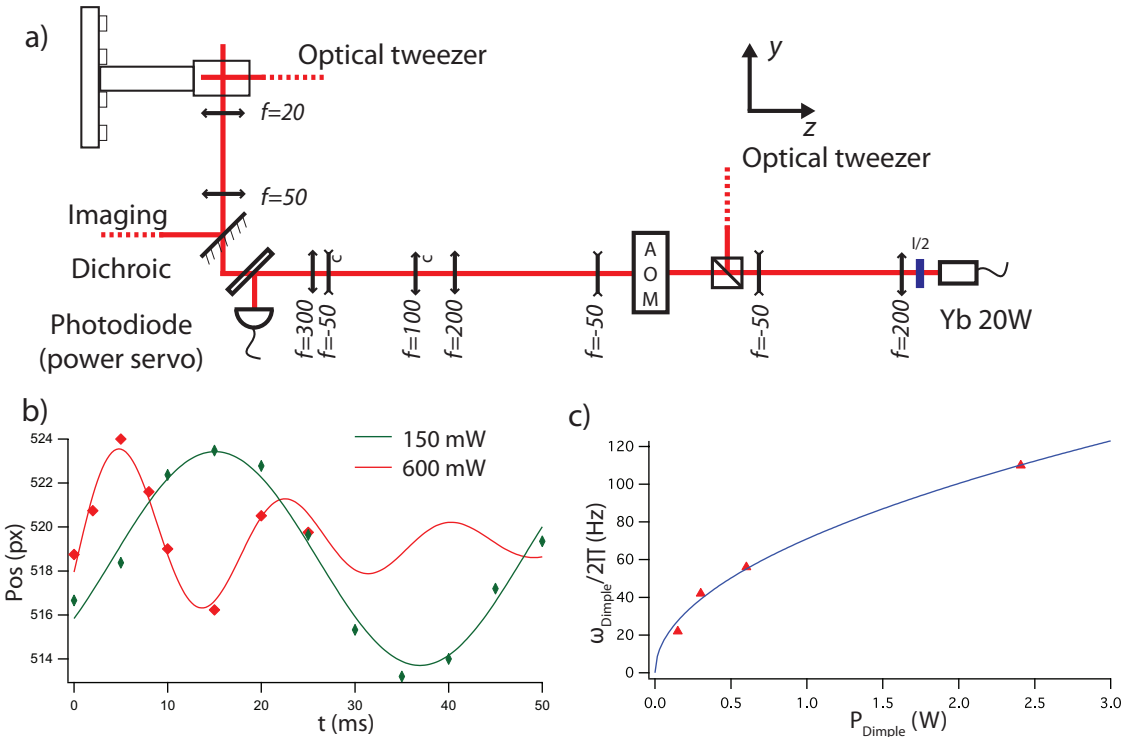

Figure 3.9: **The dimple beam**. a)Optical setup for the creation of the dimple beam. b)We characterized the dimple by dipole oscillations. The adjustment with a damped sine yields for $\omega/2\pi = 56$ Hz (for $P_{Dimple} = 600$ mW) and $\omega/2\pi = 22Hz$ (for $P_{Dimple} = 150$ mW) c) The trapping frequencies as a function of the the power in the dimple. The red dots are obtained from the fits of the dipole oscillations for different dimple strengths. The blue curve corresponds to eq. (3.32) for the waists given in the text.

We take this dimple beam off the same laser source as the tweezer (Fig. 3.9 a). It propagates on the y-axis, perpendicular to the tweezer. We chose to use an elongated beam with waists of $w_{Dimple,x} = 180$ μm and $w_{Dimple,z} = 90$ μm. This elongation perpendicularly to the tweezer simplifies the crossing of the trap. More importantly, the trapping

due to the dimple is negligible in all directions except the z-axis. This allows us to achieve an almost spherical optical trap.

We characterized the beam again in a first step by a direct observation on a CCD camera. We then measured the actual trapping frequencies of the dimple directly by dipole oscillations (Fig. 3.9 b). We triggered the oscillation by a frequency shift of the AOM signal, which displaced the center of the beam in the intended direction. For weak dimple strengths we observed a strong damping of the dipole oscillation. We attribute this damping to the fact that the atoms explore larger regions of the beam where the approximation of a harmonic trap breaks down. This strong damping also hinders us from a direct measurement of the trapping frequencies for the most decompressed configurations of trapping frequencies less than 20 Hz. Instead, we calculate the trapping frequency from the measured dimple power via the relation (3.32). We verified that the relation holds for several powers as shown in Fig. 3.9 c).

3.4.2.2 The evaporation scheme

Before we load the atoms into the trap, we decompress the tweezer down to $\omega_r/2\pi = 520$ Hz, which lowers the temperature of the atoms. Then we ramp up the dimple within 300ms to its maximal power of 8 W. This way we are able to load $\sim 7.6 \cdot 10^5$ atoms at ~ 5 μK in the trap. For reasons that will become obvious later, we also start the magnetic levitation (Sec. 3.4.3) before we begin the evaporation.

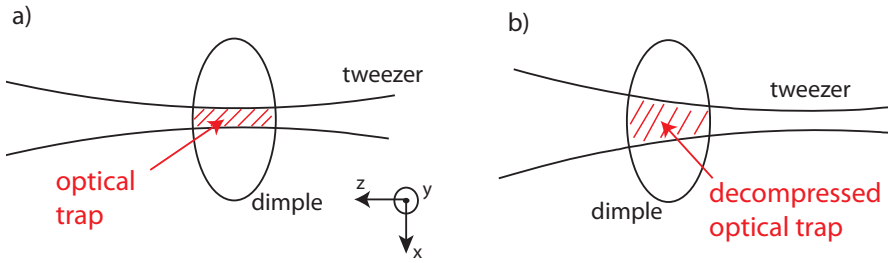

Figure 3.10: **The dipole trap**. a) The dipole trap described in Sec. 3.4.2.1 is obtained by the superposition of the optical tweezer and the dimple. b) To create a very decompressed, almost spherical trap we displace the center of the tweezer by 4.5 mm. This increases the waist of the dipole beam in the trapped region to 60 μm.

The cooling of the atomic cloud is done in two stages. The first stage of the evaporation takes place in the dipole trap described in the previous section, see also Fig. 3.10 a). This configuration yields a relatively tight confinement, which leads to high collision rates and hence to an effective evaporation (Fig. 3.11). As we lower the power of the trapping beams, the confinement of the trap decreases accordingly and the evaporation becomes ineffective at some point. To continue the evaporation, it would also be necessary to lower the power of the tweezer to some μW, which is hard to achieve in practice.

Instead, we reduce the velocity spread of the atomic cloud further by an adiabatic opening of the trap. To achieve a very decompressed trap we chose to deplace the focal point of the tweezer by 4.5mm in an intermediate step, see Fig. 3.9 b). This increases the waist of the tweezer in the trapped region to $w_{tweezer} = 60$ μm. We finish this second phase

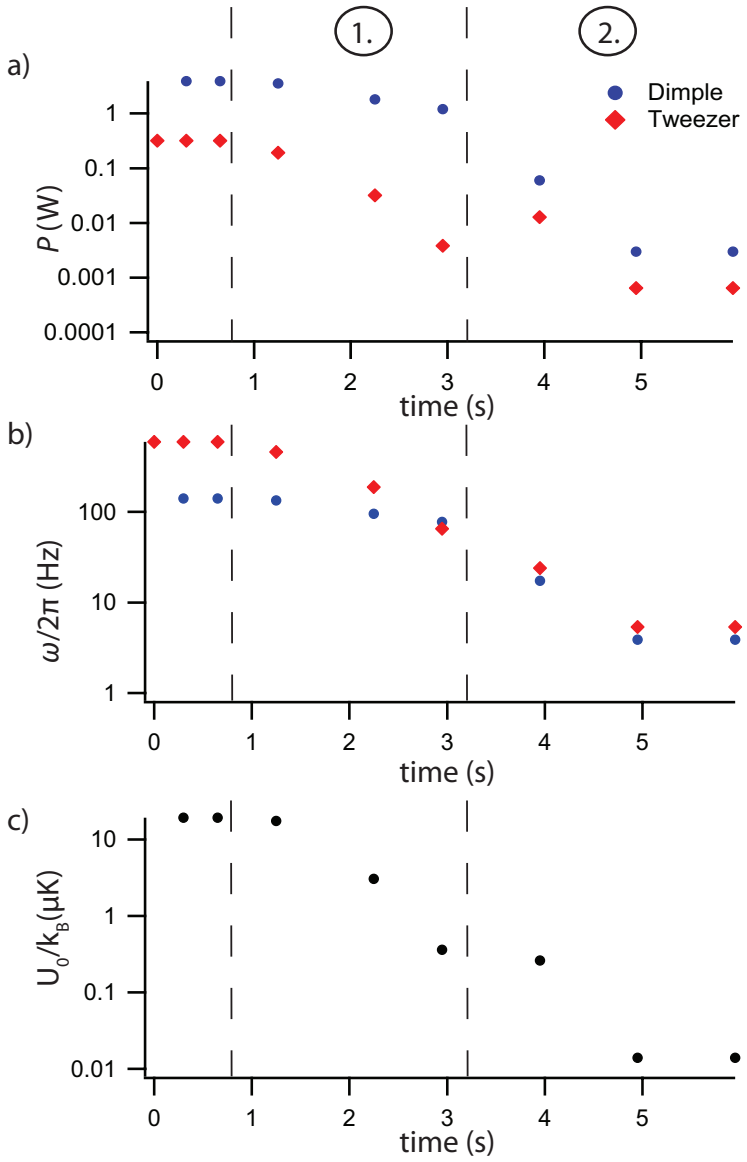

Figure 3.11: **Ramps of the evaporation**. We show the characteristics of the trap during the three phase of the evaporation: a) power of the arms, b) trapping frequencies of each arm, c) depth of the trap. At the beginning we load the atoms in the trap. In the 1. phase we evaporate in the normal optical trap. In the 2. phase we decompress the trap by translating the focal point of the tweezer and finish the cooling in this decompressed optical trap.

of evaporation after another 2.8s . The parameters of the at the end of the evaporation

and the adiabatic opening are

$$\omega_{Dimple}/2\pi = 3.9 \text{ Hz} \quad (3.39)$$
$$\omega_{Tweezer}/2\pi = 5.3 \text{ Hz} \quad (3.40)$$
$$U_0/k_B = 15 \text{ nK} \quad (3.41)$$

At this point we, can also explain the necessity of the levitation during the evaporation. Without levitation, the optical trap does not only confine the atoms in a certain region it also holds them against gravity. This induces a sag of the center of the trap $y_{Center} = g/\omega_r^2$. The trap doesn't have a minimum if the sag is bigger than $w/2$, which implies a minimum depth of the trap of

$$U_{0,min} = \frac{g m_{Rb} w}{2} \quad (3.42)$$

For a trap, with a waist of $w = 30$ μm this limits the depth of the trap to $U_{0,min}/k_B = 1.5$ μK. With the levitation, we overcome this limitation and have lowered the depth of the trap by two orders of magnitude more than it would it would have been possible without the levitation.

3.4.2.3 Characteristics of the cloud during the evaporation

To characterize the cloud, two quantities of the cloud are directly accessible to us during the evaporation. We can measure the number of atoms N by direct imaging (see Sec. 3.4.1) and the temperature T by time-of-flight (TOF) experiments, which are discussed in some detail at the end of this chapter (see Sec. 3.4.4). The evolution of the temperature and the number of atoms is shown in Fig. 3.12 a) and b). From those values and the independently measured trapping frequencies, we can also calculate the phase-space density via the relation (3.2) (Fig. 3.12).

Amongst others, the PSD gives us a very convenient way to analyze the efficiency of our evaporation ramps. In the trap the PSD scales with the number of atoms by a power-law [Walraven 10, Brantut 09].

$$D \propto N^{-\gamma} \quad (3.43)$$

We illustrate this evolution of the phase-space-density as a function of the number of atoms in Fig. 3.13. It nicely shows the power-law dependance. The measured exponent of $\gamma = 2.8 \pm 0.3$ is in good agreement with the theoretical predictions [Walraven 10, Brantut 09], which indicates that the evaporation ramps are well optimized.

As mentioned earlier, we characterize the cloud by time-of-flight experiments. Those ToF experiments require typical time scales of several $1/\omega \sim 50$ ms . Such long expansion times are accessible to us only by the magnetic levitation. Therefore, we will treat the magnetic levitation before we discuss those expansions in Sec. 3.4.4.

3.4.3 The magnetic levitation

To compensate gravity several approaches are possible. We could have tried to make a "free-falling" experiment. During the fall the atoms are in the inertial frame as the experiment without being held against gravity and evolve freely. Several experiments have taken this approach. At the tower of Bremen the experiment falls for several seconds

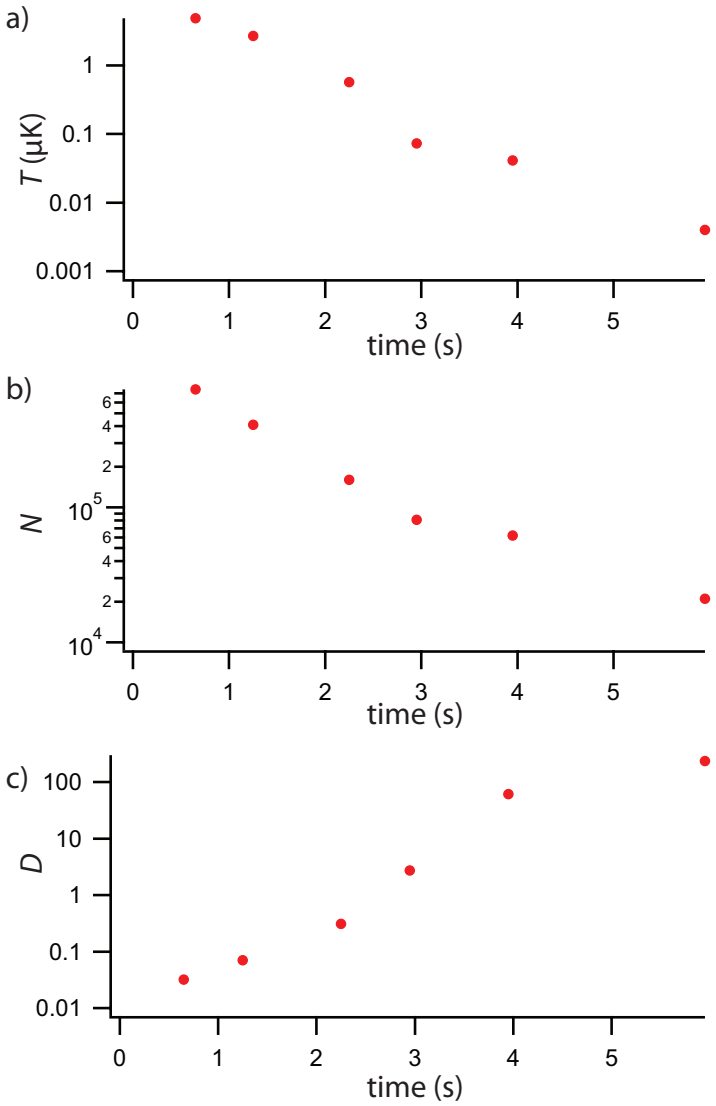

Figure 3.12: **Characteristics of the atomic cloud during the evaporation**. a) The temperature measured by time-of-flight experiments. b) The atom number. c) The phase-space-density deduced from Eq. (3.2)

[van Zoest 10]. The ICE experiment of our group is loaded in a zero-g plane which provides the possibility to cancel out gravity for 22s [Geiger 11]. An experiment in a satellite is still in the construction phase [Laurent 06]. All these approaches provide an extremely clean test environment, but they are in general costly and imply high constraints on the set-up. As we do not need the high quality of compensation provided by these techniques, we have chosen a simpler and cheaper approach on our experiment by using a magnetic levitation.

We compensate gravity with a magnetic gradient field. This introduces additional gradients in the other directions, as the magnetic field has a conserved flux. So residual

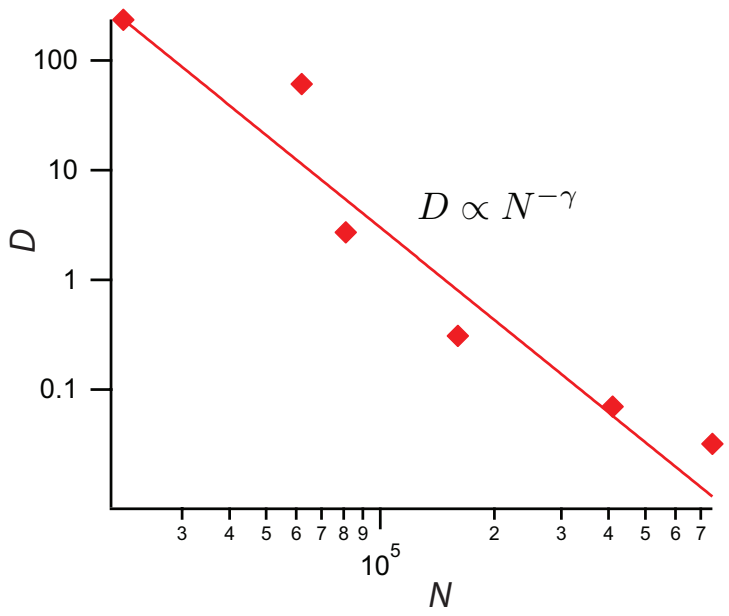

Figure 3.13: **Phase-space-density vs Number of atoms**. The red dots are experimental values. The red line is a fit of the form $D = A \cdot N^{-\gamma}$ with $\gamma = 2.8 \pm 0.3$.

inhomogeneities of the field will always persist. However, the atoms are only sensitive to the amplitude of the magnetic field as the spin of the atoms follows to the direction of the magnetic field lines at the Larmor frequency. By adding a bias field, we can diminish the influence of the gradients inthe transverse directions, see Fig. 3.14. Indeed, it can be shown that residual trapping frequencies in a harmonic approximation are limited by the following law [Sackett 06]

$$\sum_i \omega_i^2 \geq \frac{\mu b'^2}{2mB_0} \text{ with } b' = \frac{mg}{\mu} \ , \tag{3.44}$$

where we can calculate $\mu = \frac{\partial E}{\partial B}$ from Eq. (3.23) .

3.4.3.1 A model of our levitation

Before we discuss the actual experimental implementation of the levitation, we want to show here the simple idea behind it and that it should actually be limited by (3.44).

The simplest experimental solution is to create the gradient by a pair of coil with opposed current I_G creating a magnetic field [Fauquembergue 07] gradient b'. A second pair of coils with currents flowing in the same direction will create the necessary bias field B_0 and a curvature b''. The total field is then

$$\mathbf{B} = \left(B_0 + b''(y^2 - r^2/2) + b'y\right)\ \mathbf{e}_y - \left(b'r/2 + b''ry\right)\ \mathbf{e}_r \tag{3.45}$$

The development of the norm of the magnetic field to second order leads to

$$B \simeq B_0 + b'y + y^2 b'' + r^2 \left(\frac{b'^2}{8B_0} - \frac{b''}{2}\right) \ , \tag{3.46}$$

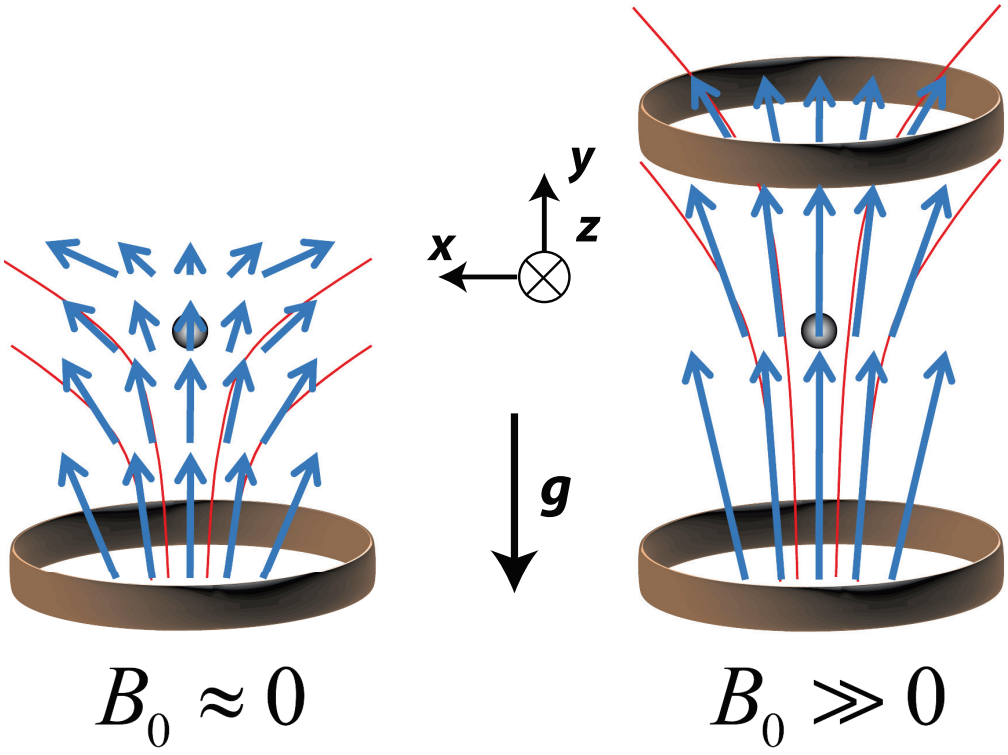

Figure 3.14: **Principe of the magnetic levitation**. a) The gradient used to compensate gravity always introduces gradients in the other directions. b) As we are only sensible to the norm of the field we can reduce the effect by adding an strong bias field B_0.

with the associated frequencies

$$\omega_y^2 = \mu/m \cdot 2b'' \text{ and } \omega_r^2 = \mu/m \cdot (b'^2/4B_0 - b'') \tag{3.47}$$

Thus condition (3.44) is exactly verified in this setup. We deduce from (3.47) that the residual trapping is isotropic, if we satisfy the condition

$$b'' = \frac{b'^2}{12B_0} \tag{3.48}$$

The magnetic gradient is fixed as it has to cancel out the gravitional potential

$$b' = \frac{mg}{\mu} \tag{3.49}$$

Using (3.49) and (3.48), the residual frequency reads

$$\omega_{res}^2 = \frac{mg^2}{6\mu m B_0} \tag{3.50}$$

This isotropic magnetic potential forms a trap if $\mu > 0$ and it is expelling if $\mu < 0$.

3.4.3.2 Experimental implementation

As b'' and B_0 are generated by the same current, they are not independent but linked via the geometry of the set of bias coils [Fauquembergue 07]. This means that the strength of the bias field and thus the residual frequencies of the levitation are fixed by the isotropy condition, once we have installed the coils. To overcome this limitation, we use two sets of bias coils each one being close to a Helmholtz configuration, see Fig. 3.15. Their total magnetic field can be seen as coming from a single "effective" bias coil with a changing effective distance L_{eff}, which depends on the ratio between the currents I_{ext} and I_{int} in each of the bias coils.

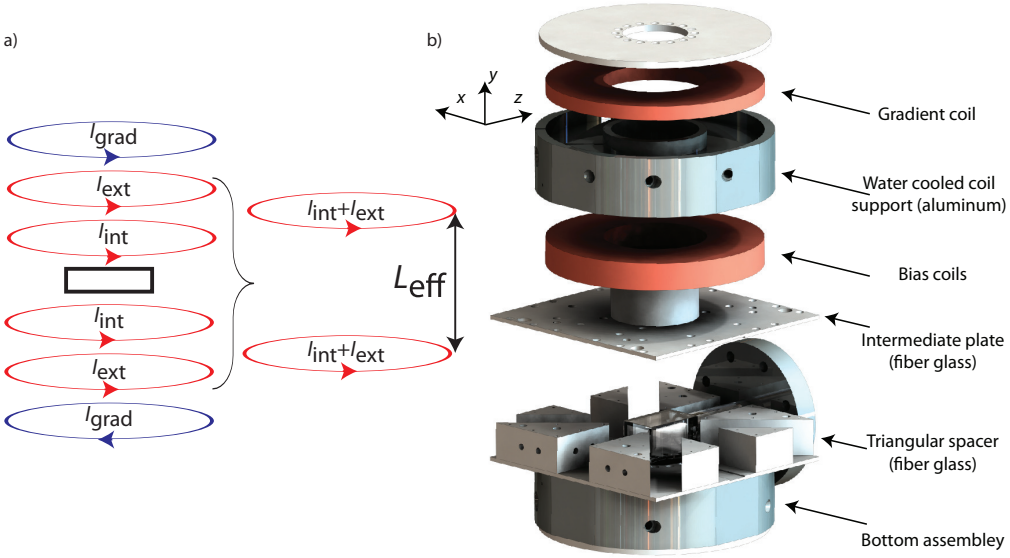

Figure 3.15: **The magnetic levitation**. a) Current scheme: We control the gradient by the current I_{Grad} in the gradient coils. The bias field is controlled by I_{Ext} and I_{Int} in the two pairs of bias coils. By changing the ratio between those we can control the effective distance L_{eff} of the set of bias coils. b) The design of our levitation. Each coil has 64 turns. The support is made of aluminum in order to dissipate the heat easily and it is additionally water-cooled.

The actual design of our levitation is shown in Fig. 3.15 b). It is composed of three pairs of coils, designed to fit precisely in an aluminum support, which serves as water-cooled radiator. [9] Each coil has $N = 68$ turns of copper wire (2 layers of 34 turns each). The bias coils are placed next to the second chamber, as we want them to create the highest fields. They are fet by stable power supplies ($\Delta I/I \approx 10ppm$), able to generate currents up to $I_B = 200A$. The gradient coils are placed outmost and controlled by a power supply delivering up to $I_G = 50A$. This way we can create bias fields up to $B_0 = 2000G$ and a magnetic gradient up to $b' = 30G/cm$.

We tested the quality of our levitation with expansion experiments, described in the

[9] The coils were developed and fabricated in collaboration with Michel Lecrivain from the SATIE laboratory.

following section.

3.4.4 Expansion of the BEC

In this final section, we discuss the ToF-experiments we performed with our condensate. The interest of them is twofold. On one hand they allow us to characterize precisely the magnetic levitation. Further, they allow us to precisely determine the properties of the atomic cloud like the tempature or the condensation ration in the trap.

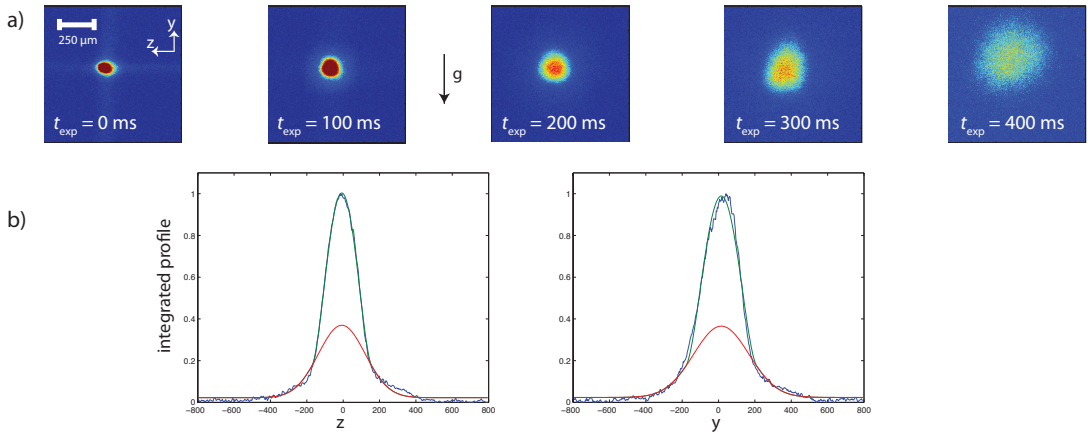

Figure 3.16: **Expansion of the Bose-Einstein condensate**. The atoms are in the $|F = 2, m_F = -2\rangle$ state and the magnetic potential is anti-trapping with $\omega_{res} = -0.5$ Hz a) Fluorescence images of the expanding cloud for different expansion times t_{exp} b) Integrated profiles of the expanding cloud at $t_{exp} = 300$ ms in the z and y direction. The blue line is the measured profile. The green line, describing the parabolic shape of the condensed fraction and the red line, describing the thermal part, are fits to the experimental datas.

Having created our BEC as described in Sec. 3.4.2, we can cut the trap and let the cloud expand in the levitating potential as shown in Fig. 3.16 a). We perform those experiments most of the time with an atomic cloud in the $F = 2$ $m_F = -2$ ground state.[10] This provides us with an expelling magnetic levitation and the necessary strength of the gradient field is independent of the bias field B_0.

We can see a quasi-isotropic expansion of the cloud for several hundred milliseconds. In this time the center of the cloud has moved by ≈ 100 μm, which means that we have compensated the residual gradients up to $10^{-4}g$, where $g = 9.81\text{m/s}^2$. For intermediate times ($t_{exp} \sim 100$ ms), one can see a double structure emerging in the density profile. This is a characteristic feature of an expanding condensate surrounded by the thermal atoms in the wings [Anderson 95, Davis 95a].

The projection of these profiles in the directions z and y provides us with the characteristic properties of the cloud (see Sec. 3.1.3.1). The thermal wings are well described by a gaussian of of rms $\sigma_{Th}(t_{exp})$. The condensed part at the center of the cloud has the

[10] After the transport the atoms are in $|F = 1, m_F = -1\rangle$ state and we transfer them via an rf-sweep at $B_0 \sim 5$G in $t_{Sweep} = 200ms$ with a sweep range of $1MHz$. The transfer efficiency is $> 90\%$.

form $n_c(u, t_{exp}) = n_c(0) \cdot \max\left(1 - u^2/u_0^2(t_{exp}), 0\right)^2$, where $u \in y, z$. Fig 3.16 b) shows that this double structure applies well to the observed profiles. From those fits we estimate that $\geq 50\%$ of the $N_{at} \simeq 25000$ atoms are contained in the condensate.

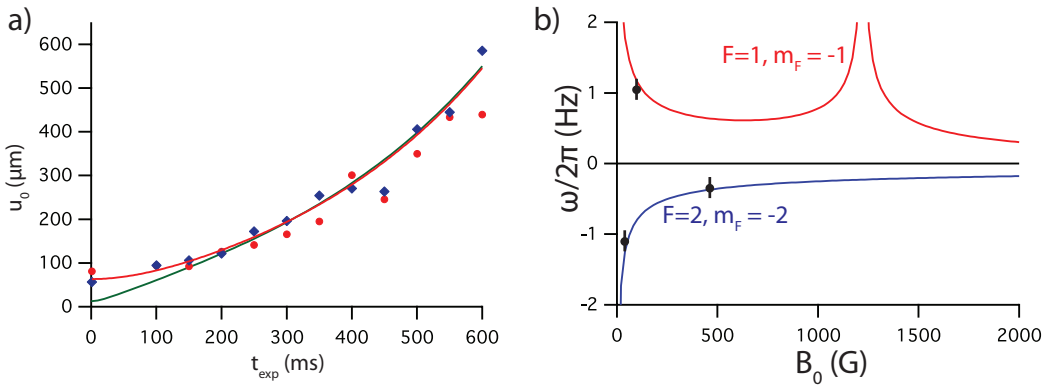

Figure 3.17: **Time evolution of the condensate**.a) Evolution of the radius of the condensate. The points mark the experimental datas in vertical (blue) and horizontal (red) direction. The red line is a fit to the experimental datas. The green line results from the scaling approach without free parameters. b) Residual frequencies of the magnetic levitation. The continuous lines are the predictions of the model presented in Sec. 3.4.3. The black dots are obtained from the ToF - experiments as described in the text.

Further, we can analyze the time evolution of the radius of the condensed fraction $u_0(t_{exp})$, shown in Fig. 3.17 a). In a first step, we can treat it with a simple classical, phenomenological model. Supposing that the velocity of the atoms is independent of their position at the beginning of the expansion we can describe the expansion by

$$u_0(t) = \sqrt{u_0(0)^2 \cosh^2(\omega_{res} t_{exp}) + \left(\frac{v_{i,max}}{\omega_{res}}\right)^2 \sinh^2(\omega_{res} t_{exp})}\ , \tag{3.51}$$

where $v_{i,max}$ is the maximum velocity of the atoms in the condensate. Applying this model to the expansion of the cloud yields a direct measurement of the maximum velocity $v_{max} = 0.5$ mm/s and the expulsion $\omega_{res}/2\pi = 0.5$ Hz. With (3.20) we can then directly calculate the chemical potential $\mu_{in}/h = 40$ Hz. To verify the validity of these measurement we compared them to other independent models.

First, we performed such expansion experiments for different strength of the bias field B_0 and in different magnetic substates. In Fig. Fig. 3.17 b), we compare the results from those expansions to the model of the residual frequencies (3.50) which was presented in the previous section. Given the simplicity of the two independent models, the agreement between them is quite good.

In a second step, we verified that the observed expansion is compatible with the predictions of the scaling approach we discussed in Sec. 3.1.3.1. We can identify the measured radius with the time-evolving Thomas-Fermi radius and use the scaling relations (3.16). Neglecting the slight anisotropy of the initial trap, they yield

$$u_0(t) = b(t) \cdot u_0(0) \tag{3.52}$$

$$\text{with } \frac{d^2 b(t)}{dt^2} = \frac{\omega_{Trap}^2}{b^4} - \omega_{res}^2 b(t) \tag{3.53}$$

We solved this equation numerically using the independently known trap frequency ω_{trap} and residual expulsion of the levitation ω_{res}. Fig. 3.17 a) shows the good agreement between this independent theoretical prediction and the experimental observations. For short times we observed that the measured radius of the condensate is systematically larger than the predictions. We believe that this is due to problems of the imaging, which are known to arise in dense atomic clouds. A detailed study of the problem had to be left to future investigations.

Finally, we can measure the temperature of the cloud from the mean velocity of the thermal wings. To extract this mean velocity we applied the simple model (3.51) to the time evolution of its width $\sigma_{Th}(t_{exp})$. That way we estimated the temperature of the cloud to be $T = 3$ nK.

Those expansion experiments have allowed us therefore to measure directly the following characteristics of the condensate :

$$N_{at} = 25000 \tag{3.54}$$
$$T/k_B = 3 \text{ nK} \tag{3.55}$$
$$v_{Max} = 0.5 \text{ mm/s} \tag{3.56}$$
$$\mu_{in}/h = 40 \text{ Hz} \tag{3.57}$$

3.5 Conclusion

In this chapter we have explained our experimental set-up which allows us to observe the expansion of ultra-cold atomic clouds in a clean test environment and with an important optical access on several axes. The transport of the atoms out of the cooling chamber enabled us to spatially separate the laser-cooling set-up and Ioffe-Pritchard trap from experimental region in the second chamber. This way, we were able to install a well-performing magnetic levitation and the fluorescence imaging on several axes, still leaving space for the installation of the speckle disorder.

CHAPTER 4

Characteristics of a three-dimensional speckle disorder

One of the major interests of using ultracold atoms for the study of Anderson Localization stems from the great flexibility and control of the disordered potentials in which the atoms evolve. Several methods allow to create disorders of this type. A lattice can be perturbed by the presence of a different species of atoms, confined in the wells [Gavish 05, Massignan 06]. These atoms are then playing the role of the impurities in the system. It is possible to use bichromatic optical lattices, whose chosen frequencies are incommensurate. This way the atom is propagating in a potential with broken translation symmetry. The dynamics in such a quasi-disorder is described by the André-Aubry model [Grempel 82, Roth 03].

In our experiments we have chosen to create the three-dimensional disorder by an optical *speckle potential*. It corresponds to the spatially random intensity distribution that results from the coherent diffraction of a laser on a rough surface. The atoms placed in such a light field feels a optical dipole potential $V(\mathbf{r})$, directly proportional to the laser intensity and thus spatially random. As the statistical properties of such a speckle field are known [Goodman 07], the dipole potential created by it is perfectly controlled [Clément 06], whether for its correlation or the distribution law of its amplitude.

In this chapter we are going to discuss in a first step the general properties of such a speckle disorder. We will then introduce the most important quantities to characterize a disorder. The intensity distribution $P(I)$ describes the probability to encounter a specific intensity I. The correlation function $C(\delta\mathbf{r})$ and power spectral density allow us to quantify the size of the grains in the different directions by the correlation length $\sigma_{R,i}$. In this context we will understand that the speckle is a correlated disorder formed by anisotropic elongated grains.

Finally, we will show how we have reduced this anisotropy by an interference of two perpendicular speckle fields. We will discuss the properties of this superposition and how they are controlled by the interference between the two fields.

4.1 The speckle - a well-controlled, correlated disorder

The speckle is a spatially random intensity distribution that results from the coherent diffraction of a laser on a rough surface. Depending on the setup, the diffraction can take place in reflection or transmission. On our experiment, we have decided to work in transmission (Fig. 4.1): the laser beam is diffracted during its propagation through a frosted glass whose thickness varies randomly. This can be seen as a large number of diffusing elements, emitting waves randomly dephased against each other. The interferences between

these waves, destructive or constructive depending on the point **r** of the speckle field we are looking at, are at the origin of the spatially random intensity distribution.

4.1.1 Simple model of the speckle as an diffraction picture

As mentioned above, the speckle field is obtained by the diffraction of a laser beam propagating through a frosted glass with variable thickness $\delta e(\alpha, \beta)$, where (α, β) denote the position on the diffuser. The diffraction of an incident plan wave with amplitude a_0 gives rise to a wave, directly behind the diffuser, with amplitude :

$$a(\alpha, \beta) = a_0 e^{i\delta\phi} \text{ with } \delta\phi(\alpha, \beta) = \frac{2\pi}{\lambda}(n-1)\delta e(\alpha, \beta) \ , \tag{4.1}$$

where λ is the wavelength and n the optical index of the plate. The diffraction figure is perfectly random if the dephasing is uniform over $[-\pi, \pi]$, which imposes that the typical variance of the diffuser width is greater than $\lambda/(n-1) > 1 \ \ \mu$m. Under this condition, which is largely respected in practice, a speckle pattern is called "fully developed". Then, the diffraction will depend essentially on the size of the defects on the diffuser, characterized by the correlation length r_C.

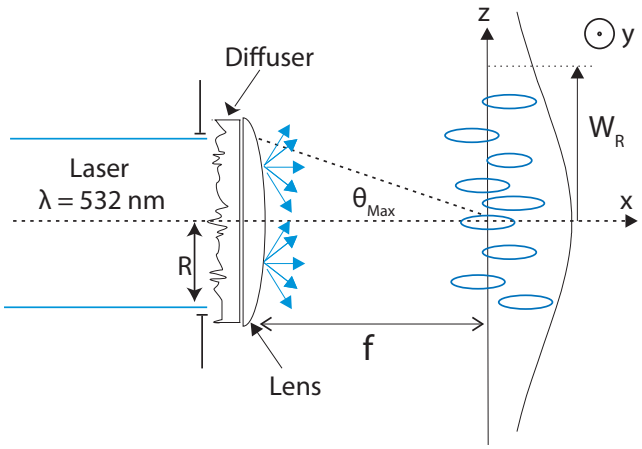

Figure 4.1: **Realisation of a speckle**. The diffuser diffracts the laser beam of radius R and the speckle is obtained around the focal point of the convergent lens with focal distance f. The numerical aperture $NA = \sin\theta_{Max}$ of the system gives the size of the speckle grains in all directions. In our case, the speckle pattern has a gaussian envelope with a waist $w_R = f\theta_{Diff}$, where θ_{Diff} is the diffraction angle of our diffuser.

In the following, we consider the case of a fully developed speckle, obtained in the focal plane of a convergent lens with focal distance f. (Fig. 4.1). The diffracted amplitude around the focal point $A(x, y, z)$ is given in the paraxial approximation ($f \gg D$) by:

$$A(x, y, z) = \frac{e^{ik(f+x)}}{i\lambda f} \int d\alpha \ d\beta \ a(\alpha, \beta) e^{-i\frac{kx}{2f^2}(\alpha^2+\beta^2)} e^{-i\frac{k}{f}(y\alpha+z\beta)} \tag{4.2}$$

Following the book by J.W. Goodman [Goodman 07], we derive the properties of the speckle pattern from the diffracted amplitude (4.2). Following the notations of Fig. 4.1,

the numerical aperture is given by :

$$NA = \sin\theta_{Max} = \frac{R}{\sqrt{R^2 + f^2}} \tag{4.3}$$

4.1.2 Physical model of the speckle

Before we enter into the details of the calculations, we will see that we can understand the essential properties in terms of interference between multiple waves.

We can see the diffuser, characterized by its correlation length r_C, as an ensemble of a large number of independent defects, with fixed size r_C, but randomly varying thickness. The diffracted amplitude by each defect is essentially contained in a cone of angle $\theta_{Diff} = \lambda/r_C$, which gives an intensity distribution with a width $\sim f\lambda/r_C$ in the focal plane. In the focal plane of the lens, the diffraction patterns are all perfectly superposed and create the envelope of the intensity distribution. Therefore, its extension depends only on the size of the defects r_C. The interferences between the defects, on the other hand, will create a modulation in the interior of this envelope. If the defects are small compared to the size of the diffuser ($r_C \ll D$), the total extension of the envelope will be large compared to those modulations, called speckle "grains".

In the speckle pattern, all defects contribute equally to the total amplitude A at a given point in the focal plane, only their phase varies randomly. Therefore, we can replace the integral in (4.2) by a discrete sum of the form:

$$A = \frac{a_0}{\sqrt{N}} \sum_{n=1}^{N} e^{i\phi_n} \ , \tag{4.4}$$

where $N = D/r_C$ and the phases ϕ_n are independent and randomly distributed over $[-\pi, \pi]$. Thus, we can interpret the speckle pattern as the result of the interference between N detects distributed over the diffuser. In analogy with the diffraction pattern of a lattice, we can also deduce that the transverse size of the grains will correspond approximatively to the diffraction limit $\lambda/2NA$ given by the size of the diffuser. Locally, we can see each of these grains as an emitter of size $\lambda/2NA$. Each elementary emitted beam stays parallel over the Rayleigh distance. Beyond this, the beam diverges, mixes with the beams coming from the other grains and the correlation is lost. Therefore, the longitudinal size of the grains will correspond approximatively to the Rayleigh length $2\lambda/NA^2$. We will establish these results more rigorously in the following. [1]

4.1.3 Intensity distribution

According to (4.4), the diffracted amplitude A is a sum of $N \gg 1$ random variables. The central limit theorem can then be applied: from this we conclude that probability law of the amplitude is gaussian. As the intensity of the diffracted wave is given by $I = |A|^2$, its

[1] Let us insist on the fact that the above supposes that all defects contribute really at each point of the speckle, a condition that is perfectly fulfilled in the focal plan of the lens. If the lens has now some aberrations, this will slightly displace the diffraction pattern of each scatterer against the others. But this effect is normally completely negligible, as the displacement is extremely small compared to the size of the intensity spot. Therefore, the properties of a speckle figure are rather independent to aberrations of a lens.

distribution is exponential and it is given by [Goodman 07]:

$$P(I) = \frac{1}{\bar{I}} e^{-I/\bar{I}} \ , \tag{4.5}$$

where $\bar{I}$ is the average intensity and turns out to be equal to the standard deviation of the intensity σ_I. Therefore, the contrast defined by $C = \frac{\sigma_I}{\bar{I}}$ is always equal to 1 for a speckle figure. We want to insist here on the fact that the intensity distribution depends uniquely on $\bar{I}$, which makes the speckles particularly interesting for experiments : the measurement of the average intensity alone allows us to know the complete intensity distribution of the speckle.

In the case of a large detuning, Eq. (3.28) is valid and the amplitude of the disordered potential V_R is directly related to $\bar{I}$ by

$$V_R = \frac{\hbar \Gamma^2}{8 \tilde{\delta} I_{Sat}} \bar{I} \tag{4.6}$$

4.1.4 Spatial properties and dimensions of a speckle grain

The spatial variations of the speckle field is quantitatively characterized by its correlation function and its spectral power density. In this section we are interested in its characteristics in the paraxial approximation. We further suppose that the correlation radius of the defects on the diffuser is infinitely small: the speckle figure is extended over the whole space and its statistical properties are translation invariant. This approximation is well justified around the focal point for distances much smaller then $f\theta_{Diff}$.

4.1.4.1 Auto-correlation function

The auto-correlation function is defined by $\Gamma_I(\delta \mathbf{r}) = \langle I(\mathbf{r}) I(\mathbf{r} + \delta \mathbf{r}) \rangle$. Because the mean value of this correlation function does not have any importance to us, we are interested in the following in the connected correlation function:

$$\Gamma_{\delta I}(\delta \mathbf{r}) = \Gamma_I(\delta \mathbf{r}) - \bar{I}^2 \tag{4.7}$$

This function is a correlation function of fourth order of the amplitude A, given by (4.2). As the amplitude is a gaussian variable we can apply the Wick theorem and rewrite $\Gamma_{\delta I}$ as a function of Γ_A:

$$\Gamma_{\delta I}(\delta \mathbf{r}) = \bar{I}^2 \left| \frac{\Gamma_A(\delta \mathbf{r})}{\Gamma_A(0)} \right|^2 \tag{4.8}$$

Thus, we need to calculate the correlation function of the amplitude. In the transverse direction $\Gamma_{A,\perp}(\delta y, \delta z) = \Gamma_A(\delta x = 0, \delta y, \delta z)$ and in the longitudinal direction $\Gamma_{A,||}(\delta x) = \Gamma_A(\delta x, \delta y = 0, \delta z = 0)$ it takes the simple form:

$$\Gamma_{A,\perp}(\delta y, \delta z) = \int d\alpha \ d\beta \ I(\alpha, \beta) e^{-i \frac{k}{f} (\delta y \alpha + \delta z \beta)} \tag{4.9}$$

$$\Gamma_{A,||}(\delta x) = \int d\alpha \ d\beta \ I(\alpha, \beta) e^{-i \frac{k \delta x}{2 f^2} (\alpha^2 + \beta^2)} \ , \tag{4.10}$$

where $I(\alpha, \beta)$ is the intensity distribution on the diffuser.

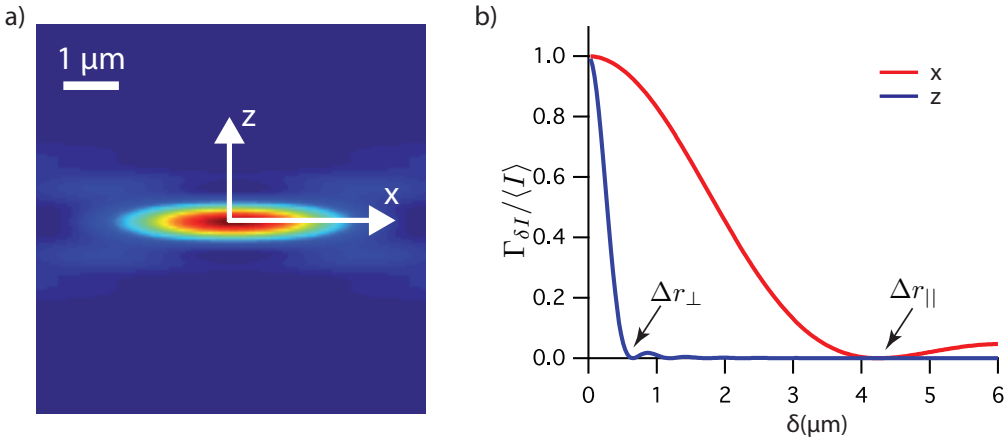

Figure 4.2: **The correlation function of a speckle**. a) The complete correlation function for a numerical aperture $NA = 0.5$ and a wavelength $\lambda = 532$ nm. b) Cuts of the correlation function in transverse (z) and longitudinal direction (x).

4.1.4.2 Transverse direction

In the transverse direction the connected intensity correlation function is directly proportional to the square of the Fourier transform of the intensity $I(\alpha, \beta)$. In the case of a uniform intensity distribution on the diffuser, the dimension of each grain corresponds to the diffraction limit for the numerical aperture given by the diffuser. Let us consider the case of a circular diffuser, as implemented in the experiment, with radius R. Its transverse correlation function is given by :

$$\Gamma_{\delta I,\perp}(\delta y, \delta z) = \bar{I}^2 \left| \frac{\lambda}{\pi NA\ \delta r} J_1\left(\frac{2\pi NA\ \delta r}{\lambda}\right)\right|^2 \text{ with } \delta r = \sqrt{\delta y^2 + \delta z^2}\ , \tag{4.11}$$

where J_1 is the Bessel function of first kind. The size of a grain is commonly defined as the distance to the first zero

$$\Delta r_\perp = 1.22\frac{\lambda}{2NA} \tag{4.12}$$

This is an essential result for the speckle : The transverse size of the grain is the diffraction limit.

4.1.4.3 Longitudinal direction

In the longitudinal direction we obtain for a circular diffuser:

$$\Gamma_{\delta I,||}(\delta x) = \bar{I}^2 \text{sinc}\left(\frac{NA^2}{2\lambda}\delta z\right)^2 \tag{4.13}$$

As for the transverse direction, we define the longitudinal correlation radius as the distance to the first zero

$$\Delta r_{||} = 2\frac{\lambda}{NA^2} \propto \frac{\Delta r_\perp^2}{\lambda} \tag{4.14}$$

This size corresponds to the Rayleigh distance for the diffraction by a "hole" of size $\Delta r_\perp$.[2] This is the quantative derivation of the intuitive picture given in the previous section.

4.1.4.4 The power spectral density

According to the Wiener-Khintchine theorem, the power spectral density (PSD) is the Fourier transform of the connected intensity correlation function (4.8).

$$C_{\delta I}(\mathbf{k}) = \int d\delta\mathbf{r}\Gamma_{\delta I}(\delta r)e^{i\mathbf{k}\cdot\mathbf{r}} \tag{4.15}$$

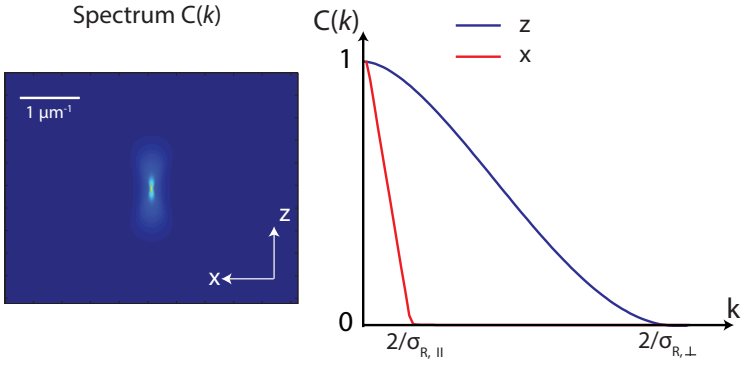

Figure 4.3: **The power spectral density of a speckle**. a) The complete PSD for a numerical aperture $NA = 0.5$ and a wavelength $\lambda = 532$ nm. b) Cuts of the PSD in transverse (z) and longitudinal direction (x).

We want to note here that the transverse PSD is simply given by the autocorrelation of the intensity on the diffuser. We represented the PSD of a circular diffuser in Fig. 4.3. In particular, we can see that the PSD is strictly zero for the spatial frequencies

$$k_{max,\perp} = \frac{4\pi NA}{\lambda} \text{ and } k_{max,||} = \frac{\pi NA^2}{\lambda} \tag{4.16}$$

These cutoff frequencies will serve us as definition of the size of the grain $\sigma_R = 2/k_{Max}$:

$$\sigma_{R,\perp} = \frac{\lambda}{2\pi NA} \text{ and } \sigma_{R,||} = \frac{2\lambda}{\pi NA^2} \tag{4.17}$$

4.2 Realization of a three-dimensional speckle disorder

Comparing the transverse and the longitudinal length of the grains, we recognize instantly that the grains are strongly anisotropic for realistic NA which are compatible with experiments on ultracold atoms. We can evaluate this anisotropy conviniently by the ratio $\kappa = \sigma_{R,||}/\sigma_{R,\perp} = 4/NA$. In typical experiments with low NA this ratio can be as big as 100.

Therefore, we had to take special care in the experiment in order to limit this anisotropy. Working at high $NA \simeq 0.5$, allows us to obtain an anisotropy ratio of $\kappa \sim 8$.

[2] We can recover Eq. (4.14) easily by considering that the typical diffraction angle is $\theta \approx \lambda/\Delta r_\perp$. It is sufficient to write that the spread due to the diffraction $\Delta r_{||}\theta$ is equal to the initial size $\Delta r_\perp$.

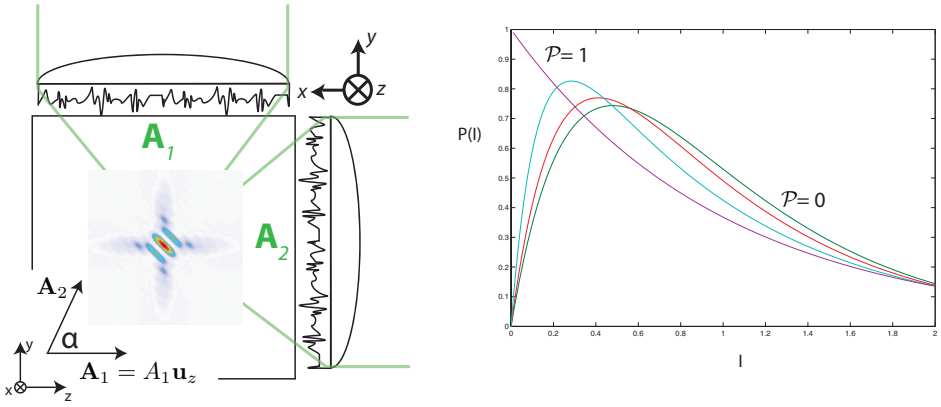

Figure 4.4: **The speckle field superposition**. a) We use aspherical lenses with a maximum $NA \sim 0.5$ to focalise two speckle fields. The two speckle fields are propagating on perpendicular optical axes. They sum up coherently at the center of the science chamber as their polarization is fixed in the z-direction. b) The intensity distribution of the total speckle fields.

Further, on the experiment we can superpose two perpendicular speckle fields to create our disordered potential (Fig. 4.4 a). The upper field has a fixed polarization $\mathbf{A}_1 = A_1\mathbf{u}_z$ and the bottom field has a polarisation $\mathbf{A}_2 = A_2\left(\cos(\alpha)\mathbf{u}_z + \sin(\alpha)\mathbf{u}_y\right)$. As the two fields come from the same laser source, we sum the amplitudes and the total intensity is given by

$$I = |\mathbf{A}_1 + \mathbf{A}_2|^2 = |A_1|^2 + |A_2|^2 + \mathcal{P}\left(A_1^* A_2 + A_1 A_2^*\right) \ , \tag{4.18}$$

where $\mathcal{P} = \cos(\alpha)$. When the two speckle fields are polarized in the same direction , they interfere and $\mathcal{P} = 1$. In this situation the arguments from section 4.1.2 still hold and the speckle field can be seen as a diffraction picture from a large number of elementary diffusers.

If on the other hand the polarizations of the two fields are perpendicular $\mathcal{P} = 0$, the two field do not interfere and we have to do the incoherent sum of their intensities.

We will now characterize the intensity distribution and the correlation functions of this three-dimensional disorder.

4.2.1 Intensity distribution

The total intensity distribution of the superposed field is given by [Goodman 07]

$$P(I) = \frac{1}{\mathcal{P}\bar{I}}\left(\exp\left(-\frac{2}{1+\mathcal{P}}\frac{I}{\bar{I}}\right) - \exp\left(-\frac{2}{1-\mathcal{P}}\frac{I}{\bar{I}}\right)\right) \tag{4.19}$$

We plotted this probability law for different polarizations in Fig. 4.4 b). For the coherent superposition ($\mathcal{P} = 1$) nothing has changed for the way the amplitudes are summed and the intensity distribution is still given by the Rayleigh law (4.5) and the most probable intensity is $I = 0$. As we reduce $\mathcal{P}$, we decrease the interference between the two speckle fields and the two fields become gradually more independent. To some degree, we can

picture each field as some background for the other field, the low intensities are inhibited and the most probable intensity will be shifted to a higher value. In the extreme case of an incoherent sum ($\mathcal{P} = 0$) the probability distribution is changed to

$$P_{\mathcal{P}=0}(I) = \frac{4I}{\bar{I}^2} \exp(-\frac{2I}{\bar{I}}) \ . \tag{4.20}$$

The zero intensities are now forbiddden and the most probable intensity is shifted up to $0.5\bar{I}$. [3]. As expected, the total mean value of the field does not depend on the interference between the superposed fields

$$\langle I \rangle = \int dI \ I \ P(I) = \bar{I} \tag{4.21}$$

The second moment, related to the fluctuations of the intensity, on the other hand is modified

$$\langle I^2 \rangle = \frac{\bar{I}}{2}(3 + \mathcal{P}^2) \tag{4.22}$$

Using the mean value and the second moment, we can calculate the rms of the superposed speckle field

$$\sigma_I = \sqrt{\langle I^2 \rangle - \langle I \rangle^2} \tag{4.23}$$

$$= \bar{I}\sqrt{\frac{1 + \mathcal{P}^2}{2}} \ . \tag{4.24}$$

In the case of $\mathcal{P} = 1$ we rederived the statement that rms is as big as the mean value $\sigma_I = \bar{I}$. In the incoherent superposition $\mathcal{P} = 0$, the interferences between the two fields are suppressed and the fluctuations got reduced to $\sigma_I = \bar{I}/\sqrt{2}$.

4.2.2 Correlation function

The correlation function of the incoherent superposition, $\mathcal{P} = 0$ is the sum of the intensity correlation functions of each single speckle field as represented in the first row in Fig. 4.5. In the x and z directions exists a double structure in the spectrum, associated to the transverse and longitudinal cutoff frequencies of a single speckle.

In the coherent superposition, $\mathcal{P} = 1$, the interference between the two perpendicular speckle fields modulate the grains at a frequency of $\sqrt{2}/\lambda$. This creates a lateral band in the diagonal direction (Fig. 4.5 second column) and increases the frequency cut-off to a value which is close to the maximum value of $\lambda/2$ and correspond to the interference between the most elongated rays at $\theta \sim 160°$. The cutoff frequency is minimal in the diagonal and corresponds to the projection of the diffraction limit on this axis $\sqrt{2}NA/\lambda$. The ratio between the most elongated and the shortest axis of the grains is $\kappa = \sqrt{2}/NA \sim 2.8$ for our experimental parameters. The superposition of the two speckle fields has allowed us to reduce the anisotropy of our disordered potential considerably. A 3D Gaussian fit of the central peak of the autocorrelation function yields standard radii of 0.11 μm, 0.27 μm and 0.08 μm, along the main axes (axis y and the two bisecting lines of x-z).

[3] This modification of the probability distribution will have dramatic effects on the percolation threshold, which we will discuss in Sec. 5.4.7.

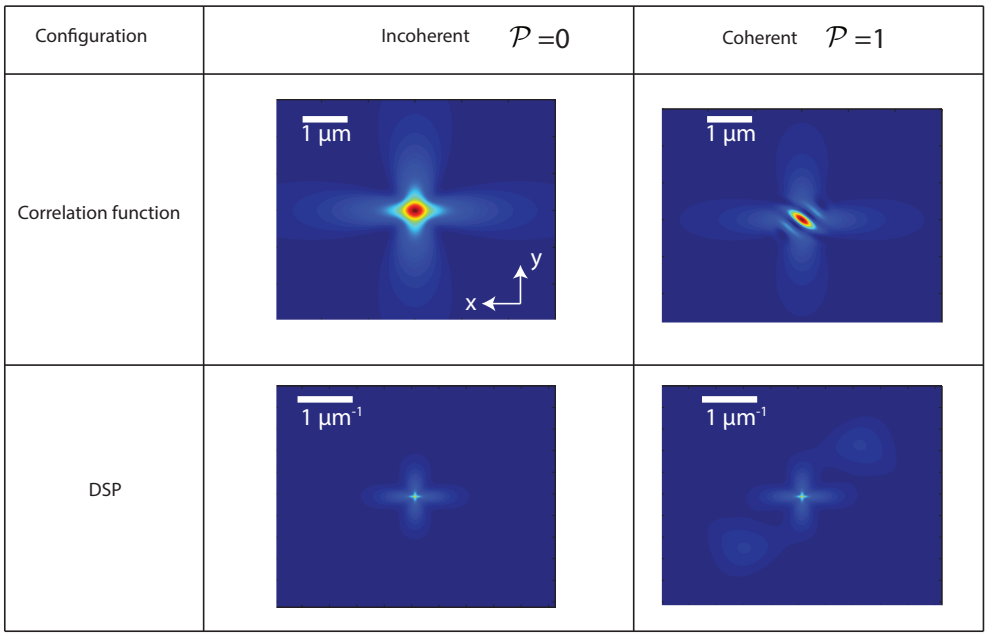

Figure 4.5: **Overview over the correlation functions**. We plot the correlation functions for the superposed speckle in the two limiting cases.

4.2.3 Experimental setup

The setup for the creation of the disordered potential is shown in Fig. 4.4.

The light source is a continous *Coherent* Laser delivering $18W$ with a wavelength $\lambda = 532$ nm. The power on the atoms is controlled by passing the beam through an AOM with an efficiency of $\sim 80\%$. The beam is enlarged by a first telescope and coherently split by a beam spliter. Each of the arms is then further enlarged to a final waist of $w_0 = 12$ mm and finally directed on the atoms through the holographic diffuser with a diameter of 20 mm. This optical setup allows us to apply a maximum power of $\sim 12W$ on the atoms.

The light is subsequently focused on the atoms with an aspherical lens with focal distance $f = 20mm$ and a diameter of ~ 20 mm, allowing the two configurations described previously. A half-wave plate is placed behind the beam splitter in order to turn the polarization of the bottom arm. This way we can tune the polarization in order to realize a coherent or incoherent superposition of the speckle fields. We are able to control the angle between the polarizations with an accuracy of $\pm 5°$. We also tested the stability of the superposition between the two arms before we installed the disorder setup on the experiment. We built up the ensemble of the magnetic levitation and the disorder in a test environment. Having removed the last lens and the diffuser in each of the arms, we observed the interference between the two arms under realistic conditions. The phase drift between the two arms was $\leq \pi/10$ in $10s$ with the magnetic coils being switched on and off during the test.

Finally, a plastic diffuser with an diffraction angle of $5°$ was placed behind the asperical lens. The resulting speckle field has an intensity envelope with a waist of 1.5 mm on the

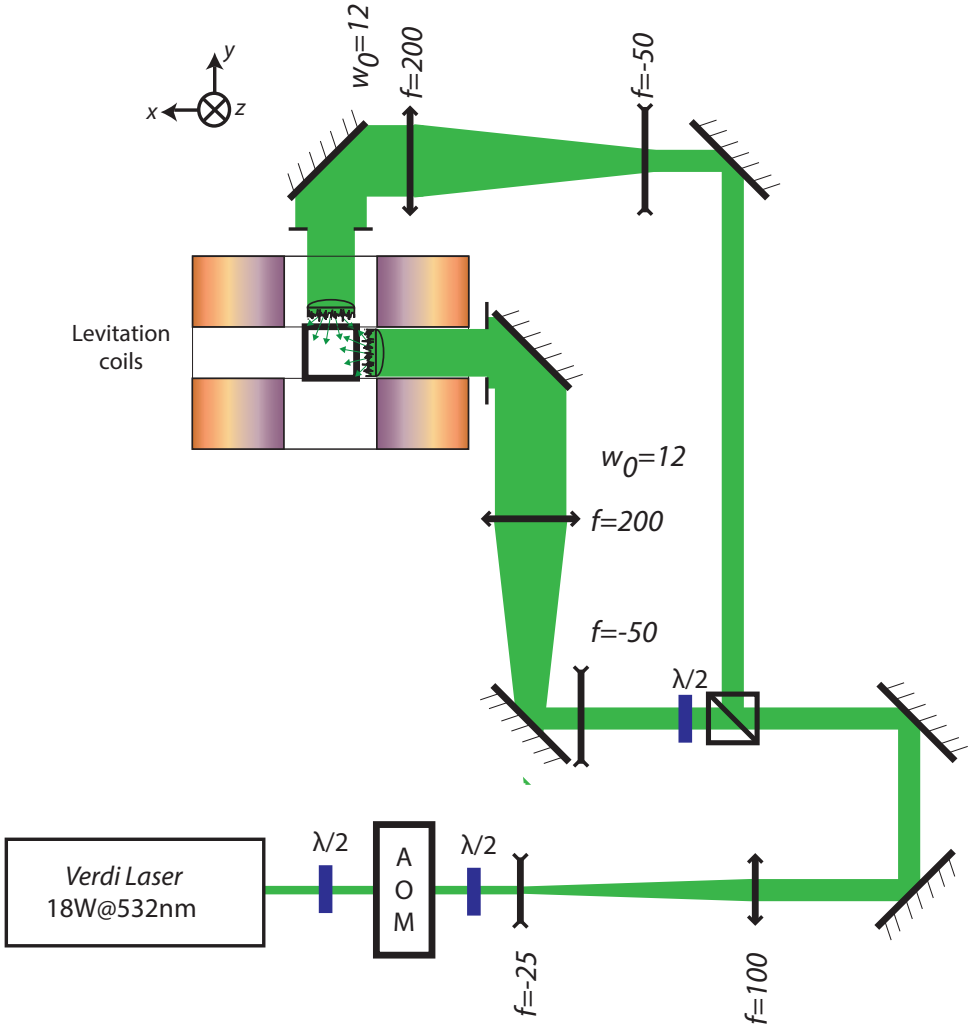

Figure 4.6: **Experimental setup for the generation of the speckle**.

atoms. With this choice we can obtain speckle field intensities up to $\sim 2.6W/\text{ mm}^2$, which corresponds to a maximum disorder strength of $V_R \leq 4.5$ kHz

4.3 Conclusion

In this chapter, we have described the realization of a correlated optical disorder. The potential experienced by the atoms is anisotropic and its correlation lengths are fixed by the numerical aperture of the system and the wave length of the laser.

Using a coherent superposition of two orthogonal speckle fields we reduced this anisotropy considerably and the correlation lengths in the three directions are 0.11 μm, 0.27 μm and 0.08 μm, along the main axes (axis y and the two bisecting lines of x-z). The amplitude

of the disorder is easily modified by changing the intensity of the laser and can reach a maximum value of ~ 4.5 kHz.

Knowing the correlation function and the amplitude of the disorder it is possible to calculate without free parameters the microscopic quantities of the propagation of the atoms in the disorder. This unmatched control of the applied potential allows us to compare our experimental results to analytical theoretical predictions [Piraud 12a, Piraud 12b].

CHAPTER 5

Some notions of diffusion and localization of matter waves

Quantum interferences play a fundamental role for the properties of disordered systems interferences as they can eventually lead to Anderson Localization (AL). In this chapter we are going to discuss the different physical macroscopic and microscopic quantities describing the properties of these systems.

In the first part of this chapter we provide some important concepts in the context of AL, which highlight the importance of interferences and dimensionality. In the second part we discuss the influence of several microscopic parameters in some detail.

We want to add here one word of caution. Whenever possible, we tried to use simple physical explanations of the different quantities presented in this chapter. Most of them give qualitatively correct results, but do not permit to do quantitive predictions. Often such a theoretical prediction would go far beyond the scope of this chapter, as most of the interesting quantities are still subject to an intense research activity at the moment we are writing this manuscript.

5.1 From diffusion in a weak disorder...

We study the propagation of an atom from an initial point $\mathbf{r}_1$ to the final point $\mathbf{r}_2$ in the disorder. The amplitude of such a propagation is the sum of all possible trajectories described by the complex amplitude a_j [1]

$$f(\mathbf{r}_1, \mathbf{r}_2) = \sum_j a_j(\mathbf{r}_1, \mathbf{r}_2) \tag{5.1}$$

The probability of propagation from one point to another is then

$$P(\mathbf{r}_1, \mathbf{r}_2) = \overline{|f(\mathbf{r}_1, \mathbf{r}_2)|^2} \tag{5.2}$$

$$= \overline{\sum_j |a_j(\mathbf{r}_1, \mathbf{r}_2)|^2} + \overline{\sum_{i,j} a_i^*(\mathbf{r}_1, \mathbf{r}_2) a_j(\mathbf{r}_1, \mathbf{r}_2)} \tag{5.3}$$

The $\overline{\ldots}$ marks an ensemble average over different configurations in the disorder as in Ch. 2. In the first term the relative phase between the amplitudes vanishes. This describes the classical probability to propagate from $\mathbf{r}_1$ to $\mathbf{r}_2$. The second term is the product of two different propagation paths and it vanishes over the ensemble average for most configurations of a_i and a_j^*. Nonetheless, we will show later on that this term is associated with quantum interferences between different propagating paths and absolutely essential to understand the dynamics in a strong disorder.

[1] See also the very similar discussion in Sec. 2.2

In a first step, we focus on the weak disorder case where we may neglect the second term and focus on the first contribution in (5.3)

$$P_{Cl}(\mathbf{r}_1, \mathbf{r}_2) = \overline{\sum_j |a_j(\mathbf{r}_1, \mathbf{r}_2)|^2} \tag{5.4}$$

This leads to the well-known problem of diffusion through a disordered medium.

5.1.1 Diffusion as a random walk in a disordered potential

Due to the scattering of the atoms on the impurities the motion of the atoms is modified on a typical length scale l_B, called *transport length*, [2] as shown in Fig. 5.1.

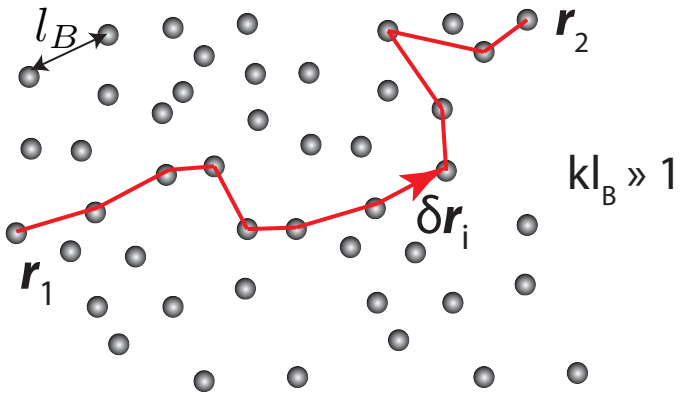

Figure 5.1: **Propagation of a classical particle in a disorder**.

As long as the de Broglie wavelength λ_{dB} is much smaller then l_B, we can describe this propagation as a sequence of successive elastic collisions of the atom with the diffuser, i.e.

$$\mathbf{r}_2 = \sum_{i=1}^{N} \delta\mathbf{r}_i \text{ for } kl_B \gg 1 \tag{5.5}$$

At each elastic collision the particle scatters in a certain direction with some probability $p(\delta\mathbf{r}_i)$. After a large number of scattering events we can apply the central limit theorem and the variance is of the form $\langle \mathbf{r}^2 \rangle = N\langle \delta\mathbf{r}_i^2 \rangle$. The typical time between two scattering events is τ_B and we will define the l_B via $\langle \delta\mathbf{r}_i^2 \rangle = 2l_B^2/d$, [3] where d is the dimension. This means that the probability to find a particle at a distance r from the starting point after a time $t = N\tau_B$ is given by [Kuhn 07]

$$\langle r^2 \rangle = 2Dt \ , \tag{5.6}$$

where we have used $l_B = v\tau_B$. This law is fulfilled in a very wide variety of physical problems like the mixing of two fluids, the propagation of heat, the dynamics of polymers and the propagation of electrons in a crystal. All these systems have the common property

[2] The exact value of l_B will then depend on the microscopic details of the disorder as discussed in more detail in Sec. 5.4.3.

[3] We use this definition to be compatible with the common literature

that the variance of the displacement is linear in time and not quadratic in time like for ballistic motion. This diffusive motion is characterized by the *diffusion constant*

$$D = \frac{v l_B}{d} = D_0 \cdot k l_B, \tag{5.7}$$

where $D_0 = \hbar/md$ is the natural unit of the diffusion constant.

From eq. (5.7) we can see that the diffusion constant directly quantifies the disorder strength kl_B. If the disorder parameter kl_B is very big the disorder is relatively weak and the particle can propagate rapidly through the disorder. While we decrease kl_B the disorder has stronger effects on the propagation and the diffusion slows down.

In the limit of a stronger disorder we are obliged to take into account the contribution of the trajectories that we ignored up to now. In first order they lead to the phenomena of weak localization, i.e. act against the propagation through the disorder. Ultimately they lead to the complete suppression of transport, i.e. Anderon Localization.

5.2 ...to localization in a strong disorder

5.2.1 Weak localization

In the discussion of the propagation through the disorder we have neglected until now the contribution of trajectory pairs of the form

$$P_{CP}(\mathbf{r}_1, \mathbf{r}_2) = \overline{\sum_{i,j} a_i^*(\mathbf{r}_1, \mathbf{r}_2) a_j(\mathbf{r}_1, \mathbf{r}_2)} \ . \tag{5.8}$$

They are a product of distinct propagation amplitudes. Such products often vanish over the disorder average, as there exists typically a certain dephasing between the distinct paths.

Still, some pairs of distinct trajectories remain, as long as their dephasing is small. This is for example the case for two trajectories that follow the same sequence of scattering events and cross, forming a loop with counter-propagating trajectories (Fig. 5.2).

The probability that such a crossing appears in a time interval dt is proportional to the ratio of the explored volume by the particle to the size of the system [Akkermans 07, Müller 09]

$$dp_x(t) = \frac{\lambda_{dB}^{d-1} v \ dt}{L^d} \approx \frac{1}{g} \frac{dt}{\tau_D} \tag{5.9}$$

$$\text{with } g(L) = 2 \frac{k l_B}{d} (kL)^{d-2} \tag{5.10}$$

$$\tau_D = L^2/D_0 \ , \tag{5.11}$$

where we have introduced the *Thouless time* τ_D and the *dimensionless conductance* $g(L)$. This dimensionless conductance is directly related to the conductance $G = I/U$ known from condensed-matter.[4] τ_D is the typical time a particle needs to diffuse through a system of size L^d and sets the upper limit for the time scales of the diffusion. To evaluate the

[4] For electrons both are related by $g = G/(e^2/h)$, where e is the electric charge.

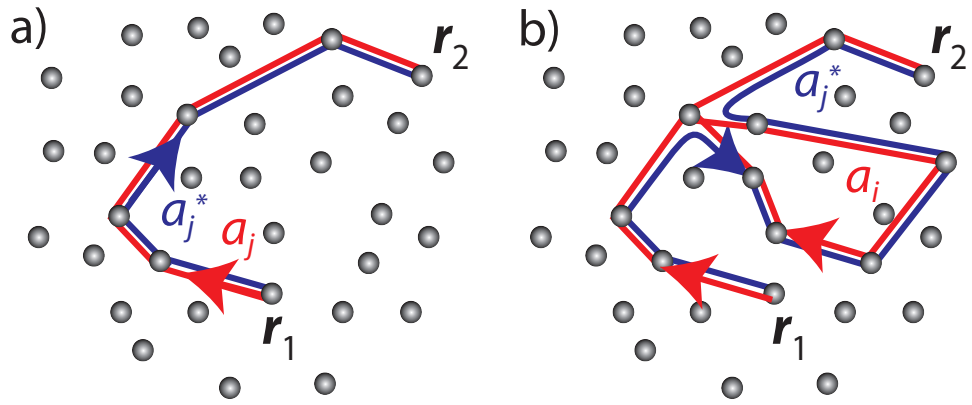

Figure 5.2: **Trajectories contributing to the transport in a disorder**.a) The product of the same amplitude. These pairs of trajectories provide the classical probability of propagation. b) The crossing of the trajectories leads to a new pairing of amplitudes that has to be taken into account even after an ensemble average. As these amplitudes increases the weight of those long paths, such closed loop trajectories are at the origin of the weak localization effect.

total probability for a crossing, we need to integrate the elementary probability (5.9) over time

$$p_x = \int_0^{\tau_D} dp_x(t) = \frac{d}{2kl_B}\frac{1}{(kL)^{d-2}} \tag{5.12}$$

$$= \frac{1}{g} \tag{5.13}$$

If the disorder gets stronger, i.e. kl_B smaller, the probability of a crossing increases as the diffusion slows down and the particle spends more time in the given volume. Further, the probability of a crossing also depends on the size L of the system. We will discuss this very important dependance in some detail below.

Interestingly the interferences increase the weight of the paths with closed loops and counteract the propagation through the disorder, they favor localization [Strinati 89, Di Castro 03]. This phenomena of immense importance for solid state physics is called the *weak localization*, as we have discussed already in the introduction. We will discuss this weak localization further in context of the observation of coherent backscattering of ultracold atoms in Ch. 7.

The weak localization is a first term of a whole series of corrections that have to be taken into account as the disorder gets stronger and it is therefore only valid in the weak disorder limit where $kl_B \gg 1$. We will now extend our discussion to the strong disorder limit $kl_B \leq 1$.

5.2.2 The Thouless criterion

A possibility to connect the physics in the weak and strong disorder limit is to use the dimensionless conductance $g(L)$ as proposed by Thouless in 1977 [Thouless 77]. He showed

that the different values of g can be associated with very different regimes. For $g > 1$ the propagation is diffusive and for $g < 1$ the states are localized.

In order to analyze the physical meaning g we can rewrite Eq. (5.10) in terms of energies

$$g = \rho(E) L^d \frac{\hbar D}{4L^2} \tag{5.14}$$

$$= \frac{J_T}{\Delta} , \tag{5.15}$$

where $\rho(E)$ is the density of states and $\Delta = 1/\rho(E)L^d$ is the spacing between energy levels. $J_T = \hbar D_0/4L^2$ is the *Thouless energy*, which can interpreted as a coupling term as shown in Fig. 5.3.

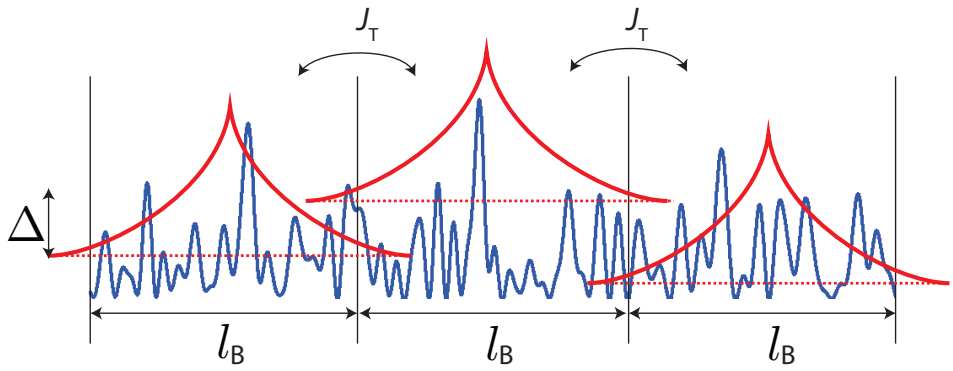

Figure 5.3: **Interpretation of the dimensionless conductance $g = \frac{J_T}{\Delta}$ in the Thouless picture**. The smallest length scale of the propagation in the disorder is the transport length l_B. The different states separeted by the typical length scale are marked by the red lines. They have a typical energy difference of Δ and a typical coupling strength of J_T

In this form g describes the interplay between two typical energy scales of the problem. This energy spacing between different states acts against the propagation of the atoms from one state to another . It therefore favors localization. As the energy spacing Δ is due to the disordered potential, its effect increases for growing disorder strength. J_T on the other hand couples the different states and makes it possible for the particle to propagate from one state in the system to another. It therefore favors therefore the diffusive propagation through the system. This coupling is proportional to the diffusion constant and therefore large in the weak disorder.

Depending on the ratio between these two energy scales, two very different regimes are then possible:

- If $g > 1$, the coupling is stronger than the distance between the different energy levels. In this case, it was argued by Thouless, that the different states mix and the resulting state is delocalized over the total system. This is the diffusive regime, where the (dimensionless) conductivity has to ohmic form

$$g \propto L^{2-d} \tag{5.16}$$

This regime that also called the *ordered* or *conducting phase* in the condensed matter literature.

- If $g < 1$, the coupling is weaker than the energy splitting. The coupling is exponentially small between distinct states and Thouless argued that the whole system is *localized*. In such a localized system, the (dimensionless) conductivity should decreased exponentially with the size of the system

$$g \propto e^{-L/\xi} \ , \tag{5.17}$$

where ξ is the localization length. In condensed matter literature this is also called the *disordered phase* or *insulator phase*.

- For $g \sim g_c \approx 1$ the distance between the energy levels and the coupling balance out. In this case the system does neither behave like in the ordered phase nor the disordered phase. The properties of states in this interesting region depend strongly on the dimensionality as we will see in the following section.

This result rephrases in different terms that the atoms are localized in a strong disorder $kl_B \leq 1$ and diffusive in a weak disorder $kl_B \gg 1$.

Having now in g a quantity that distinguishes between localized and diffusive states, it is important to come back to the explicit dependance of the dimensionless conductance on the system size L. Consider the weak disorder case $g(L) \propto L^{d-2}$. Depending on the dimensionality, $g(L)$ evolves very differently for an increasing size. In 1D, $g(L)$ always goes to values smaller then 1 for very large systems and thus all states are localized in infinite one-dimensional systems. In 2D, there is no explicit dependance on the length. Finally the dependance is inversed in 3D. The weak disorder $g(L)$ increases for a growing system size L, which is in dramatic contrast to the prediction at 1D.

A systematic study of this size dependance $g(L)$ for the different dimensions has been done in the celebrated scaling theory of localization by the "gang of four" consisting of Abrahams, Anderson ,Licciardello and Ramakrishnan, in 1979 [Abrahams 79] and it was reviewed in great detail by Lee et al. [Lee 85]. This scaling theory shows that all states are localized in 1D or 2D and that there exists a phase transition at 3D between diffusive and localized states.

5.3 Scaling theory

The fascinating prediction of Eq. (5.10) is that the speed of the propagation through the disorder, i.e. g, depends on the explored volume L^d. For a particular disorder $g(L)$ evolves smoothly as L increases to very large system sizes and goes over to the limiting case of a diffusive regime (5.16) or the localized regime (5.17). This limiting behavior depends on the microscopic details of the disorder and the dimension.

The scaling theory aims to describe how $g(L)$ changes then for $L \gg l_B$ for all dimensions. Abrahams et al. argued that such a change should be studied by the following scaling function

$$\beta(L) = \frac{d \log g}{d \log L} \tag{5.18}$$

For a normal conductor, $g \gg 1$, one might neglect most quantum corrections and use (5.16) to estimate the behavior of the scaling function [Lee 85]

$$\beta(g) = d - 2 - \frac{c_d}{g} + \mathcal{O}(g^{-2}) \text{ for } g \gg 1 \tag{5.19}$$

The term $d-2$ is the classical contribution from (5.10). The contribution c_d/g is the weak localization and the constant c_d has to be calculated from some microscopic theory.

In the localized regime on the other hand, one should rather use (5.17), which leads to [Lee 85]

$$\beta(g) = \log(g/g_0) \text{ for } g \ll 1 \ , \tag{5.20}$$

where $g0$ is some constant, whose value is of no importance for the following. In this regime $\beta(g)$ is always negative and does not depend on the dimension.

The scaling curve can then be reconstructed using eq. (5.19) for large g, eq. (5.20) for small g and assuming that $\beta(g)$ is monotonic and continuous. We sketched the resulting scaling curves for $d = 1, 2, 3$ in Fig. 5.4 as a function of g.

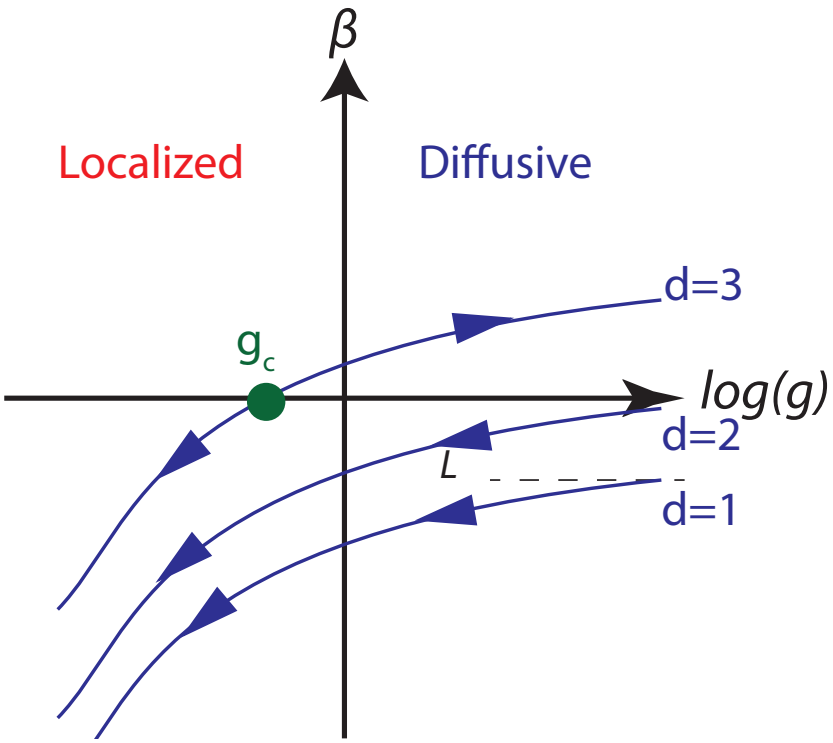

Figure 5.4: **The scaling of the dimensionless conductance** g.

5.3.1 Consequences of scaling theory - Localization of all states in one and two dimensions

In 1D and 2D the scaling function β is always negative. So independently of the initial conductance, the system ends up in an insulating state for an infinite system in one and two dimensions. It seems helpful to understand what the predictions of the scaling theory

mean for the expansion of atoms in a disorder. Suppose that the particles were released in a small region in the disorder that is sufficiently weak to have $g(l) \gg 1$. As the atoms expand they explore an increasing volume and g decreases according to (5.19). At some point $g < 1$ and the atoms don't move anymore. They are localized in a arbitrarily weak disorder.

The case of $d = 2$ is special as β does not depend explicitly on the size of the system. The scaling equation in a weak disorder reads

$$\beta = -\frac{c_2}{g} \text{ for } g \gg 1 \tag{5.21}$$

The conductance does not depend explicitly on the size of the system anymore and the change of the conductance is explicitly due to the weak localization correction encountered in the previous section. As this correction acts against the propagation through the disorder, the constant c has to be positive and all the states are localized. An interesting situation arises, when we add a spin-orbit coupling to the problem [Akkermans 07]. This can actually lead to weak anti-localization, where the return probability is smaller then the classical value. The sign of the constant is then changed [Hikami 80] and a phase transition between localized and diffusive states arises even in two dimensions [Evers 08, Fendley 00]. A study of this transition with ultracold atoms would be fascinating and might be feasible with modern experimental techniques [Lin 09, Lin 11].

5.3.2 The existence of a mobility edge in 3D

The situation changes radically for three dimensions. The dimensionless conductance (5.10) reads

$$g_{3D} = \frac{2kl_B}{d} kL \text{ for } g \gg 1 \tag{5.22}$$

The scaling relations take for $d = 3$ the form:

$$\beta = 1 - \frac{c_3}{g} > 0 \text{ for } g \gg 1 \tag{5.23}$$

$$\beta = \log(g/g_0) < 0 \text{ for } g \ll 1 \tag{5.24}$$

β is positive for large g and negative for small g and must therefore cross zero at some value that we note g_c. Again, we might consider the expansion of atoms in the disorder to gain some insight. If the disorder is weak, i.e. $g(l) > g_c$, $\beta(g)$ is always positive and the conductance increases as the explored volume becomes bigger, so the atoms continue to diffuse through the disorder for all times. A different scenario arises, when the initial disorder is strong, $g(l) < g_c$. As the $\beta(g)$ function is now negative, the atoms stay localized and the propagation comes to a halt at some time τ_{Loc}.

Hence, there exists a transition, called *Anderson transition*, between a localized and a diffusive phase in three dimensions. The localized phase exists in a strong disorder ($g(l) < g_c$) for which the dynamics will stop after some time τ_{Loc}. A diffusive phase for which the dynamics will continue for any time can be found in a weak disorder ($g(l) > g_c$).

The transition from the diffusive to the localized phase must happen somewhere in the region of $g_c \sim 1$ and the smallest length scale we can use in our description is l_B, leading us to

$$\Rightarrow (kl_B)_c \sim 1 \tag{5.25}$$

The above equation, called the *Ioffe-Regel criterion*, implies the existence of localized, low energy states with $kl_B < 1$ and diffusive high energy states with $kl_B > 1$. The energy E_C separating the two scales is called the *mobility edge*.[5]

5.3.3 The critical region

For a 3D disordered system we have seen, that there exists a localized and a diffusive phase separated by a mobility edge E_C. The region around this mobility edge, called the *critical region* has some interesting properties. Atoms with energy E just above the mobility edge are diffusive, but the disorder is so strong that the diffusion is extremely slow approaching zero for an energy $E = E_C$. As a function of $E - E_C$ we can describe the diffusion constant in this region as [Lee 85]

$$D \propto |E - E_c|^s \ , \tag{5.26}$$

where s is a *critical exponent*. Atoms with energies just below the mobility edge on the other hand, are localized on very large length scales which diverges for $E = E_C$. Its scaling as function of its distance to mobility edge is:

$$\xi \propto |E - E_c|^{-\nu} \ , \tag{5.27}$$

where ν is a second critical exponent. This region show a peculiar behavior, which leads to unusual properties for such critical states. They are subject to research in the large field of theoretical and experimental investigations of phase transitions [Sachdev 11, Ma 76, Goldenfeld 92].

It is one of the beautiful properties of phase transitions that ν and s do not depend on the microscopic details of the problem. Atoms in a speckle, electrons in a crystal or photons in disordered powders should all follow the same scaling equations Eq. (5.26) and Eq. (5.27). From numerical investigations it is known nowadays that $s = \nu = 1.58 \pm 0.01$ [Lemarié 09, Slevin 99].

It is one of the major motivations of the experiments presented in this thesis to pave the way to investigations of this critical regime with ultracold atoms in a speckle potential.

Another major goal of ongoing experimental and theoretical investigations is the precise investigation of the position of the mobility edge. This position will depend on the microscopic details of each system. Up to this day, several theoretical predictions like the self-consistent theory presented in Sec. 5.4.9 exist, but none allows for exact predictions of the precise position of the mobility edge. Given the complexity of the problem, it is a formable testing-ground for ultracold atoms as a quantum simulator.

5.4 Microscopic quantaties - Energy scales

Up to now, we have discussed the propagation of atoms through the disorder on a macroscopic scale. We will now turn our attention to the microscopic parameters controlling the propagation in a speckle disorder.

[5] The existence of such a mobility edge was already predicted by Neil Mott in 1961 [Mott 61]. He argued that particles with $kl_B < 1$ have a de Broglie wavelength that is bigger then the mean free path. They are always in collision with the disorder and are localized.

5.4.1 The scattering time

During the propagation of the atoms through the disorder, they undergo elastic scattering on the different grains in the speckle disorder. The characteristic distance between the scattering events is called the *mean free path*

$$l_S = v\tau_S \ , \tag{5.28}$$

where τ_S is the *scattering time*. Several generic approaches, like the Green function formalism [Kuhn 07], exist for the calculation of the scattering time. We present here a very simple approach that allows us to calculate τ_S to first order perturbation theory in a weak disorder.

The time scale on which an atom in the initial state $\mathbf{k}_i$ scatters in some other final state $\mathbf{k}_f$ is given by Fermi's Golden rule

$$\frac{1}{\tau_S} = \gamma_{S,k} = \frac{2\pi}{\hbar} \sum_{\mathbf{k}_f} |\langle \mathbf{k}_f | \mathcal{V} | \mathbf{k}_i \rangle|^2 \ \delta(E_{\mathbf{k}_f} - E_{\mathbf{k}_i}) \ , \tag{5.29}$$

where $\langle \mathbf{k}_f | \mathcal{V} | \mathbf{k}_i \rangle$ describes the interaction of the atoms with the impurity potential. We can then identify $|\langle \mathbf{k}_f | \mathcal{V} | \mathbf{k}_i \rangle|^2$ with the Fourier transform of the correlation function of the disorder $C(|\mathbf{k}_f - \mathbf{k}_i|)$

$$\frac{1}{\tau_S} = \frac{mk^{d-2}}{2\pi^{d-1}\hbar^3} \int d\Omega C(2k\sin(\theta/2)) \ , \tag{5.30}$$

where we integrate over the total surface of the unit sphere and θ is the scattering angle between $\mathbf{k}_f$ and $\mathbf{k}_i$ (see Fig. 5.5). The argument of the correlation function

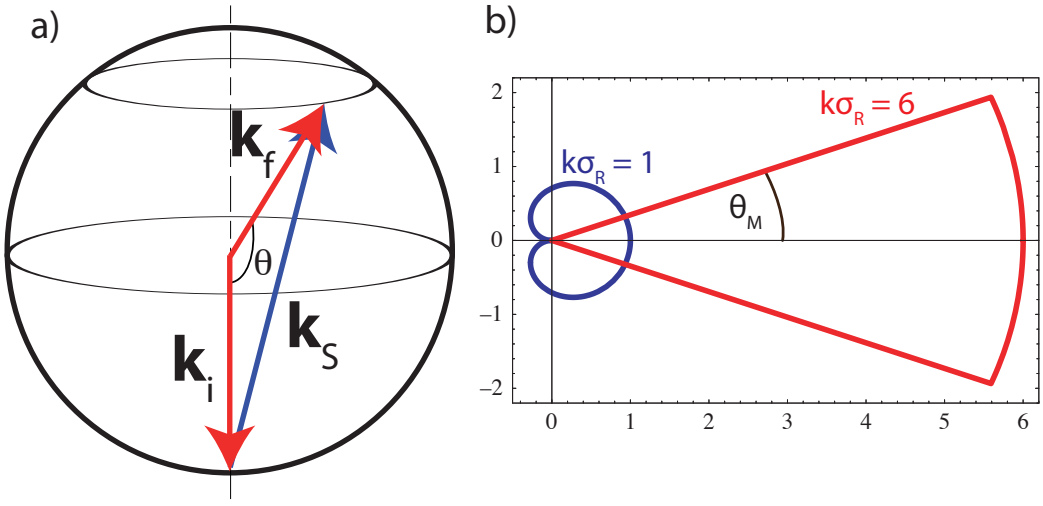

Figure 5.5: **Scattering of the atoms in 3D.** a) Scheme representing the scattering by an angle θ from $\mathbf{k}_i$ to $\mathbf{k}_f$ in 3D. The vector $\mathbf{k}_s$ has a length $k_s = 2k\sin(\theta/2)$ corresponding to a frequency component of the disorder potential. b) Scattering distribution in an isotropic disorder from [Kuhn 07]. For large $k\sigma_R$ the scattering is restrained in a scattering angle $\theta_M < 2/k\sigma_R$.

$k_S = |\mathbf{k}_f - \mathbf{k}_i| = 2k\sin(\theta/2)$, indicates that the Bragg condition has to be verified in the Born approximation, where k_S is the amplitude of the transferred momentum. Kuhn et al. have shown that the scattering time for an isotropic speckle disorder has the analytical form [Kuhn 07]

$$\hbar\gamma_{S,k} = \pi\frac{V_R^2}{E_R}\left(\theta(1-k\sigma_R) + \frac{1}{k\sigma_R}\theta(k\sigma_R - 1)\right) \tag{5.31}$$

$$E_R = \frac{\hbar^2}{m\sigma_R^2}\ , \tag{5.32}$$

where E_R is called the correlation energy[6]. The correlation function of a speckle disorder has a cutoff at $1/\sigma_R$ and hence the transferred momentum is restricted to $k_S \leq 2/\sigma_R$ (see Sec. 4.1.4.4). This leads to the two different diffraction regimes pictured in Fig. 5.5 b). If $k\sigma_R \leq 1$ we are in the limit of short correlations, where the atom can be diffracted in all directions and the de Broglie wavelength is longer than the disorder valleys. Quantum effects like tunneling play a major role in this case.

The opposite case, $k\sigma_R > 1$, describes a smooth disorder, where a classical picture of a particle propagating through the disorder can be a good starting point. The diffraction in this regime is preferentially in the forward direction, because of the Bragg condition $\sin\theta \leq 1/k\sigma_R$ limits the diffraction angle. In this regime, the motion is randomized over longer distances, which leads us to the distinction between mean free path and transport length done in Sec. 5.4.3.

5.4.2 The energy spread and the weak disorder condition

The coupling between the initial state $\mathbf{k}_i$ to a continuum gives rise to an energy uncertainty $\Delta E = \hbar/\tau_S$ of this state as shown in Fig. 5.6. This energy spread is quantified by the *spectral function* $A(k,E) = |\langle\mathbf{k}|E\rangle|^2$. It measures the probability for a state of energy E to have a wave vector $\mathbf{k}$. In a weak disorder the spectral function is a Lorentzien curve of width $\hbar\gamma_{S,k}$ and centered around the kinetic energy of the atoms E_k

$$A(k,E) = \frac{\hbar\gamma_{S,k}}{2\pi}\frac{1}{(E-E_k)^2 + (\hbar\gamma_{S,k}/2)^2} \tag{5.33}$$

The previously presented calculation supposed a weak disorder, where the energy spread is much smaller then the energy of the atoms $\Delta E \ll E_k$. We can rewrite this condition, using Eq. (5.31) and (5.32)

$$\Delta = \frac{V_R^2}{E_k E_R} \ll 1 \tag{5.34}$$

With increasing disorder strength a state k becomes distributed over a large energy region. In a very strong disorder $\Delta \gg 1$, the width of the distribution completely overwhelms the initial kinetic energy of the atoms. This large energy distribution is an essential ingredient to the understanding of our experiments on localization (and therefore in a strong disorder) that we present in Ch. 6.

[6] It is further discussed in section 5.4.4.

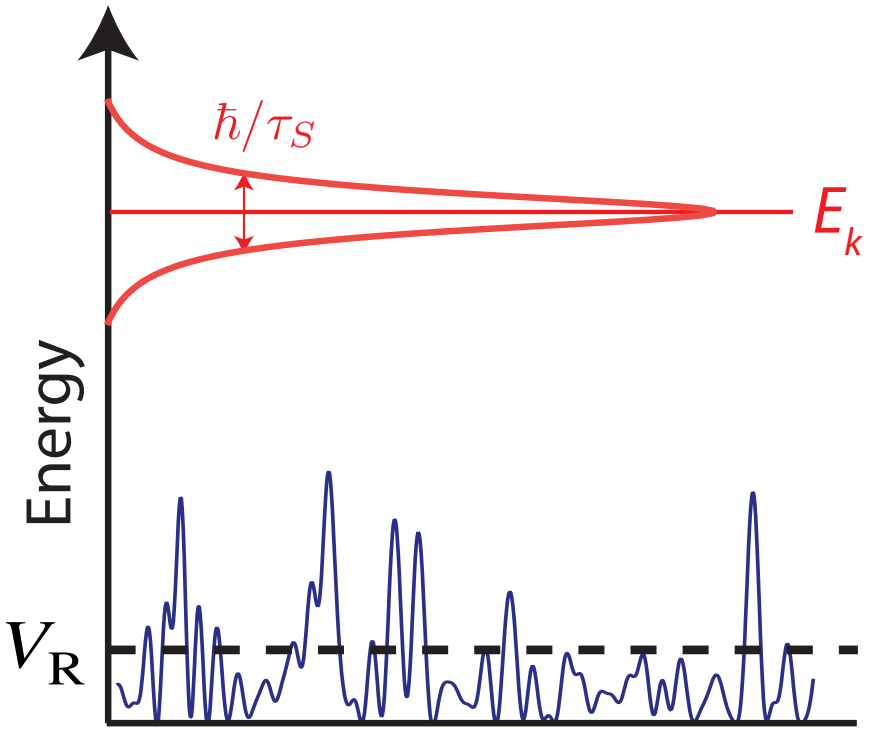

Figure 5.6: **Energy spread in a disorder**.

5.4.3 The transport length

We now come back to the propagation of the atoms through the disorder. We have seen that in a correlated disorder like the speckle the collisions of the atoms with the disorder are not always isotropic as scattering can be restricted in the forward direction. The motion is then randomized over a longer distance than the mean free path. This distance is the transport length l_B, which we had introduced phenomenologically in Sec. 5.1. In an isotropic disorder it can be related to the mean free path by [Kuhn 07]

$$l_B = \frac{l_S}{1 - \langle \cos\theta \rangle} \ , \tag{5.35}$$

where $\langle \dots \rangle$ signifies the average over the different scattering angles. If the scattering probability is uniformaly distributed over all scattering angles, the two length scales are identical. If the scattering angle is strongly restricted in the forward direction the transport length is much larger then the mean free path.

Kuhn et al. [Kuhn 07] were then able to give an analytical expression of l_B

$$1/kl_B \ = \ \frac{\pi}{3}\Delta \left(\theta(1 - k\sigma_R) + (k\sigma_R)^3 \theta(k\sigma_R - 1) \right) \ . \tag{5.36}$$

kl_B is inversely proportional to the disorder parameter $kl_B \propto 1/\Delta$ and measures therefore directly the strength of the disorder. This justifies in a more rigorous way that we can use kl_B as a measure of the disorder strength, as argued at the beginning of this chapter in a much more qualitative way.

5.4.4 The correlation energy - from classical to quantum disorder

In the discussion of the scattering and the transport time we had to introduce the correlation energy

$$E_R = \frac{\hbar^2}{m\sigma_R^2} \ , \tag{5.37}$$

which arises from the finite correlation length σ_R of the speckle disorder. It has the meaning of a zero point energy for an atom confined in spatial region of size σ_R. Depending on the ratio V_R/E_R we can distinguish between two different disorder regimes [Shapiro 12, Shklovskii 08].

If the disorder amplitude is smaller than the correlation energy $V_R < E_R$, a typical valley does not support any bound states and classical trapping does not play any role to understand the physics of the problem. The only possiblibility to localize particles is by quantum interference effects and we call such disorder a *quantum disorder*. In this regime the disorder is smoothed by the long de Broglie wavelength and might be described by an effective disorder $V_R^{Eff} = V_R^2/E_R$ [Economou 83].

If on the other hand the disorder amplitude is much higher than the correlation energy, a typical valley contains a large number of bound states and semi-classical approaches can be helpful to understand the problem. We speak of a *classical disorder*.

We now go on with a discussion of the position of the mobility edge in those two different disorder regimes.

5.4.5 The mobility edge in the quantum disorder regime

The regime, where quantum effects should be most important is the case of a quantum disorder and for a de Broglie wavelength much bigger then the typical size of the valley $k\sigma_R \ll 1$. In this regime, classical trapping is forbidden and quantum effects like tunneling are surely important. As sketched in Fig. 5.7 the mobility edge is therefore well separated from the classical percolation threshold, that is the energy where a classical particle is trapped in an infinite disorder.

Commonly, this regime is called the the *white noise limit*, where we can neglect the extremely small correlation length [Falco 09b]

$$\langle V(\mathbf{r}_1)V(\mathbf{r}_2)\rangle = \kappa^2\delta(\mathbf{r}_1 - \mathbf{r}_2) \text{ with } \kappa^2 = V_R^2\sigma_R^3 \tag{5.38}$$

The disorder is then described by the *Larkin length*

$$\mathcal{L} = \frac{\hbar^4}{m^2\kappa^2} \ . \tag{5.39}$$

As this is the only remaining length scale of the problem, the mobility edge should be in the order of magnitude of the only energy scale describing the disorder the Larkin energy [Falco 09b, Shapiro 12, Shklovskii 08]

$$W = \frac{\hbar^2}{m\mathcal{L}^2} = V_R\left(V_R/E_R\right)^3 \ , \tag{5.40}$$

where W is measured from the average amplitude of the disorder. This dimensional argument allows us to estimate that the mobility edge should be somewhere in the region of V_R as W is only some small correction in the case of $V_R/E_R \ll 1$. The exact scaling, if it is slightly above or below V_R and other important question will then depend on the microscopic details of the disorder.

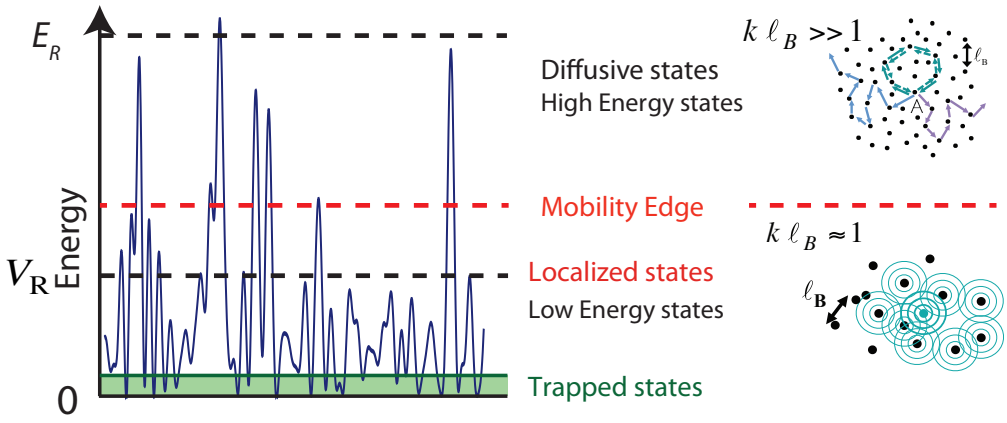

Figure 5.7: **Energy diagram in the quantum disorder:** The high energy states are diffusive as $kl_B \gg 1$. The low energy states with $kl_B \lesssim 1$ are localized. In between them there exists a mobility edge. It marks the energy at which atoms stop to propagate through the disorder.

5.4.6 The mobility edge in the classical disorder regime

In the opposite limit of $V_R \gg E_R$, where a typical valley contains a large number of bound states, the classical picture can be a good starting point to estimate the position of the mobility edge. We can therefore, estimate that Localization will typically arise in the vicinity of the classical percolation threshold E_P as shown in Fig. 5.8 [Shklovskii 08, Shapiro 12]. However, as we approach the mobility edge the motion slows down until $D \leq \hbar/m$. At this point $kl_B \sim 1$ and interference effects localize the particle. This gives us the very rough estimate of

$$E_C \sim E_P \left(1 + \frac{1}{(V_r/E_R)^{2t}}\right) , \tag{5.41}$$

, this correction in the second term becomes very rapidly negligible as the exponent t is rather is, that is $2t \sim 3.4$. It means that interference effects will localize the particle even for energies slightly higher then the percolation threshold.

This relationship has to be used with a lot of caution as it has supposed two important scales: a microscopic scale associated with the diffusion constant D_0. A second macroscopic scale which describes the clustering of the volume in the vicinity of the percolation threshold has to exist. The existence of this second scale is not obvious at all and a very strong assumption. If the valleys become very large and flat, in the extreme case the potential is zero between some peaks, there is no connection between the classical percolation threshold and localization [Shapiro 12].

The position of the mobility edge for an isotropic speckle disorder in this classical regime was studied by quantum Monte-Carlo methods by Pilati et al. [Pilati 10]. They observed the mobility edge to be significantly higher than the classical percolation threshold, suggesting that quantum effects should play a major role. On the other hand, the mobility edge was still scaling with V_R and was located well below the mean value V_R of the speckle, which suggests that a semi-classical interpretation of the localization process might be adapted. Recent results by Piraud et al. using a self-consistent theory of

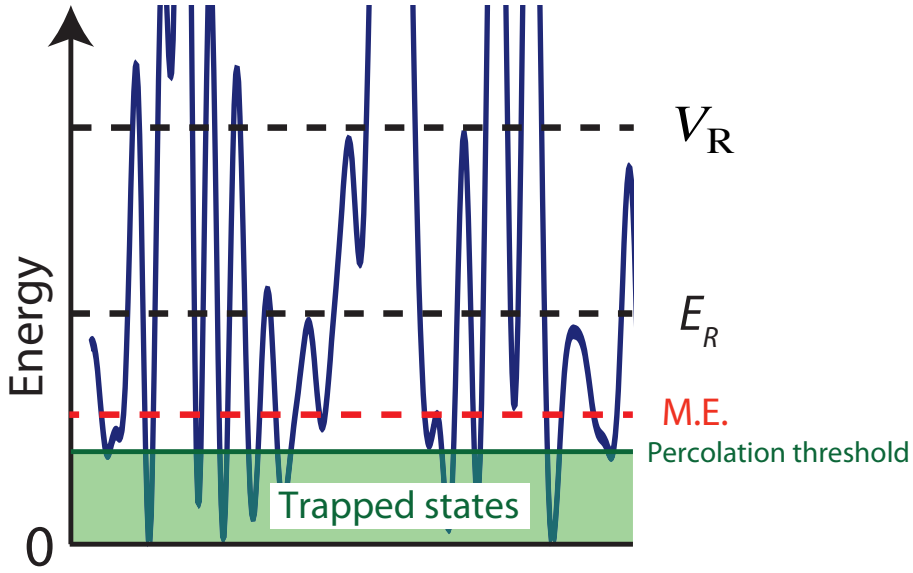

Figure 5.8: **Energy diagram in the classical disorder:** $V_R \gg E_R$ The mobility edge is very close to the classical percolation threshold, leaving only a small energy window where quantum effects are predominant.

localization to calculate the mobility edge seem to hint in a similar direction [Piraud 12b].

5.4.7 The classical percolation threshold

We continue with a discussion of the classical percolation threshold, corresponding to the critical energy below which the atoms are classically trapped.

Classical particles cannot access regions of potential energy higher than their total energy. Hence, these regions are forbidden for an atom moving in a disorder and the atom has to propagate in the remaining accessible volume (Fig. 5.9)

$$\Phi(E) = \frac{1}{L^d} \int_{V(\mathbf{r})<E} d\mathbf{r} \tag{5.42}$$

At the *percolation threshold* E_P this remaining volume is so small that the allowed regions are disconnected and the atom is trapped in one of the disorder minima. It determines the classical mobility edge E_P separating classicaly localized (trapped) states for $E < E_P$ and diffusive ones with $E > E_P$. This is the so called percolation transition and it has been studied intensely [Stauffer 94, Kirkpatrick 73, Isichenko 92]. As in the case of a quantum system, it is a transition between diffusive states and localized (trapped) states. Approaching the percolation threshold the diffusion constant falls to zero

$$D \sim D_0 \left(E/E_P - 1\right)^t \ , \tag{5.43}$$

where $D_0 = \sqrt{V_R \sigma^2/m}$ is the natural unit for classical diffusion and t is the *percolation conductance exponent*. It is $t \sim 1.7$ in 3D [Efros 84, Zallen 71].

The exact position of the percolation threshold E_P in the disorder depends on the dimension of the problem and the microscopic properties of the disorder. At low dimensions

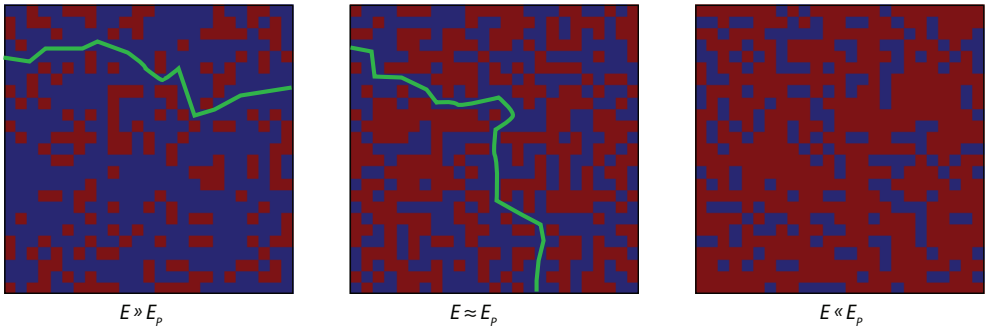

Figure 5.9: **Example of a percolation**. We show the propagation of a particle through a $2d$ lattice, where sites with $V > E$ are not accessible. A particle with $E \ll E_P$ cannot propagate and is trapped in a local minima of the disorder

the trapping in a local minimum is much easier as the atom cannot travel around high peaks.

In 1D the atom is directly trapped between two peaks higher then its energy E. In our speckle disorder, where arbitrarily high potential peaks exist, the percolation threshold is $E_{P,1D} = \infty$. With increasing dimension it becomes easier to travel around those high peaks and the percolation threshold is lowered. For a two-dimensional speckle the percolation is $E_{P,2D} = 0.52 V_R$ [Smith 79, Weinrib 82, Pezzé 11].

For an isotropic three-dimensional speckle disorder it was shown that the percolation threshold is extremely low. The critical energy is there given by [Pilati 10]

$$E_{P,3D} \simeq 4 \cdot 10^{-4} V_R \tag{5.44}$$

This threshold is 2 orders of magnitude lower than in the widely used three-dimensional gaussian disorder-model, where $E_{P,G} = 0.04 V_R$ [Efros 84, Skal 73]. The Rayleigh law distribution of the intensity in speckle, producing a grained structure as discussed in Sec. 4.1.3, makes it very improbable to get trapped in the large regions of low intensity.

5.4.8 Percolation in an anisotropic 3D speckle

In our experiment we do not work with an isotropic speckle disorder, but with a superposition of two perpendicular speckle fields. Depending on the polarization of the two fields $\mathcal{P} = \cos\alpha$, where α is the angle between the polarizations of the superposed speckle fields, the intensity distribution is modified (for a detailed discussion see Sec. 4.2.1).

We studied the percolation for those experimentally relevant configuration numerically, the results are shown in Fig. 5.10. When the two fields are superposed coherently ($\mathcal{P} = 1$) the percolation threshold stays as low as in the isotropic case, as the intensity distribution follows again a Rayleigh law. We numerically found the percolation threshold to be $E_{P,\mathcal{P}=1} \leq 5 \cdot 10^{-3} V_R$. The discrepancy with the results for the isotropic case by Pilati et al. are due to the limited size of the grids we could use for our studies.[7]

[7] We performed simulations on a grid of 300x300x300 $= 27 \cdot 10^6$ elements. Bigger grids would go beyond the scope of our studies as they would have to be performed on much more powerful computers.

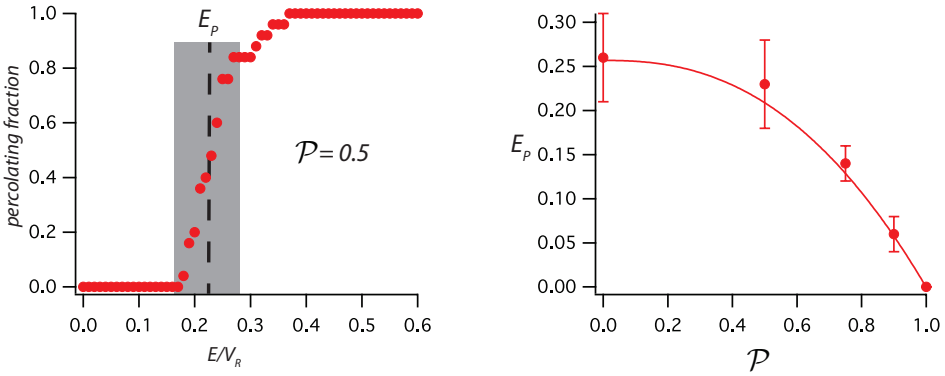

Figure 5.10: **Percolation in a 3D speckle**. a) We measure the fraction of configurations that percolate at an energy E over a cube of size $L = 10\sigma_{R,\perp}$ and a grid step of $1/20\sigma_{R,\perp}$. The plotted data are from an average over 25 configurations. b) The percolation threshold as a function of $\mathcal{P}$. As the low intensity regions get suppressed for incoherent superpositions, the percolation threshold increases. Error bars are estimated from the width of the transition region.

Decreasing the coherence modifies the intensity distribution in the speckle according to Eq. (4.19). The probability to find regions of low intentensity gets strongly suppressed in this case, which leads to a dramatic increase of the percolation threshold to $E_{P,\mathcal{P}=0} = 0.26 \pm 0.05 V_R$.

As we want to study the localization of atoms by quantum effects, it is advantageous to work in the coherent configuration $\mathcal{P} = 1$. The classical percolation threshold is then extremely low and classical trapping can be neglected for the interpretation of our experiments.

5.4.9 The self-consistent theory of localization

We want end this chapter with some words on the self-consistent (SC) theory of localization.

In Sec. 2.2 we have seen that quantum interference effects slow down the propagation of the atoms through the speckle disorder. The diffusion constant of the system is therefore smaller than without the interference

$$D = D_0 - \delta D \ , \tag{5.45}$$

where D_0 is the classical diffusion constant of the system and δD is the reduction of the diffusion constant due to the quantum corrections. The first quantum correction to be taken into account is the weak localization correction, which is proportional to the probability of a crossing. Hence, one assumes [Vollhardt 92]

$$\frac{\delta D}{D_0} \approx p_x \simeq \frac{1}{g} \ . \tag{5.46}$$

From Eq. (5.14) we can see directly the correction of the diffusion constant depends on the diffusion constant itself

$$D = D_0 - D_0 \cdot p_x(D_0) \ . \tag{5.47}$$

A refinement of the above equation would be to evaluate the probability of a crossing for the actual diffusion constant of the system D, leading to

$$D = D_0 - D_0 \cdot p_x(D) \ . \tag{5.48}$$

This is a self-consistent equation for the calculation of the diffusion constant in the framework of weak localization. In this approach the interference effects (weak localization) are a precursor of the complete suppression of transport (strong localization). This *self-consistent theory of Localization*, was developed by Vollhardt and Wölfe to give a quantitative description of localization [Vollhardt 80]. It is to our knowledge the only theory that allows a calculation of the mobility edge based on the microscopic properties of the disorder. The mobility edge which is calculated from the microscopic properties of the disorder, is in qualitative agreement with the Ioffe-Regel criterion, which was based on purely macroscopic considerations. The agreement between the predictions of SC theory and numerical simulations for some kinds of un-correlated disorder can be quite remarkable (see Fig. 5.11). On the other hand, the self-consistent theory is now well known to be not perfectly accurate in the prediction of the mobility edge and there are still no numerical simulations to compare to for a speckle disorder. This theory is furthermore not applicable in the critical region as it predicts universal exponents $s = \nu = 1$ in contradiction with the widely accepted value $s = \nu = 1.57$ [Kramer 93].

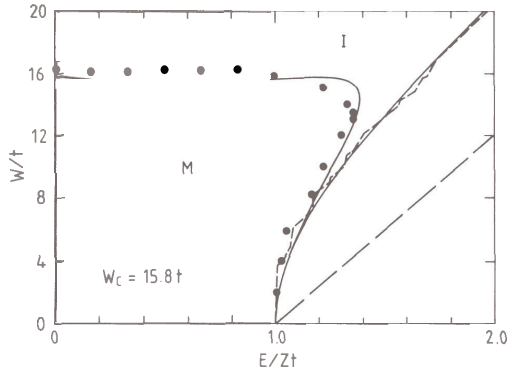

Figure 5.11: **Comparision numerics - SC theory for an uncorrelated disorder** form [Vollhardt 92]. We compare the numerical simulations (black dots) with the predictions of the SC theory (continuous line) for a box-shaped level-distribution.

The self-consistent theory has been applied to the case of an isotropic speckle and predicted that the mobility edge is actually given by

$$(kl_B)_C = \sqrt{\pi/3} \ , \tag{5.49}$$

which is in agreement with the qualitative Ioffe-Regel criterion (5.25). The mobility edge is therefore at

$$E_C = \sqrt{\pi/3}\frac{V_R^2}{E_R} \ , \tag{5.50}$$

where the zero of the energy is taken to be at the mean value of the speckle V_R. For a quantum disorder, we can rewrite the previous equation as $E_C \approx V_R^{eff}$ (see Sec. 5.4.5)

and might say qualitatively that the atoms are localized when the smoothed disorder is as large as the kinetic energy of the atoms. In the classical regime, there are indications that the approximations done in order to obtain equation (5.50) are to rough even for qualitative disscusions and that more sophisticated approaches might be necessary [Yedjour 10, Piraud 12b].

A very detailed discussion of the theory can be found in numerous reviews [Vollhardt 92] and in the context of ultra-cold atoms especially in the PhD of Marie Piraud.

5.5 Summary - a generic phase diagram in 3D

In this chapter we discussed the dynamics of atoms propagating through a disorder. We saw that the disorder strength is characterized by kl. From the scaling theory it followed that in 1D and 2D all states are localized in an infinite disorder and that there exists an phase transition in 3D as sketched in Fig. 5.12.

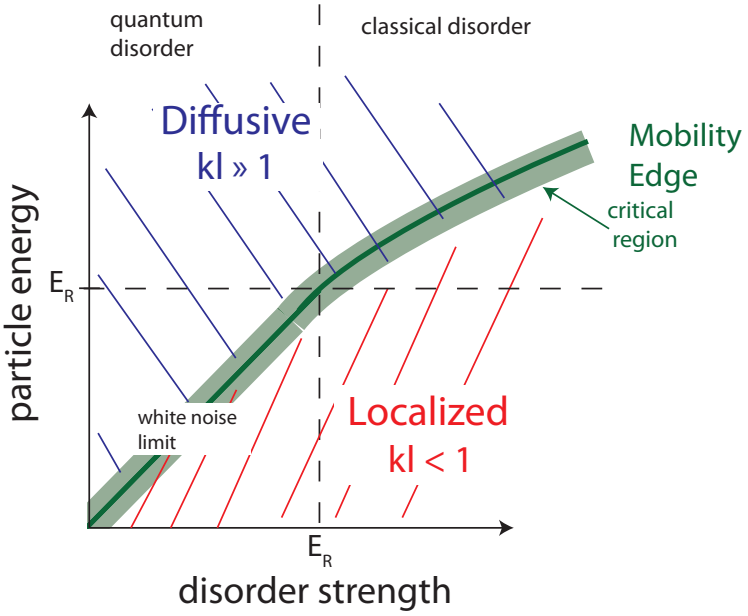

Figure 5.12: **Generic phase diagram at 3D**.

In this 3D case, the diffusive states ($kl \gg 1$) are then separated from the localized states by a mobility edge at $kl \sim 1$. The exact position of the mobility edge depends then on the microscopic properties. In general, on can identify several important regimes depending on the ratios between the particle energy E, the disorder strength V_R and the correlation energy E_R (see Fig. 5.12).

The correlation energy sets a typical upper energy scale, below which quantum effects play an important role in the system. For particle energies below the correlation energy, $E \ll E_R$ the deBroglie wavelength is bigger than the typical size of the valleys and quantum interference effects like tunneling are pronounced. If the amplitude of the disorder is further smaller than the correlation energy, $V_R \ll E_R$, the typical valley does not support any bound states and trapping gets negligible. It is in this white-noise limit, where the

wave character of the atoms is most important that we performed our experiments on AL presented in the next chapter.

CHAPTER 6

Experiments on 3D Localization

Anderson localization (AL) was proposed more than 50 years ago [Anderson 58] to understand how disorder can lead to the total cancellation of electron conduction in certain materials. It is a purely quantum, one-particle effect, which can be interpreted as due to interference between the various amplitudes associated with the scattering paths of a matter wave propagating among impurities. According to the celebrated scaling theory [Abrahams 79] , AL depends on the dimension of the system, and in the three-dimensional (3D) case a mobility edge is predicted. It is an energy threshold separating localized states from diffusive states. However, determining the precise value of the mobility edge, and the corresponding critical behaviour around it, remains a challenge for microscopic theory, numerical simulations, and experiments. The quest for AL has been pursued not only in condensed matter physics [Lee 85] , but also in wave physics [van Tiggelen 99], and experiments have been carried out with light waves [Wiersma 97, Störzer 06, Schwartz 07, Lahini 08], microwaves [Chabanov 00] and acoustic waves [Hu 08]. Nowadays, ultracold atoms have proven to be a great system for the study of AL. Following theoretical proposals [Damski 03, Sanchez-Palencia 07, Kuhn 07, Skipetrov 08], recent experiments have shown that ultracold atoms in optical disorder constitute a remarkable system to study 1D localization [Billy 08, Roati 08] or 2D diffusion [Robert-de Saint-Vincent 10, Pezzé 11] of matter waves.

Here, we report the observation of 3D localization of ultracold atoms of a Bose-Einstein condensate (BEC), suspended against gravity, and released in a 3D optical disordered potential. Our scheme is a generalization of the one that allowed us to demonstrate AL in 1D . Therefore, I start the chapter with a discussion of those 1D experiments. Additionaly to its historical value, it allows to present the important parameters we have to control in such experiments. It is a beautiful textbook example of what such expansion experiments can provide. Before I discuss our experimental results on 3D localization, I present the key ideas that guided us while we set up the new experiment. In the last part of this chapter I present several additional studies we have started in order to control the energy distribution of the atoms in the disorder and to test the influence of the microscopic properties of the disorder.

6.1 Localization in a weak disorder in 1D

In this section, we review the localization of ultracold atoms in 1D. This allows us to introduce the most important physical quantities, also discussed in chapter 5, and the typical experimental sequence of the expansion experiments we use. In 2008, Anderson Localization of ultracold atoms in one dimensions was shown by two groups in different set-ups. The Florence group, let by Prof. Inguscio, observed the halt of the propagation of ^{39}K non-interacting atoms in a strong bichromatic lattice providing a quasi-disorder

[Roati 08]. Our group, chose to observe the expansion of ^{87}Rb atoms in a weak speckle potential [Billy 08].

6.1.1 Key features 1D localization in a speckle disorder

As all states are localized in 1D (see Sec. 5.3.1), it was possible to investigate localization in a weak disorder, where the disorder amplitude was much smaller than the kinetic energy of the atoms ($V_R \ll E_k$). Therefore, there was no possibility of a classical reflection from a potential barrier and classical trapping could be ruled out in those experiments (see Fig. 6.1 a). Still, as discussed in Ch. 4, the speckle disorder has a typical correlation length σ_R. In such a disorder, only atoms with a wave vector $k = \sqrt{2mE/\hbar^2} < 1/\sigma_R$ undergo a high number of quantum reflections, leading to AL (see Sec. 5.4.1). In other words, for kinetic energies higher than half of the correlation energy $E_R = \frac{\hbar^2}{m\sigma_R^2}$ the localization length diverges and localization becomes very difficult to observe in finite systems. To obtain an unambiguous signature of localization in 1D, it was therefore necessary to work in a configuration, where

$$V_R \ll E_k \leq E_R/2 \ . \tag{6.1}$$

Note that this implies that the experiments were performed in a quantum disorder regime as explained in more detail previously in Sec. 5.4.5.

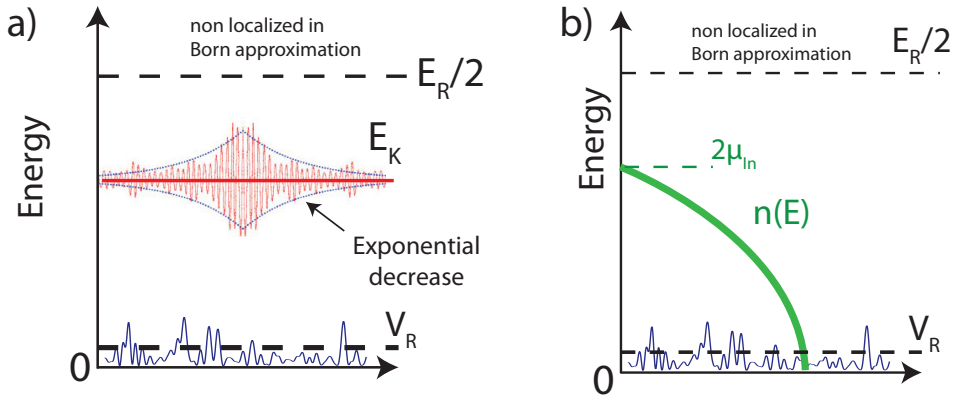

Figure 6.1: **1D AL in a weak speckle disorder**. a) The wave of kinetic energy E_k higher than the average amplitude V_R undergoes multiple quantum reflections on the disorder barriers. The different scattering paths interfere destructively and yield a localized wave function which decreases exponentially. This process is only effective for energies below the correlation energy b) In the experiment we work with a BEC. During the expansion the initial interaction energy is transformed in kinetic energy. Therefore, the atoms have an energy (velocity) distribution $n(E) \equiv n(k)$ with $E = \hbar k^2/2m$. The maximum kinetic energy is given by $E_{Max} = 2\mu_{in}$.

So far, we have always considered the effect of localization for a fixed energy E_k. In practice, a Bose-Einstein condensate was used as atomic source. After switching of the trap the condensate can expand as explained in detail in Sec. 3.1.3. During the first moments of the expansion, the interaction energy of the atoms in the condensate is converted into

kinetic energy. It is then possible to describe the condensate as a superposition of plane waves k with a certain distribution $n(k)$. As the disorder is very weak, we can identify this wave vector distribution with the energy distribution of the atoms in the disorder. In other words, the energy spread induced by the disorder ΔE is much smaller than the kinetic energy E_k of the atoms and k is therefore still a good quantum number (see Sec. 5.4.2). The resulting superposition of matter waves is then characterized by a energy distribution $n(E)$ with a maximum energy controlled by the chemical potential $E_{Max} \approx 2\mu_{in}$ (see Fig.6.1 b).

In the second phase of the expansion, we consider the diffusion of each independent component k of this superposition of plane waves by the weak disorder. After undergoing multiple quantum reflections, each component k gets then Anderson localized on a localization length $\xi(k)$. In the limit $k\sigma_R \leq 1$, that is ($E_k \leq E_R/2$), that we consider here, the localized atomic density profile shows then the exponential decay, on a localization length determined by the maximum kinetic energy [Sanchez-Palencia 07]. Due to the weak disorder, this localization length (typically ≥ 100 μm) is actually much larger than the initial size of the cloud. Therefore, the exponential decay of the wave function, emblematic for AL, was directly observable in these experiments.

6.1.2 Experimental observations

The experiment started with a BEC of $2 \cdot 10^4$ atoms and a chemical potential of $\mu_{in}/h =$ 219 Hz. It was produced in an anisotropic opto-magnetic hybrid trap. A far-off-resonance laser beam created an optical wave-guide along the horizontal z axis. A shallow magnetic trap confined the BEC in the longitudinal direction. At $t = 0$ the longitudinal confinement was switched off, and the BEC started to expand in the guide along the z-direction under the effect of the initial repulsive interaction energy. The atoms would then expand freely along the z-direction over several millimetres. Finally, an in-situ picture of the expanding BEC was taken by fluorescence imaging at any time t. The maximum velocity , and hence the value of the associated kinetic energy E_{Max}, was measured directly by observing this free expansion of the BEC in the waveguide in the absence of disorder. This confirmed that $k_{Max}\sigma_R = 0.65 < 1$ and that it was therefore possible to observed AL as described above.

To study localization, a disordered potential was applied to the expanding BEC using a far-off-resonance blue-detuned optical speckle field, which provided a purely conservative disordered potential. Along the z-direction, the correlation length of the speckle was $\sigma_R = 0.26$ μm ($E_R/h = 1.71$ kHz). When the longitudinal trapping was switched off in the presence of weak disorder ($V_R/\mu_{in} = 0.12$), the BEC started expanding, but the expansion stopped, in stark contrast with the free expansion case, see inset Fig. 6.2 d). The density profiles in linear (Fig. 6.2 c) and semi-log (Fig. 6.2 d) coordinates then showed clear exponential wings, a signature of Anderson localization. An exponential fit to the wings of the density profiles yielded the localization length l_{Loc}, which was then compared to the theoretical value. It showed quite a good agreement between the measurements and the theoretical predictions with no adjustable parameters [Sanchez-Palencia 07].

In summary, a halt of the atoms due to this weak disorder was effectively observed accompanied by an exponential decrease of the atomic density in its wings. These two observations and the good agreement with the theoretical predictions were an unambiguous sign for the observation of AL in one dimension. The success triggered experimental

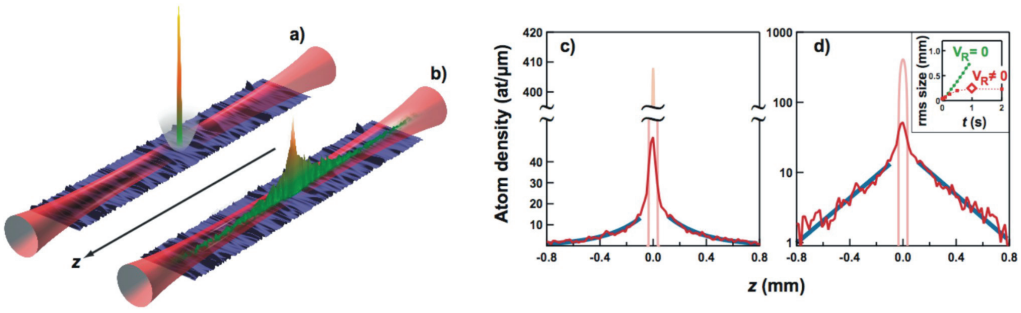

Figure 6.2: **Scheme of the experiment on Anderson Localization in 1D** [Billy 08]. a) A very dilute condensate is created in a hybrid trap (The magnetic field is shown in grey). b) When the magnetic trap is switched off, the condensate propagates along by the optical guide in the presence of a weak disorder. c) and d): Profiles in linear and semilogarithmic scale once the localized regime has been reached. Inset: The expansion is ballistic, when no disorder is present and stops after ~ 1 s when a disorder is applied.

efforts to transpose this scheme to higher dimensions. An implementation of the scheme in the 2D experiment of our group led to the observation of classical diffusion in 2D [Robert-de Saint-Vincent 10]. The newest results obtained on this experiment on disordered physics in 2D can be found in the thesis of Thomas Plisson and Baptiste Allard.

6.2 Transposing the 1D scheme to 3D

It was a key challenge of my PhD to participate in the transposition of the successful 1D scheme to the 3D case. The ultimate goal of the series of experiments we started in 3D is to observe the critical region around the mobility edge in 3D. The experiment is the three-dimensional analog to the ones presented in the previous section. We observe the expansion of a BEC, suspended against gravity, which is released from the initial trap in a 3D optical disordered speckle potential.

In this section we discuss the key ideas that guided our work. We will see that the existence of the mobility edge makes it necessary to work in a strong disorder, which deeply modifies the expected observations in 3D compared to the 1D case, where the observations were made in a weak disorder.

6.2.1 The quantum regime

In 3D, as in 1D, quantum effects are most pronounced at energies well below the correlation energy $E_k \ll E_R$. In this regime the de Broglie wavelength is much larger than the typical size of the valleys σ_R and quantum interference effects gain prevalence (see Sec. 5.4.4). When the disorder amplitude is also smaller than the correlation energy, $V_R \ll E_R$, a typical valley does not support any bound states. In this white-noise limit, we can again rule out classical considerations for the treatment of localization in the same manner as in 1D (see Sec. 5.4.5).

But in sharp contrast to 1D, only the atoms with an energy smaller than the mobility

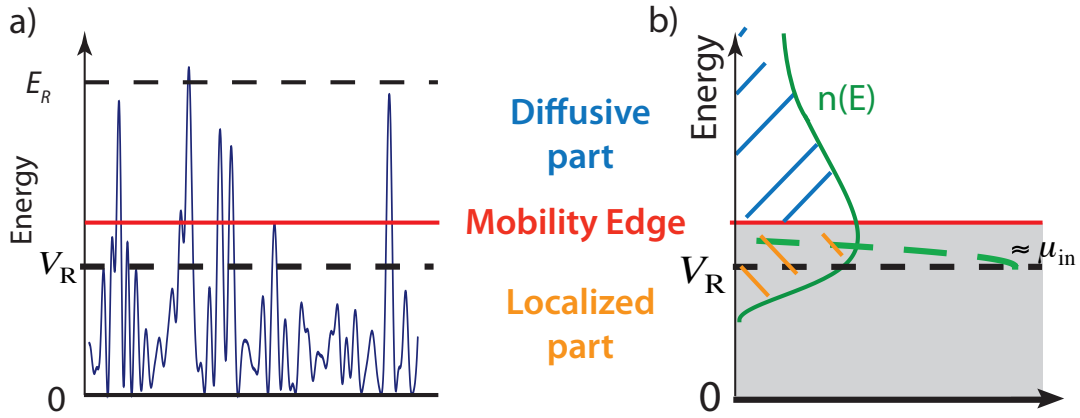

Figure 6.3: **Energy diagram in strong disorder** a) Energy scales in the 3D disorder. Only the states below the mobility edge are localized. b) Energy spread. The sudden switch on of the speckle potential enlarges the energy distribution (green line) heavily, as the initial wave vectors (the dashed green curve) get projected on a large number of different energies. This spreads the energy distribution around the mobility edge (red line) and a diffusive component (blue region) persists at arbitrary strong disorder.

edge $E < E_C$ are localized at 3D (see section 5.3.2). It was the key message of the chapter 5 that localization then only takes place in strong disorder with $E_k \ll V_R$. Our observations of localization in 3D are therefore done in the limit, where

$$E_k \ll V_R \ll E_R \ . \tag{6.2}$$

Note that the correlation energy stays the highest energy scale of the problem, but that the kinetic energy and the disorder amplitude have switched order compared to the 1D case (6.1). Because we now have to work in the strong disorder limit, while maintaining the disorder amplitude smaller than the correlation energy, the kinetic energy of the atoms has to be even smaller than in 1D. In the experiments we obtained typically about $k\sigma_R \sim 0.1$ before the disorder gets switched on. In the following, we study how the fact that we have to work in this strong disorder profoundly modifies the expected observations.

6.2.2 Persistence of the diffusive component at arbitrarily strong disorder

The way the atoms are loaded in the disorder now plays a crucial role. Consider that the disorder is switched on suddenly. The initial states E_k cease to be eigenstates and get projected on a range of energies ΔE during the application of the disorder (see Sec. 5.4.2). In the strong disorder, this energy spread completely overwhelms the initial energy of the atoms and the characteristics of the energy distribution of the atoms $n(E)$ is entirely governed by the properties of the disorder as sketched in Fig. 6.3. Hence, the observed density profile $n(\mathbf{r}, t)$ is the sum of a large number of states $n_E(\mathbf{r}, t)$ spread over different energies

$$n(\mathbf{r}, t) = \int dE \ n(E) \ n_E(\mathbf{r}, t) \ . \tag{6.3}$$

When the modified *energy distribution* in the disorder $n(E)$ spreads to energies higher than the mobility edge E_C, only a fraction of the atoms localizes in the disorder as sketched in Fig. 6.3. In this case, the total density profile is constituted by two components; a time-evolving diffusive component $n_{\mathbf{Diff}}(\mathbf{r}, t)$ of atoms above the mobility edge and a localized component $n_{\mathbf{Loc}}(\mathbf{r})$ of atoms below the mobility edge. The persistence of the two components is probably the most striking difference to the experiments in 1D. It was predicted by several theoretical works [Skipetrov 08, Yedjour 10].

One therefore might be tempted to address the existence of the two components to the sudden application of the disorder. At first sight, ramping the disorder slowly would allow us to load the atoms adiabatically in the deeper energy states and to eliminate the diffusive component. However, this approach has several drawbacks as discussed in more detail in Sec. 6.6.2. First, it is not obvious how one can be adiabatic in a disorder. Second, there are no theoretical predictions that would allow us to test our experimental results. We therefore chose in our experiments to work with the sudden application of the disorder for the investigation of localization.

As the energy distribution spans around the mobility edge some atoms are in the critical region, where the diffusion constant and the localization length show scaling behavior (see Sec. 5.3.3). Having a fine enough resolution this scaling behavior would manifest itself in the dynamics and the shape of the cloud [Skipetrov 08] and would allow us to measure the critical exponents. But as we will see later on in Sec. 6.4, the critical region is too small compared to the energy spread to be observable in our experiments. Still, improving the experimental conditions the investigation of the critical region with our experiment seems not out of reach.

Given that the observed profiles always contain a localized and diffusive component, we now continue with a discussion of the properties of each of them. This allows us then to identify the conditions under which the localized atoms are observable.

6.2.3 Properties of the diffusive component

The dynamics of the cloud should be mainly controlled by the evolution of the diffusive component. The rms of this diffusive component shows then the emblematic $\sigma \propto \sqrt{2Dt}$ behaviour (see section 5.1). To estimate the typical time scales of the evolution, we can use the Ioffe-Regel criterion which tells us that localization arises typically at $(kl_B)_c \sim 1$ (see Sec. 5.25). Using this criterion and the definition of the diffusion constant (5.7) to estimate the typical diffusion constant D_C for the atoms of energy close to the mobility edge

$$D_C \simeq \frac{\hbar}{3m} \simeq 250 \ \ \mu\mathrm{m}^2/s \ . \tag{6.4}$$

Such a small diffusion constant leads to an extremely slow dynamic of the cloud, which has to be observed over typical time scales of several seconds. These very long observation times have been one of the major challenges of the experiments and were one of the major motivations for the installation of a magnetic levitation, as presented in Sec. 3.4.3.

These diffusive atoms might be present at any disorder strength, but at long times these atoms propagate away from the center of cloud and the localized atoms are revealed.

6.2.4 Properties of the localized component

After some seconds the localized atoms have emerged from beneath the diffusive shell. As localization only takes place for energy states which are deeply embedded in the disorder the localization length is very small[1]. For atoms with an energy well below the mobility edge the localization length is typically on the of ~ 1 μm and not ~ 1 mm like in the 1D experiments. This was shown theoretically by Kuhn et al. for an isotropic speckle [Kuhn 07] and for an anisotropic speckle by Piraud et al. [Piraud 12b].

This localization length is well below the resolution of our imaging system. An observation of the exponential profile of the localized states as in 1D was therefore out of reach at this stage[2]. Within our experimental accuracy the localized atoms can then supposed to be frozen at the sudden switch on of the disorder. Hence, the density profile of the localized atoms is a replica of the initial profile at the switch on of the disorder:

$$n_{\mathbf{Loc}}(\mathbf{r},t) = f_{\mathrm{loc}} \cdot n_i(\mathbf{r}) \text{ with } n_i(\mathbf{r}) = n(\mathbf{r}, t = t_i) \tag{6.5}$$

The most important question, at this stage, was of course, how many atoms should be localized and it was very welcome for us that several estimations already existed. Skipetrov et al. estimated in the case of delta-correlated disorder that the localized fraction is effectively never larger then $\sim 45\%$, independently of the strength of the disorder [Skipetrov 08]. Building up on this work, Yedjour et al. estimated the localized fraction for an isotropic speckle potential to be $\sim 60\%$ [Yedjour 10].

6.2.5 Intermediate summary

In conclusion, we have shown, that the existence of a mobility edge in 3D profoundly modifies the expected observations compared to the 1D scheme. As only the deep energy levels are localized, the experiments are performed in the strong disorder regime. This leads to the following key features for an expansion of ultra-cold atoms in a speckle disorder:

- Due to the strong disorder, the energy distribution is completely controlled by the disorder. The spread of this energy distribution is so wide, that the cloud always contains a localized and a diffusive part.
- The diffusive component is always present, but those atoms slowly diffuse away from the center of the cloud, which allows us to observe the localized component. Still, this diffusion is extremely slow and happens on a time scale of several seconds.
- There is a localized fraction of atoms. As only the deep energy states are localized, the localization length is typically much smaller than the initial size of the cloud and the resolution of the imaging system. The dynamics of the localized atoms is therefore essentially frozen at the application of the strong disorder.

We are going to show in the following presentation of our experimental results, that we have indeed observed such a density profile with two components and that the observed localized fraction cannot be explained by classical trapping. We compare those experimental results in Sec. 6.4 with a theory of 3D AL, adapted to our experimental situation

[1] The critical regime is of course an exception to this. But as said previously, it is too narrow to be visible in our experiments

[2] A high NA optical system to be installed in the experiment, will allow us to get closer to this goal.

by our theory team under the guidance of Laurent Sanchez-Palencia, that fully takes into account the large energy distribution and the characteristics of our anisotropic disorder.

6.3 Expansion of ultra-cold atoms in a strong speckle disorder in 3D

In this section we are going to discuss our observations of the expansion of a cloud of ^{87}Rb atoms in a three-dimensional speckle disorder. The results of these experiments were published in *Jendrzejewski et al.*, "Three-dimensional localization of ultracold atoms in an optical disordered potential",Nature Physics **8**,398 (2012). Similiar results on the expansion of a Fermi gas in an strongly anisotropic disorder were obtained simultaneously in the de Marcos group in Urbana-Champaign and published in *Kondov et al.*, "Three-Dimensional Anderson Localization of Ultracold Matter", Science **334** 66 (2011).

6.3.1 The experimental setup

Building upon the experience made during the investigations of 1D AL and the consideration above, we constructed a new apparatus. It was described in detail in chapter 3. The experimental sequence we implemented is a generalization of the 1D scheme, see Fig. 6.4.

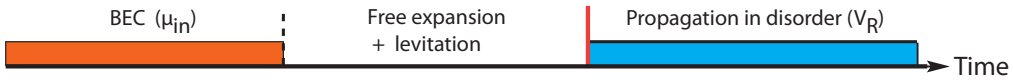

Figure 6.4: **Chronogram for the expansion experiments:** In a first step we create a very dilute condensate as described in Sec. 3.4.2. The initial interaction energy is transformed into kinetic energy during a free expansion. Finally, the disorder is suddenly switched on at t_i and the non-interacting atoms propagate for a time $t - t_i$.

Our experiments on Anderson Localization are performed in three steps (Fig. 6.4). First, evaporative cooling of an atomic cloud of ^{87}Rb atoms in a quasi-isotropic optical dipole trap (trapping frequency $\simeq 5$ Hz) yields a dilute Bose-Einstein condensate of 2.5×10^4 atoms in the $F = 2$, $m_F = -2$ ground state sublevel. It is in thermal equilibrium with about the same number of uncondensed atoms. When the trap is switched off, we can monitor the free expansion of the suspended atomic cloud for several hundred ms due to our magnetic levitation (see Fig. 6.5)[3]. As discussed in Sec. 3.4.4, we obtain from those expansions the values of the initial chemical potential $\mu_{in}/h \sim 40$ Hz and the temperature $T \sim 3$ nK.

Second, we suppress the interatomic interactions by releasing the atomic cloud and letting it expand during 50 ms. At this stage, the atomic cloud has a size (standard half-width) of $\sigma_0 = 30$ μm. The residual interaction energy, estimated to be $E_{\rm int}/h \sim 1$ Hz from Eq. (3.12), is negligible compared to all the other relevant energies of the problem (see below).

[3]We reduced the residual transverse gradients associated with the magnetic levitation by using a strong bias field $B_0 \sim 500$ G [Sackett 06]. The residual expelling potential is isotropic, with an inverse expansion time constant of 1.8 s^{-1}, and plays a negligible role in our experiment. For further details see Sec. 3.4.3

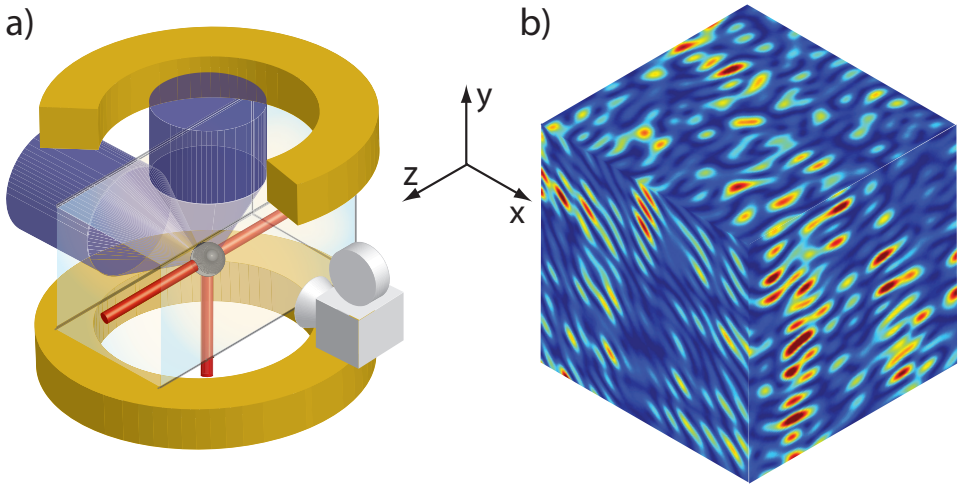

Figure 6.5: **Experimental setup**. a) A dilute BEC of ultracold ^{87}Rb atoms, initially trapped by the red-detuned crossed laser beams, is released and subjected to a repulsive disordered potential (two blue beams). The atoms are suspended against gravity by a magnetic field gradient (produced by the yellow coils), and the expansion of the atomic cloud can be observed for times as long as $6s$. The camera images the fluorescence of the atoms, and yields the atomic column density integrated along the x axis. b) False colour representation of a realization of the disordered potential in the x = 0, y = 0 and z = 0 planes.

Finally, we switch on suddenly (≤ 100 μs) a disorder after the initial free expansion. As discussed in detail in Ch. 4, the disordered potential $V(\mathbf{r})$ is created by the superposition of two crossed speckle fields. The superposition of the two speckle fields has allowed us to limit the anisotropy of our disordered 3D potential considerably. A 3D Gaussian fit of the central peak of the autocorrelation function yields standard radii of 0.11 μm, 0.27 μm and 0.08 μm (see Sec. 4.2.3). We characterize these correlations by a geometric average of 0.13 μm of the standard radii of the autocorrelation function. The associated correlation energy $E_R/h \simeq 6.5$ kHz is then indeed much larger then the kinetic energy of the atoms, thus allowing us to work in the quantum disorder regime.

We chose to work with laser fields with the same polarization in order to minimize classical trapping and maximize the amplitude of the disorder fluctuations (see Sec. 4.2). Using a far-off-resonance blue-detuned optical speckle field ($\lambda = 532$ nm) provides a purely conservative and repulsive disordered potential. The disorder strength is varied in our experiments from 0 up to $V_R/h = 1.1$ kHz, much smaller than the estimated correlation energy of this speckle $E_{R,Exp}/h \simeq 6.5$ kHz and we are working indeed in the limit (6.2) presented in Sec. 6.2. We can estimate the limit of this strong disorder regime to be at $V_R^2/E_R \geq \mu_{in}$ (see Sec. 5.4.9). We operate therefore in the strong disorder regime for disorder strengths $V_R/h \gtrsim 500$ Hz and expect to observe a significant localized fraction.

Finally, we observe the atomic cloud, at a given time t, by direct in-situ fluorescence imaging along the x-axis (see Sec. 3.4.1). This yields the column density

$$\tilde{n}(y,z,t) = \int dx\ n(x,y,z,t)\ . \tag{6.6}$$

The obtained column density profiles were averaged over $3-5$ realizations in order to increase the signal-to-noise ratio. To smooth the signal further, we applied a numerical sliding average over 3 px yielding an effective resolution of 15 μm (full-width at half-maximum) in the $y-z$ plane.

6.3.2 Observations

We have studied how the expansion of the released cloud of atoms is affected when we apply the laser speckle potential. Figure 6.6 shows the evolution of the observed column density profiles for two different values of the disorder amplitude V_R. The obtained profiles have small residual spatial fluctuations, which do not depend on the particular realization of the laser speckle disorder. This can be traced to the averaging arising from the finite spatial resolution of the imaging system. Further, it is consistent with the fact that each profile is a sum of many profiles associated with different atom energy components that probe different, uncorrelated, k-components of the disordered potential. One can then consider that the observed profiles represent, within the experimental accuracy, an ensemble average over different realizations of the disorder.

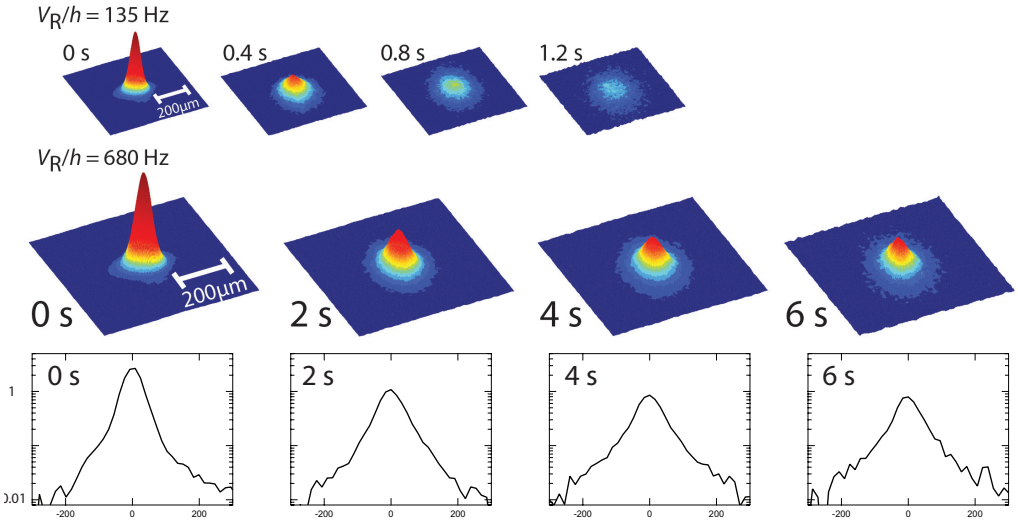

Figure 6.6: **Density profiles after expansion in a strong disorder**. Plots of the column density in the $y-z$ plane, as observed by fluorescence imaging along the x axis (Fig. 6.5 a) at various delays $t-t_i$ after application of the disorder. For a weak disorder ($V_R/h = 135$ Hz), we observe an expansion leading to the disappearance of any observable atomic density for times larger than 1.2s. For a strong disorder ($V_R/h = 680$ Hz), the atomic cloud is still clearly visible after 6 s, and the profile shows a steady peak around the origin, superposed on a slowly expanding component. In the last row we present horizontal cuts of the profiles in a semilogarithmic scale.

For the weaker disorder, $V_R/h = 135$ Hz, the cloud expands considerably. For times longer than 1.2s the size of the cloud is so large that the residual expulsion of the levitation (see Sec. 3.4.3) accelerates the atoms at the outer parts of the cloud. The induced inhomogeneous losses make the observations hard to quantify and we therefore do not

consider times longer than 1.2s for this disorder strength. In contrast, for the strong disorder ($V_R/h = 680$ Hz), the diffusive expansion is slower, and an almost steady peak survives at the centre for observation times as long as 6s. Atom losses were unavoidable for experiments with such long expansion times. But as they are homogeneous, we can compensate those losses by rescaling our data to a fixed number of atoms. A more detailed discussion about those atom losses can be found in appendix A.

6.3.3 Phenomenological model

To analyze our observations, we use a phenomenological model, which relies on the discussion of section 6.2. We assume that the observed profiles are the sum of two contributions:

1. a steady localized part that is the replica of the initial profile $\tilde{n}_i(y,z)$ at $t = t_i$ of the atoms of energy below the mobility edge

$$\tilde{n}_{Loc}(y,z) = f_{\text{loc}} \cdot \tilde{n}_i(y,z) \tag{6.7}$$

2. a diffusive expanding part $\tilde{n}_D(y,z,t)$, whose contribution at the centre decays towards zero.

More precisely, we assume that we can decompose the observed column density as

$$\tilde{n}(y,z,t) = f_{\text{loc}} \cdot \tilde{n}_i(y,z) + \tilde{n}_D(y,z,t) \ . \tag{6.8}$$

6.3.4 The diffusive component

We characterized the dynamics of the cloud by the time evolution of its variance.The evolution of the rms of the whole cloud reflects the diffusive behavior of the diffusive component. We calculated it directly from the observed profile by

$$\langle u(t)^2 \rangle = \sum_u u^2 \tilde{n}(y,z,t) = \sum_u u^2 \tilde{n}(u,t) \ , \tag{6.9}$$

where $u \in \{y,z\}$. As usual, the detected signal contains the actual signal proportional to the atomic density $\tilde{n}_S(y,z,t)$ and a background noise $\tilde{n}_N(y,z)$. Then, we rewrite the above as

$$\langle u(t)^2 \rangle = \sum_{y,z} u^2 \left(\tilde{n}_S(y,z,t) + \tilde{n}_N(y,z)\right) = \langle u(t)^2 \rangle_S + \langle u^2 \rangle_N \ . \tag{6.10}$$

We limited the influence of the noise contribution by a restriction of the summation to a grid of 120×120 points around the center of the cloud. The residual contribution of the noise simply leads to a constant offset in the rms and does not influence the measurement of the diffusion constant D.

We traced the evolution of the variance in Fig. 6.7 a) for two different disorder strengths. In both cases, it shows a linear time dependance

$$\langle u(t)^2 \rangle_S = \sigma_0^2 + 2\langle D^u \rangle (t - t_i) \ , \tag{6.11}$$

This confirms the existence of a diffusive component in the cloud. The global dynamics of the cloud are then characterized by the average diffusion constants

$$\langle D^u \rangle = \int dE \ n(E) \ D^u(E) \tag{6.12}$$

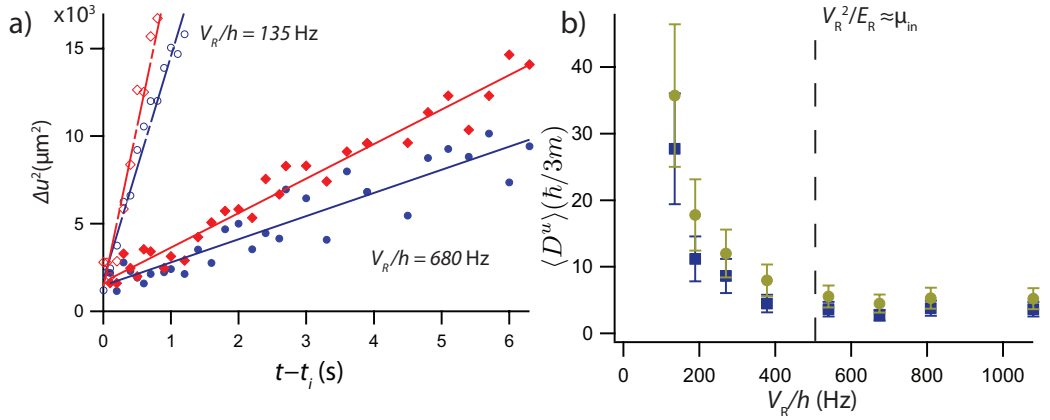

Figure 6.7: **The evolution of the diffusive component.** a) Time evolution of the mean squared widths y (red diamonds) and along z (blue circles) of the column density profiles, and their fits by straight lines, yielding the diffusion coefficients along y and z. The anisotropy of the disorder is reflected in the diffusion coefficients. b) Diffusion coefficient versus disorder amplitude. The yellow circles and blue squares give the experimentally measured diffusion coefficients, $\langle D^u \rangle$, in units of $\hbar/3m$, along the $u = y, z$ axes, respectively. These coefficients are derived from the evolution of the mean squared widths of the atomic cloud. The black, vertical, dashed line marks a very rough estimate of the strong disorder limit using Eq. (5.34). The error bars reflect the effect of background noise on the mean squared widths.

The analysis of the experimental data described above has been carried out for different values of V_R (Fig. 6.7 b). The difference between the diffusion constants in different directions reflects the anisotropy of the disorder. For rather weak disorder strengths the transport length gets reduced for increasing disorder strength, while the energy distribution is only weakly disturbed. This leads to the observed steep decrease with the disorder amplitude V_R of the the averaged diffusion constants in both directions.

At a strong disorder of $V_R/h \sim 500$ Hz, and thus $V_R^2/E_R \geq \mu_{in}$, the energy distribution is entirely controlled by the strong disorder. In this regime the diffusion constant reaches an almost constant values of $D \sim 4 \cdot \frac{\hbar}{3m}$, indicating that the increased disorder strength gets roughly compensated by the increased energy spread. The measured diffusion constants are directly related to $\langle kl_B \rangle$ by Eq. (5.7). Hence, the measured averaged diffusion constants entails that $\langle kl_B \rangle \sim 4$. This value allows us to estimate the strength of the disorder qualitatively. As it it is in the order of the Ioffe-Regel (5.25) criterion, this confirms that we are actually in the strong disorder regime. In such a strong disorder, we expect a non-negligible fraction of atoms to be localized in the disorder. This stationary localized fraction gets revealed from beneath the diffusive component after those have propagated away from the center of the cloud at long expansion times.

6.3.5 The localized component

We can use the time evolution of the central density to measure the localized fraction. Using Eq. 6.8, the central density reads

$$\tilde{n}(0,0,t) = f_{\text{loc}}\tilde{n}_i(0,0) + \tilde{n}_D(0,0,t) \ , \tag{6.13}$$

where $\tilde{n}_D(0,0,t) = \int_{E>E_C} dE\ n(E)\ \frac{1}{2\pi(\sigma_0^2+2D(E)(t-t_i))}$. The diffusive term is proportional to $1/t$ for long times when the size of the initial profile becomes negligible. This $1/(t-t_i)$ dependance stems from the integration over one dimension of the $(t-t_i)^{-3/2}$ evolution expected for the 3D density at the origin. Thus, we determine the finite value of the central density by the fit function

$$\tilde{n}(0,0,t)/\tilde{n}_0 = A + C/(t-t_i) \ , \tag{6.14}$$

where C is a constant that depends on the specific experimental parameters and A is identified with the localized fraction f_{loc}. The localized fraction is found to be equal to 21% for $V_R/h = 680$ Hz, and 1% for $V_R/h = 135$ Hz. In the absence of disorder ($V_R = 0$), we fit the central density by $A + B(t-t_i)^{-2}$, as expected for a ballistic expansion, and find $A = 0$, that is, a null localized fraction.

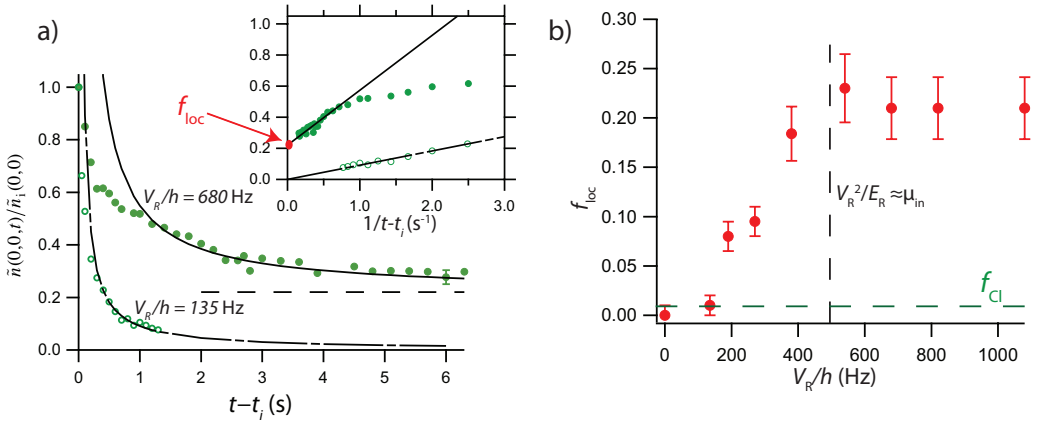

Figure 6.8: **Evolution of the central density.** a) Time evolution of the column density at the centre (green circles). The black line is a fit by the function (6.14). The inset shows the same data plotted as a function of $1/(t-t_i)$, fitted by the black straight line whose intercept on the left axis yields f_{loc}. b) Localized fraction versus disorder amplitude. The points give the localized fraction f_{loc} determined from the decay of the central density. The black, vertical, dashed line marks a very rough estimate of the strong disorder limit using Eq. (5.34). The dashed green limit marks the maximum of the classically trapped fraction as calculated in Sec. 6.3.6. The error bars reflect the uncertainty on each individual fit and the fluctuations from shot to shot.

The phenomenological analysis of the experimental data described above has been carried out for different values of V_R. For weak disorders the mobility edge increases with the disorder strength, while the energy distribution is only moderately changed. This leads to the observed increase of the localized fraction (Fig. 6.8 b), which is vanishingly

small at very weak disorder. In the strong disorder $V_R^2/E_R > \mu_{in}$ the localized fraction reaches a nearly saturated value slightly larger than 20%. It is consistent with the fact that the change of the mobility edge is compensated by the increased energy spread. These observations are in good agreement with our discussion of the diffusive component and the expectations presented in Sec. 6.2. Note that inhomogeneous atom losses (see App. A) entail an overestimation of the localized fraction for $V_R/h < 400$ Hz, so that correcting for it would result in an even steeper increase of the observed localized fraction.

Note further that we have effectively neglected the contribution of the diffusive atoms in the critical region above the mobility edge in this analysis.[4] The calculations by Piraud et al. actually showed that this region is very narrow [Piraud 12b]. Given our much larger energy distribution, its influence is negligible in our experiments. That the time evolution of the central density is actually well described within the phenomenological model (6.8) confirms this further.

6.3.6 Trapped fraction

Finally, it is instructive to compare the experimental observations on the localized fraction with purely classical considerations. The classical mobility edge is the percolation threshold E_P calculated numerically in Sec. 5.4.7. In order to obtain the classically trapped fraction, we also need to calculate the energy distribution $n_{Cl}(E)$ of the atoms in the disorder (see Fig. 6.9 a).

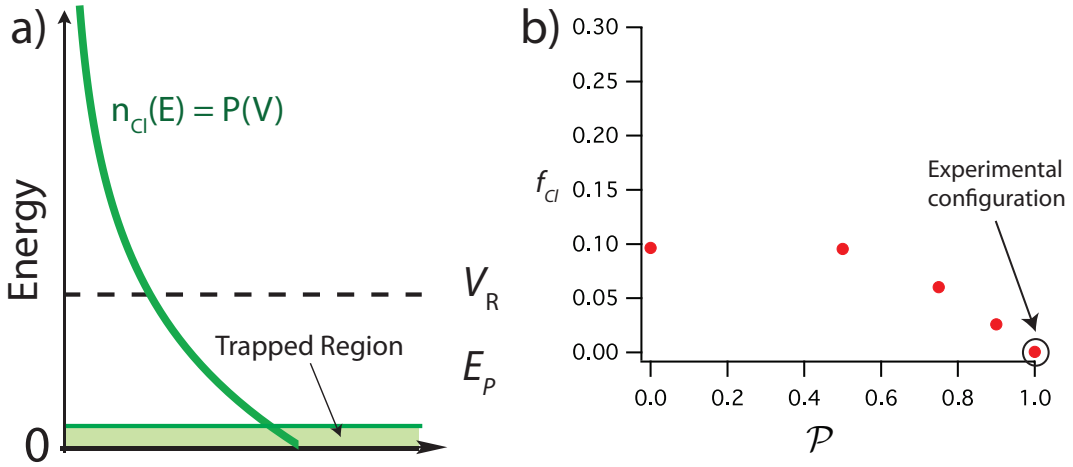

Figure 6.9: **Classical Trapping**. a) Scheme of the classical energy diagram, where E_P is the classical percolation threshold discussed in Sec. 5.4.7. b) The classically trapped fraction.

[4] The diffusion constant for the atoms in the critical region reads $D(E) \simeq \alpha|E - E_C|^s$. Supposing that the energy distribution is constant in the critical region we might write for the corresponding atoms

$$\int_{E>E_C} dE\; n(E)\; \tilde{n}_E(0,0,t) \quad \propto \quad \int_0^\infty dE \frac{1}{1+\frac{2t\alpha}{\sigma_0^2}E^s} \tag{6.15}$$

$$\propto \quad 1/t^{1/s} \tag{6.16}$$

In a strong disorder the initial velocity of the atoms can be neglected. When the disorder is switched on suddenly, the atom at some point $\mathbf{r}$ gains the potential energy furnished by the disorder at this point $V(\mathbf{r})$. The classical energy distribution in the disorder is then the exact reproduction of the intensity distribution of the Speckle potential $n_{Cl}(E) = P(V)$. As discussed in Sec. 4.2.1 this intensity distribution has a well-known analytical expression Eq. (4.19). We can then calculate the classically trapped fraction

$$f_{Cl} = \int_0^{E_P} dE\, n_{Cl}(E) \tag{6.17}$$

$$f_{Cl} = 1 - \frac{\mathcal{P}-1}{2\mathcal{P}} e^{2E_P/(1-\mathcal{P})} - \frac{P+1}{2\mathcal{P}} e^{-2E_P/(\mathcal{P}+1)} \tag{6.18}$$

The resulting trapped fraction, shown in Fig. 6.9, is $\leq 1\%$ for the coherent superposition of the speckle fields, $\mathcal{P} = 1$, chosen in the experiments. This trapped fraction is negligibly small compared to the experimentally observed one of $\sim 21\%$. It would increase up to 8% in the completely incoherent superposition, which would make the differentiation between classical trapping and localization more involved (see Sec. 6.5.1).

6.3.7 Summary of the experimental observations

In conclusion, we have observed a cloud containing two components as shown in Fig. 6.10. The time evolution of the rms has shown a clear $\sqrt{t}$ dependance, providing a clear

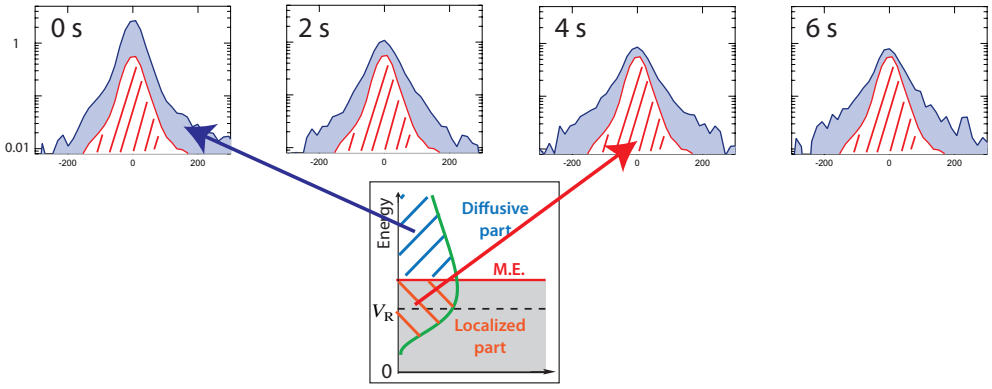

Figure 6.10: **The components of the density profiles.** We decompose the atomic column density profiles (slices through the density profiles) into two components. The low energy states are localized on short distances (red striped) and hence stationary. The high energy states (blue) above the mobility edge are diffusive and evolve over time.

signature of a diffusive component.

The measured diffusion constants were within the magnitude one expects in the strong disorder regime, where AL should take place. Further, we have measured a localized fraction of $\sim 21\%$ from the evolution of the central density.

The localization we observe cannot be interpreted as classical trapping of particles with energy below the classical percolation threshold in the disorder, which is well below

the average energy of the atoms. Similarly, quantum trapping in local potential minima is excluded, because the local potential wells are too tight to support stationary states with energy less than the potential well depth. Therefore, our observation yield good evidence for the existence of an Anderson localized component in the cloud.

6.4 Comparision to the theoretical model

To go further, we compare our results to the predictions of a theory of AL, which is adapted to the characteristics of our experiments. We compare the experimental results on the atomic profiles, the diffusion constants and the localized fraction with a self-consistent theory of AL (see Sec. 5.4.9). The methods used by the theory team, consisting of Marie Piraud, Luca Pezzé and led by Laurent Sanchez-Palencia, are described in detail in [Piraud 12b] and the PhD of Marie Piraud.

The density profile of each energy state $n_E(\mathbf{r}, t)$ from Eq. (6.3) was calculated with a self-consistent theory within the so-called "on-shell" approximation. In this approximation one takes into account the energy broadening by the disorder, but one neglects possible shifts in its dispersion relation. The theory was specifically applied to our situation, taking into account:

1. the spatial extension of the atomic gas at the initial time t_i;
2. its energy distribution induced by the sudden application of the disordered potential at time t_i;
3. the full correlation function of the 3D speckle potential.

The self-consistent theory provides the mobility edge E_C and the density profiles for different energies $n_E(\mathbf{r}, t)$. Further, the energy distribution in the disorder $n(E)$ had to be calculated numerically as we know of no simple experimental method for determining it precisely.

We are going to do the comparison between the theory and the experiment in 4 steps: First, we present the shape of the localized component, to confirm that the localized shape is actually a replica of the initial density profile. Second, we compare the observed localized fraction with the theoretical prediction. There we find that we have to introduce an ad-hoc energy shift in order to obtain a good agreement. Third, we compare the diffusion constants, taking into account the energy shift. Finally, we can compare the resulting theoretical predictions for the density profiles to the experimental results.

6.4.1 The localized shape and fraction

In the AL regime, $E < E_C$, the density profiles $n_E(\mathbf{r})$ are static and exponentially localized. They are characterized by the energy-dependent localization lengths $L^u_{loc}(E)$, which are different for each spatial direction. As expected, the calculated localization lengths increase with the energy and diverge in the proximity of the mobility edge E_C. Except in the narrow window ΔE (for example, $\Delta E/h \sim 20$ Hz for $V_R/h = 680$ Hz), below E_C, they remain smaller than the imaging resolution, and much smaller than the size of the atomic cloud when the disorder is switched on .

The energy distribution $n(E)$ of the atoms in the disorder was calculated numerically. As shown in Fig. 6.11 for the case of $V_R = 680$ Hz, it is peaked around V_R with a width of

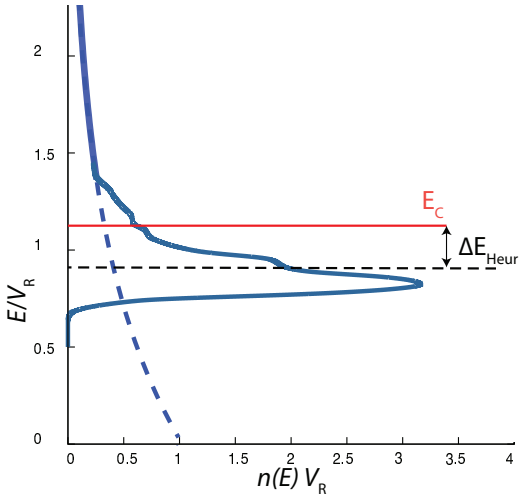

Figure 6.11: **Theoretical prediction of the energy diagram**. The straight blue curve marks the energy distribution $n(E)$. We added the classical prediction from the previous section as a dashed blue line. The red line marks the mobility edge E_C calculated from the self-consistent theory of localization. An ad-hoc energy shift ΔE_{Heur} between the center of the energy distribution and the mobility edge was introduced to take into account the uncertainties on the calculations of the mobility edge and the energy distribution and as well as experimental uncertainties.

$\Delta n_E/h \sim 140$ Hz. As most of the energy components are outside of the window, where the localization length diverges, the localized profile is simply a replica of the initial profile $\tilde{n}_i$, supporting the form chosen for the first term in Eq. (6.8) used for the phenomenological analysis.

Second, we want to compare the measured localized fraction, i.e. the fraction of atoms with energy below the mobility edge, to the theoretical predictions. Within the used theory, it was found that the mobility edge is positioned at $E_C - V_R \simeq 1.6V_R^2/E_R$ for our experimental parameters. When we calculate the fraction of atoms below the mobility edge, we find numerical results significantly larger than the measured values. Actually, due to the very peaked form of the energy distribution the numerical value found for f_{loc} is extremely sensitive to the numerical accuracy in the determination of $n(E)$ as well as to any approximation in the theoretical calculations of E_C. It is also very sensitive to uncertainties in experimental parameters, in particular the amplitude V_R and the details of the disordered potential. Considering all these uncertainties, we introduced into the calculation of f_{loc} a heuristic energy shift ΔE_{Heur} between the energy distribution $n(E)$ and the mobility edge, see Fig. 6.11.

We found that a relative shift of the form $\Delta E_{Heur} = 3.35V_R^2/E_R$ ($\Delta E_{Heur}/h \sim 225$ Hz for $V_R/h = 680$ Hz) leads to a fair agreement with the experimental results (Fig. 6.12 a). Note that ΔE_{Heur} is approximately twice as large as $E_C - V_R$ and the width of the energy distribution Δn_E . It thus strongly affects the value of f_{loc}.

More recent and refined calculations of the mobility edge by Piraud et al. have taken into account possible shifts of the dispersion relation in the disorder [Piraud 12b]. The found shifts of the mobility edge are in the same order as the heuristic one used in this

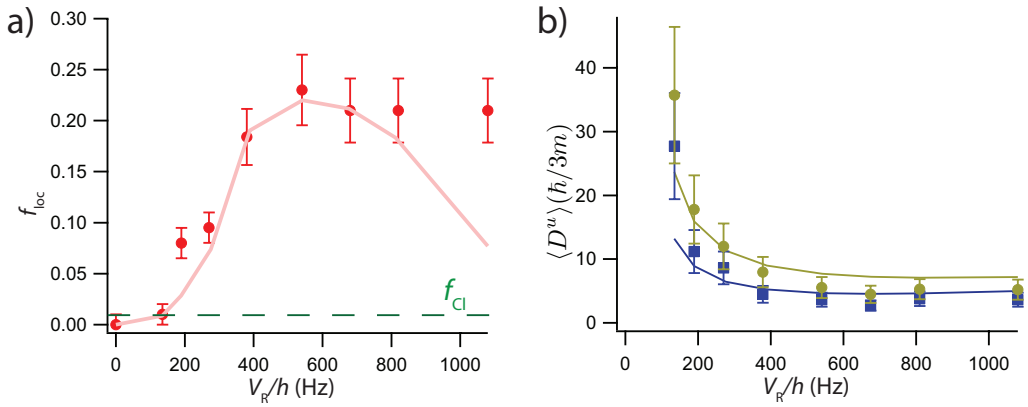

Figure 6.12: **Comparision experiment vs theory for different disorder amplitudes.** a) Localized fraction. The points give the localized fraction f_{loc} as in Fig. 6.8. The solid line shows the results of the theoretical calculation, including the heuristic relative energy shift explained in the text. The green dashed line marks the upper limit for the classically trapped fraction as discussed in Sec. 6.3.6 b) Diffusion coefficient. The yellow circles and blue squares give the measured diffusion coefficients as in Fig. 6.7. The yellow (y) and solid blue (z) lines show the results of the theoretical calculation of these coefficients, using the same heuristic energy shift.

analysis. This signals that the heuristically shift might be partially due to the "on-shell" approximation done in the calculations in the mobility edge.

To conclude on this determination of the mobility edge, we would require a reliable determination of the energy distribution in ultracold-atom experiments, which is not available yet.

6.4.2 The diffusive component

We can now go on with a comparison of theory and experiment in the diffusive regime. In the diffusive regime, $E > E_C$, the density profiles $n_E(\mathbf{r}, t)$ are time-dependent, Gaussian functions. They are characterized by the energy-dependent diffusion constants $D^u(E)$, which are different for each spatial direction. They are calculated within the self-consistent theory at each energy E. To be consistent with the calculation in the previous section, we use the same energy shift as introduced in the calculation of the localized fraction, to calculate the average diffusion constant $\langle D^u \rangle$. That is, we write

$$\langle D^u \rangle = \int_{E>E_C} n(E - \Delta E_{Heur}) D^u(E)\, dE \tag{6.19}$$

As shown in Fig. 6.12 b), we find a fair agreement between the results of this calculation and the experimental data. In particular, the anisotropy of the diffusion constants $\langle D^x \rangle / \langle D^z \rangle \sim 1.8$ is reproduced well. Note that the theoretical calculations do not involve any free parameter, apart from the heuristic energy shift discussed above.

6.4.3 The profiles

Finally, we can compare the observed profiles to the theoretical predictions. Figure 6.13 shows the comparison between them, at various delays, in the case $V_R/h = 680$ Hz. The theoretical profiles represent equation (6.3), where $n(E)$ and $n_E(\mathbf{r}, t)$ are calculated as explained above.

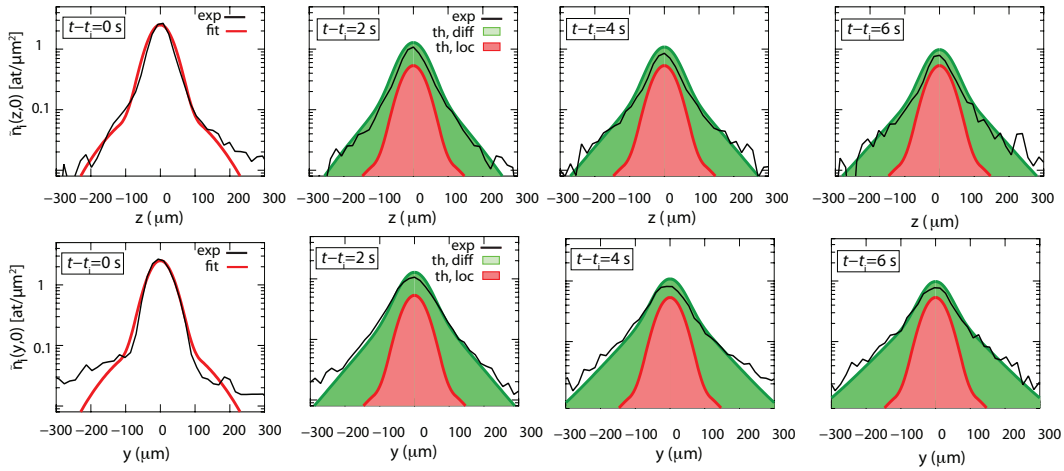

Figure 6.13: **Evolution of the density profiles in a strong disorder: experiment versus theory**. The figure shows cuts of the column density profiles along y ($\tilde{n}(y, 0, t)$, bottom row) and z ($\tilde{n}(0, z, t)$, top row), at various delays after application of the disorder with amplitude $V_R/h = 680$ Hz. The solid black lines are the experimental data. In the first column (corresponding to the initial time $t = t_i$), the solid red lines are fits to the data. In all other panels (corresponding to $t > t_i$), the solid red lines are these fitted initial profiles multiplied by the localized fraction $f_{\mathrm{loc}} = 0.21$, hence describing the localized part. Adding the theoretically determined diffusive parts at various delays, we obtain the green profiles, which reproduce well the experimental profiles.

These theoretical profiles are composed of a localized part (replica of the initial profile multiplied by the calculated localized fraction; red line), plus an evolving diffusive part (the green line is the sum of the two parts). The fair agreement with experimental profiles at various delays shows the consistency of our theoretical analysis, including the heuristic energy shift, with the experimental observations.

6.4.4 Conclusions

Recall that our observations are incompatible with classical trapping, owing to the very low value of the percolation threshold, or with quantum trapping, because our disorder does not support bound states. Moreover, the self-consistent theory of AL applied to the exact experimental situation yields good quantitative agreement with the experimental results, provided we use the energy distribution of the atoms, which is strongly modified by the sudden application of the disorder, and displace it by a heuristic shift.

Altogether, those experiments allowed us to report the first evidence of 3D Anderson localization of ultracold atoms in the presence of a well-controlled optical disorder. Be-

cause of the wide energy distribution of the atoms induced by the disorder, it has not been possible, in that experiment, to reach a regime where all atoms would be localized. The development of new methods to precisely determine and control the atom energy distribution is now a priority of the ongoing work in our team. This continued effort will be particularly important as there exists no exact theory for Anderson Localization in 3D. The comparison of our recent experiments with this theory, adapted to our specific configuration by our theory team led by Laurent Sanchez-Palencia, already suggested that the standard self-consistent theory should be refined [Piraud 12b]. Pursuing this fruitful collaboration, we aim to test this theory over a wide range of disorder parameters experimentally.

We continued our investigations with these two major objectives in mind. First, we try to find a new method to precisely control the energy distribution in the disorder. Second, we varied the parameters of the disorder to investigate the influence of the microscopic parameters. We will now present several preliminary results of those investigations.

6.5 First studies on the influence of the disorder properties

In a first series of experiments, we wanted to investigate the dependance of the localized fraction, the diffusion constants and the profiles on the microscopic properties of the speckle potential. In order to do so we can modify the intensity distribution of the disorder by passing from a coherent superposition between the two speckle fields to an incoherent one. We discuss the experimental results of these experiments in the next section. It is further very tempting to study the dependance of the mobility edge on the form of the rather easily tunable autocorrelation function (see Sec. 4.1.4) . We explain how we can modify this correlation function experimentally in Sec. 6.5.2.

6.5.1 Expansion in an incoherently crossed speckle

The easiest way to modify the intensity distribution of the speckle disorder is to change the polarization of the lower speckle arm. By turning the half-wave plate installed directly in front of the diffuser, we can control the polarization in this arm (see Sec. 4.2.3). Hence, we can pass continuously from the coherent superposition, when polarizations in the two arms are parallel, to an incoherent one, when the polarizations are perpendicular (see Sec. 4.2). Modifying this superposition from coherent to incoherent strongly modifies the intensity distribution of the disorder as the very low intensities are inhibited in the incoherent superposition (see Fig. 6.14 a).

We have performed the same expansion experiments as presented in the previous section in this configuration. The observed diffusion constant does not differ substantially from the ones observed in the coherently superposed disorder. The measured localized fractions are compared to the theoretical predictions in Fig. 6.14 b). We applied the same theory self-consistent of AL as described in the previous section, including the same heuristical energy shift that we introduced in Sec. 6.4. On the diffusion constant we did not observe more than slight changes and the localized fraction is only slightly lower. This is certainly due to the very peaked shape of the energy distribution in the disorder $n(E)$, which was calculated numerically. Then, the low energies are only weakly populated, and our observations are therefore insensitive to the strong modifications of the intensity distribution in this region.

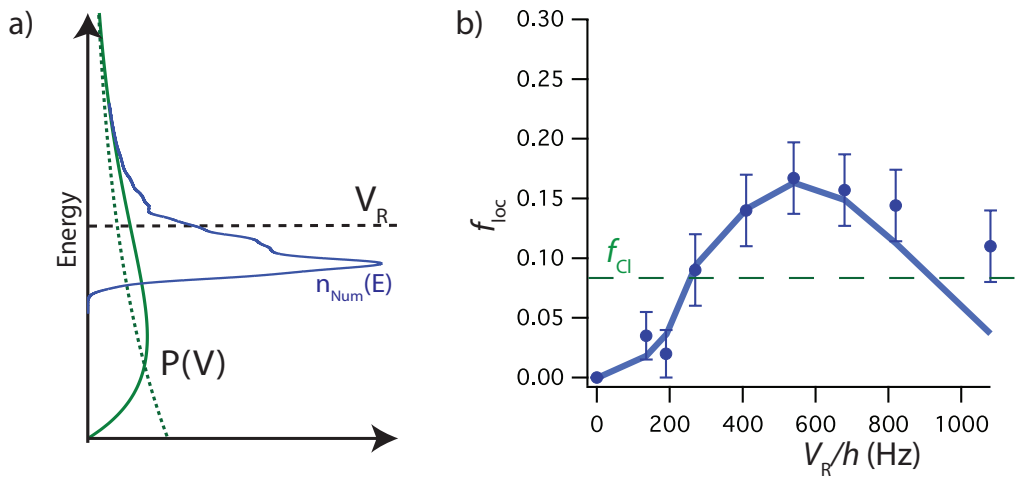

Figure 6.14: **Incoherently superposed speckle disorder**. a) Intensity distribution in the incoherent case (green straight line). The coherent case is added as the green dashed line. The straight blue line represents the numerically calculated energy distribution in the disorder. b) The localized fraction. The experimental data are represented as the blue dots. The blue straight line represents the theoretical predictions including the same heuristical shift as in Sec. 6.4. As in the previous section the observed localized fraction is significantly higher than the upper classical limit (horizontal green dashed line).

As mentioned above the low intensities are strongly inhibited in the incoherent superposition of the speckle fields. The regions of low intensities are therefore rarely connected and the percolation threshold increases substantially (see Sec. 5.4.8). One then expects within the classical model, presented in Sec. 6.3.6, that the classically trapped fraction increases to 8%. Obviously, these classical considerations are completely contrary to the behavior we observe here. We observed experimentally and theoretically that the localized fraction actually decreases compared the case of a coherent superposition of the speckle fields. We may see this as a further evidence that the localization we observe is due to 3D AL.

6.5.2 Modification of the correlations in the disorder

We also started to test possible effects of a modification of the correlation function on the expansion of the atoms in the disorder. Changes of the correlation lengths of the disorder allow us to modify the value of the associated energy, the correlation energy E_R (see Sec. 5.4.4). Such a variation will allow us for example to better define the precise value of the correlation energy for such rather complicated correlation functions like the one we are using in our experiments. Fundamental quantities such as the scattering time, the transport time and maybe most importantly the mobility edge depend on this correlation energy (see the corresponding sections in Ch. 5). Further we have seen that we pass from the quantum disorder regime,$V_R < E_R$, to a classical disorder regime, $V_R > E_R$, when the disorder amplitude is getting bigger than the correlation energy. We expect that this crossover influences strongly the position of the mobility edge in the speckle disorder, but

conclusive results from the theoretical and experimental side are still missing.

A simple first possibility to change the correlation lengths of the disorder is to vary the numerical aperture by reducing the beam diameter. This way we reduce the correlation energy strongly and investigate the classical regime. We can also achieve very anisotropic configurations, when we work in a speckle disorder created by only one single arm. Then the longitudinal correlation length is much larger then the transverse one. In the case of strong anisotropy, the dimensionality will effectively be reduced to quasi-2D configurations, resulting in strong modifications of the physical properties of the disordered system [Zhang 90, Abrikosov 94, Kaas 08]. It would then be interesting to attempt the observation of phenomena like transverse AL, which was already observed in with ultrasound [Hu 08]. [5]

Such experiments, which stayed very preliminary up to now, promise to give further insight into the open question on the influence of correlations on localization.

6.6 Towards a better control of the energy distribution

The experiments presented in Sec. 6.3 mark a first step towards the investigation of the critical behavior around the mobility edge with ultracold atoms. Important experimental efforts are still needed, especially to enable a better control and detection of the energy distribution. We do not know any easy experimental method to measure that distribution. We will discuss our first results obtained from time of flight measurement, but they only yield the momentum distribution, which cannot be directly related to the energy distribution in disordered systems. The development of new methods to precisely determine and control the atom energy distribution is now a priority of the ongoing work in our team. First attempts on doing so with ramped disorders are presented.

6.6.1 Experiments on the momentum distribution

For long enough times, time of flight (ToF) measurements allow us to directly observe the velocity distributions of the cloud in the disorder (see. Sec 3.1.3). Because of our magnetic levitation we can perform such measurements with high precision allowing us to investigate the momentum distribution even for small velocities of less than 0.3 mm/s. These velocity distributions provide us with a direct measurement of the distribution of the kinetic energy $n(E_k)$ in the disorder. To do those ToF measurements, we perform the same the sequence as previously, but add an expansion in the suspending potential after we switch off the disorder.

Results of such ToF measurements after the propagation in a coherently superposed disorder at $V_R/h = 680$ Hz are shown in Fig. 6.15 a). Due to the sudden application of the disorder the momentum distribution gets enlarged. After a propagation time in the disorder t_{Diff} of typically some ms, the form of the enlarged momentum distribution does not change anymore and can be fitted by a Gaussian with mean velocity $\bar{v} = 0.4$ mm/s. This mean velocity corresponds to a kinetic energy of $E_k = m\bar{v}^2/2 = h \cdot 17$ Hz, compared to $h \cdot 5$ Hz extracted from the free evolution.

[5] We used such a disorder configuration for our studies on the coherent backscattering of ultracold atoms that we are going to present in Ch 7.

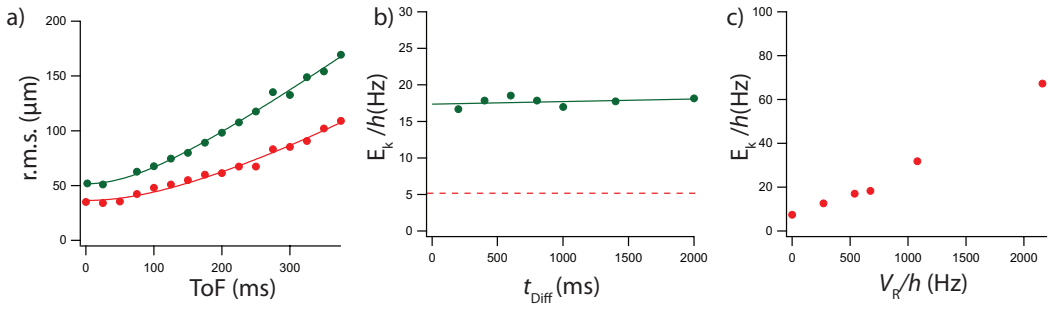

Figure 6.15: **ToF experiments**. a) ToF measurements with (green) and without (red) disorder. The measured mean velocity for the free expansion is 0.22 mm/s. The datas in the disorder are taken after a propagation time of 100 ms in a disorder of amplitude $V_R/h = 680$ Hz. The mean velocity is increased to 0.4 mm/s b) Kinetic energy depending on the diffusion time in the disorder. From the linear fit we obtain a slope of < 1 Hz/s. The dashed red line is the mean kinetic energy before the atoms are loaded in the disorder. c) Kinetic energy depending on the disorder amplitude after a propagation time of 200 ms.

We have performed these measurements for propagation times in the disorder as long as 2 s (see Fig. 6.15 b). The increase of the kinetic energy is less than $h \cdot 1$ Hz/s and compatible with zero, which means that there is no observable heating during the expansions.

We have measured the mean kinetic energy for different disorder amplitudes as pictured in Fig. 6.15 c). We can clearly identify the expected increase for stronger disorders. Still, unlike in the harmonic trap, there exists no simple connection between the potential and the kinetic energy in disorder. An analysis of those obtained data will therefore require a substantial amount of work and has to be left to future investigations.

It would also be compelling to relate the measured momentum distributions to the energy distribution in the disorder. But unlike the virial expansion in a harmonic trap, we do not know of such a connection in the disorder. Hence, the momentum distributions do not provide us with a simple way to measure the energy distribution and other experimental approaches have to be used.

6.6.2 Ramped scheme

In our first attempts to control the energy distribution, we tried to optimize the loading of the atoms in the disorder. Naively, we could expect to obtain a nearly adiabatic evolution by slowly ramping the disorder to its full height and after the propagation to zero. The merit would be twofold. First, it would allow to reduce the energy spread ΔE and further to lower the mean energy of the atoms. We would therefore expect to load the atoms in the deeper energy states and to increase the localized fraction. To test the possibility of such an adiabatic loading, we observed the momentum spread. An example is shown in Fig. 6.16 a).

When we apply sudden switches as in the experiments presented before, the momentum spread increases with the disorder strength (blue squares). We have then ramped the

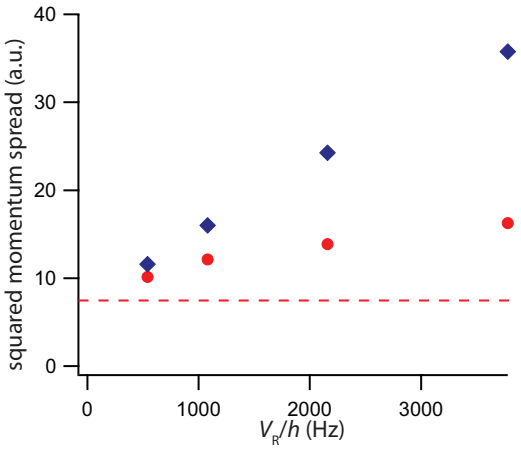

Figure 6.16: **Momentum spread in the disorder.**. The sudden switch on (blue squares) is used in the experiments presented before. We were able to reduce the spread with a ramped disorder (red dots) with ramp times of $\simeq 15$ ms for the switch on and off. The dashed red line marks the momentum spread before the propagation in the disorder.

disorder linearly up to its full strength let the atoms propagate for about 100 ms and ramped it back to zero. Ramp times of ~ 15 ms allowed to reduce the momentum spread strongly (red dots) to the vicinity of the velocity spread before the loading in the disorder. Neither longer ramp times nor more sophisticated ramp forms allowed to reduce the spread much further.

To our disappointment, this reduced momentum spread did not manifest itself in qualitative changes on the observed localized fraction or the diffusion constants compared to the scheme we used in Sec. 6.3. As said above, a slow adiabatic switch on of the disorder seemed to be a good candidate to control the energy distribution. Starting with the well controlled initial energy provided by the realization of a Bose Einstein condensate, we expected to populate the wanted low energy levels. For non-interaction bosons in the disordered systems there seems to exist no gap in the excitation spectrum. This absence of a gap makes it extremely hard to be adiabatic in a speckle disorder. This difficultly to reach adiabaticity in presence of disorder [Zakrzewski 09, Edwards 08], has been predicted theoretically. The existence of a quantum phase transition around the mobility edge makes the question about adiabaticity even more involved [Barankov 08, Polkovnikov 11].

Even if the possibility of ramped disorder might be pursued further, these important open questions definitely call for alternative, more sophisticated techniques and probes to be developed

6.7 Conclusions

In this chapter we have discussed our experimental results on 3D AL. First, we presented how we transposed the successful scheme that allowed for the observation of one-dimensional Anderson Localization to the three dimensional case. In the second part, we detailed our expansion experiments, where we monitored the three-dimensional expansion of an initial BEC in the presence of a quasi-isotropic laser speckle disorder and observed

an atomic cloud composed of two components: a localized and a diffusive part. These components respectively correspond to energy levels below and above the mobility edge. Because of the wide energy distribution of the atoms induced by the disorder, it has not been possible, in that experiment, to reach a regime where all atoms would be localized, but the existence of a localized fraction is beyond any reasonable doubt.Altogether, those experiments allowed us to report the first evidence of 3D Anderson localization of ultracold atoms in the presence of a well-controlled optical disorder. This marks a first step towards the precise investigation of the critical behavior around the mobility edge with ultracold atoms.

In the last part of the chapter, we discussed the first experiments to enable a better control and detection of the energy distribution. The development of such new methods to precisely determine and control the atom energy distribution is now a priority of the ongoing work in our team. Further work on the control and detection of the energy distribution can be inspired by the experiments on the one-particle excitation spectrum of a strongly interaction Fermi gas by the Jin Group [Stewart 08]. More recently this technique was transposed to measurements in optical lattices using Bragg diffraction [Clément 09]. This investigation promises to give deeper insight into the problem of 3D AL.

This will be particularly important as there exists no exact theory for Anderson Localization in 3D. The comparison of our recent experiments with the self-consistent theory, adapted to our specific configuration, already suggested that the standard self-consistent theory should be refined. Pursuing this fruitful collaboration, will allow to test this theory over a wide range of disorder parameters experimentally.

CHAPTER 7

Experiments on Coherent Backscattering

Quantum inference effects play a fundamental role in our understanding of quantum transport through disordered media, as it can lead to the suppression of transport, i.e. Anderson Localization (AL). We presented in the previous chapter that it has become recently possible to directly observe Anderson localization with ultra-cold atoms in one dimension [Billy 08, Roati 08] and three dimensions [Kondov 11, Jendrzejewski 12a]. Convincing as they are, none of these experiments includes a direct evidence of the role of coherence.

For weak disorder, a first order manifestation of coherence is the phenomenon of coherent backscattering (CBS), *i.e.* the enhancement of the scattering probability in the backward direction, due to a quantum interference of amplitudes associated with two opposite multiple scattering paths [Watson 69, Tsang 84, Akkermans 86, Langer 66, Gor'kov 79, Abrahams 79].[1] A direct observation of such a peak is a smoking gun of the existence of quantum coherence in quantum transport in disordered media.

In this chapter, we report on the direct observation of CBS with ultra-cold atoms, in a quasi two-dimensional (2D) configuration. After a brief review of the CBS mechanism, we discuss our experimental sequence. We then present how those experiments allowed us to measure the scattering and the transport time, before we turn our attention to the analysis of the CBS signal. The results of those experiments were published in *Jendrzejewski et al.*, "Coherent Backscattering of Ultracold Atoms", Physical Review Letters **109**, 195302 (2012). During the preparation of this manuscript we have been made aware of an independent similar observation [Labeyrie 12]. We conclude the chapter with the presentation of first results on the energy dependance of the scattering and the transport time.

7.1 The coherent backscattering mechanism

To understand the origin of that CBS peak, we follow a similar very simple discussion as in Sec. 2.2, which were strongly motivated by the Ch. 8 of [Akkermans 07]. Let us consider an input plane matter-wave with initial momentum $\mathbf{k}_i$ that experiences multiple scattering towards a final momentum $\mathbf{k}_f$ (see Fig. 7.1). The scattering amplitude may be written as

$$A(\mathbf{k}_f, \mathbf{k}_i, t) = \sum_{\mathbf{r}_{1,2}} f\left(\mathbf{r}_1, \mathbf{r}_2, t\right) e^{i(\mathbf{k}_i \cdot \mathbf{r}_1 - \mathbf{k}_f \cdot \mathbf{r}_2)} \ , \tag{7.1}$$

where $f(\mathbf{r}_1, \mathbf{r}_2)$ is the amplitude associated to the propagation from $\mathbf{r}_1$ to $\mathbf{r}_2$. As we see in Fig. 7.1 we have to consider for each multiple scattering path the reversed path

[1] In Condensed Matter Physics, those quantum interferences are the basis of the weak localization phenomenon [Altshuler 82, Akkermans 07] discussed in Sec. 2.2 and Sec. 5.2.1.

with the same input $\mathbf{k}_i$ and output $\mathbf{k}_f$. Those counter-propagating paths acquire a phase $\delta\phi = (\mathbf{k}_i + \mathbf{k}_f) \cdot (\mathbf{r}_1 - \mathbf{r}_2)$ The total disorder averaged propability to scatter from $\mathbf{k}_i$ into $\mathbf{k}_f$ is then given by (see Sec. 2.2)

$$\overline{P(\mathbf{k}_f, \mathbf{k}_i, t)} = \overline{\sum_{r_{1,2}} |f(\mathbf{r}_1, \mathbf{r}_2, t)|^2 (1 + e^{i(\mathbf{k}_f + \mathbf{k}_i)\cdot(\mathbf{r}_1 - \mathbf{r}_2)})} \tag{7.2}$$

$$= \overline{\sum_{r_{1,2}} |f(\mathbf{r}_1, \mathbf{r}_2, t)|^2} + \overline{\sum_{r_{1,2}} |f(\mathbf{r}_1, \mathbf{r}_2, t)|^2 e^{i(\mathbf{k}_f + \mathbf{k}_i)\cdot(\mathbf{r}_1 - \mathbf{r}_2)}} \tag{7.3}$$

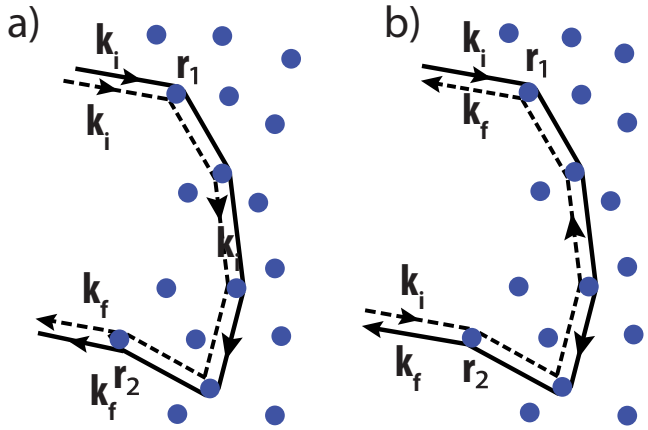

Figure 7.1: **The CBS mechanism**. The probability to scatter from some input momentum $\mathbf{k}_i$ to some final momentum $\mathbf{k}_f$ is given by the sum over all co-propagating (a) and counter-propagating paths (b).

For the *exact* backward momentum $\mathbf{k}_f = -\mathbf{k}_i$, the interference is always perfectly constructive, whatever the considered multiple scattering path. This coherent effect survives the ensemble averaging over the disorder, so that the total scattering probability is twice as large as it would be in the incoherent case. For an increasing difference between $\mathbf{k}_f$ and $-\mathbf{k}_i$, the interferences are progressively washed out as we sum over all interference patterns associated with all multiple scattering paths. It results in a CBS peak of width inversely proportional to the spread in the separations. More precisely, the peak at time t is the Fourier transform of the distribution of the separations $\mathbf{R} = \mathbf{r}_1 - \mathbf{r}_2$.

For long times multiple scattering has occurred and diffusion, characterized by a diffusion constant D, is established (see Sec. 5.1). Then, the distribution of $\mathbf{R}$ is a Gaussian of width $\sqrt{2Dt}$

$$|f(\mathbf{r}_1, \mathbf{r}_2, t)|^2 = \frac{1}{\sqrt{4\pi D t}^3} e^{-\frac{\mathbf{R}^2}{4Dt}} . \tag{7.4}$$

Going to the continuous limit allows us to perform the integral over $\mathbf{r}_{1,2}$ in Eq. (7.2) and we obtain for the momentum signal the analytical equation

$$P(\mathbf{k}_f, \mathbf{k}_i, t) = C \cdot (1 + e^{-2Dt(\mathbf{k}_f + \mathbf{k}_i)^2}) , \tag{7.5}$$

where C is some normalization constant. The first term is the incoherent contribution, associated with the classical diffusion we discussed in Sec. 5.1. The second part on the other hand is the CBS signal we want to observe. It is the momentum space signature of the weak localization correction discussed in Sec. 5.2.1. Its observation is therefore a direct signature of phase coherent transport in disorder.

In optics, where the pioneering work on CBS were done, it is far more easy to observe the CBS peak in the stationary regime [Wiersma 95]. In this regime, the CBS peak results from the sum of all the contributions for all possible diffusion times and has the celebrated cusp predicted in [Akkermans 86]. In our experiments on the other hand, we will be able to follow the time resolved dynamics of the CBS peak in a similar way as the experiments done in acoustics [Bayer 93, Tourin 97] and optics [Vreeker 88].

7.2 The experimental sequence

The experimental scheme is a generalization of the sequence used in the previous chapter on AL (see Sec. 6.3) on the apparatus explained in Ch. 3. It is based on the proposal of Ref. [Cherroret 12] that suggested observing CBS in the momentum space. A cloud of non-interacting ultra-cold atoms is launched with a narrow velocity distribution in an elongated laser speckle disordered potential, leading to quasi two-dimensional scattering (see below). Time of flight imaging, after a propagation time t in the disorder, directly yields the momentum distribution.

In the experiment we use a sample of non-interacting paramagnetic atoms, suspended against gravity by a magnetic gradient (see Sec. 3.4.3), and launched along the y-axis with a very well defined initial momentum $\mathbf{p}_\mathrm{i}$ (see Fig. 7.2). This is realized in the following main steps:

1. Evaporative cooling of an atomic cloud of ^{87}Rb atoms in a quasi-isotropic optical dipole trap (trapping frequency $\simeq 5$ Hz) yields a Bose Einstein condensate of 9×10^4 atoms in the $F=2$, $m_F=-2$ ground sublevel.

2. We suppress the inter-atomic interactions by releasing the atomic cloud and letting it expand during 50 ms. At this stage, the atomic cloud has a size (standard half-width along each direction) of $\Delta r_\mathrm{u} = 30$ μm, and the residual interaction energy ($E_\mathrm{int}/h \sim 1$ Hz) is negligible compared to all relevant energies of the problem.

3. Since the atomic cloud is expanding radially with velocities proportional to the distance from the origin, we can use the "delta-kick cooling" technique [Ammann 97], by switching on a harmonic potential for a well chosen amount of time. We discuss this technique in the next section.

4. We give the atoms a finite momentum $\mathbf{k}_i$ along the z-direction, without changing the momentum spread, by applying an additional magnetic gradient during 12 ms. The first image of Fig. 7.4 shows the resulting 2D momentum distribution. The average velocity is $v_\mathrm{i} = 3.3 \pm 0.2$ mm/s ($k_\mathrm{i} = p_\mathrm{i}/\hbar \simeq 4.5$ μm^{-1}), corresponding to a kinetic energy $E_k/h \simeq 1190$ Hz.

5. To study CBS, we suddenly switch on an elongated optical disordered potential (see below) in less than 0.1 ms, let the atoms scatter for a time t, then switch off the disorder and monitor the momentum distribution at time t.

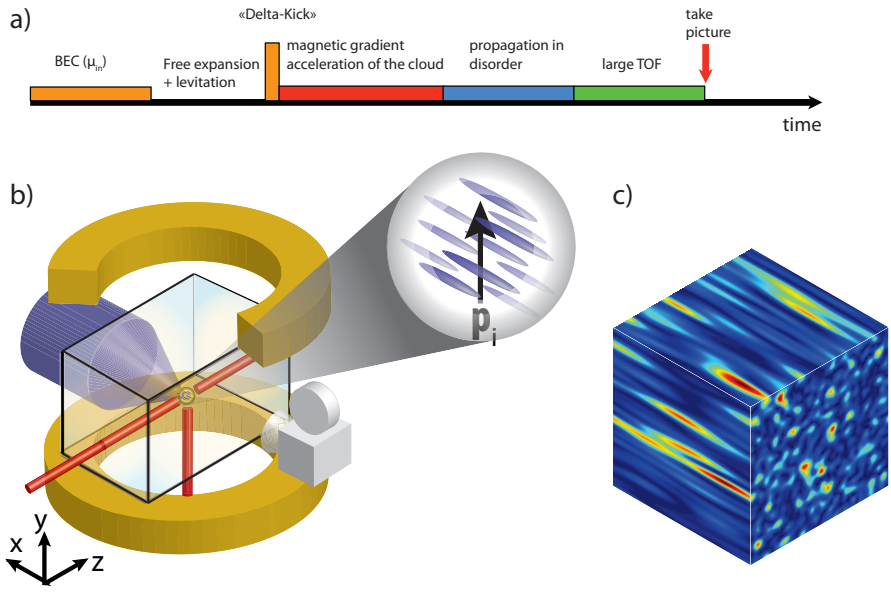

Figure 7.2: **Experimental set-up**. a) Chronogram of the experiment as explained in the text. b) A cloud of ultra-cold atoms, suspended against gravity, is launched with a well defined momentum $\mathbf{p}_\mathrm{i}$ perpendicularly to a disordered potential, which is very elongated in the x-direction. After a diffusion time t, the disorder is switched off, and fluorescence imaging along x, after a long enough time of flight, yields the 2D velocity distribution in the $y-z$ plane. c) False color representation of a realization of the elongated speckle disorder.

6. This momentum distribution is obtained with a standard time of flight technique that converts the velocity distribution into a position distribution (see Sec. 3.1.3). Because of the magnetic levitation, we can let the atomic cloud expand ballistically for as long as 150 ms before performing fluorescence imaging along the x axis. The overall velocity resolution $\Delta v_\mathrm{res} = [\Delta {v_\mathrm{u}}^2 + (\Delta r_\mathrm{u}/t_\mathrm{tof})^2]^{1/2} = 0.23$ mm/s, is nevertheless mainly limited by the initial size Δr_u of the atomic cloud. We will discuss the velocity spread Δv_u in more detail in the next section.

We will now continue with a discussion of the cooling technique and the disorder configuration we have chosen in those experiments.

7.2.1 Delta-kick cooling

As will become obvious in the discussion of our results on the CBS signal, we would like to work with a cloud with a very narrow velocity distribution. To overcome the limits of the evaporation technique (see Sec. 3.4.2.1) we have chosen to apply the so called "delta-kick" cooling technique [Ammann 97]. Its principle can be easily understood by classical considerations.

When the initial trap with trapping frequencies ω_{trap} is switched off the initial interaction energy gets transformed into kinetic energy. After a time $1/\omega_{trap}$ the expansion is free (see Fig. 7.3 a), as long as the influence of the levitation is negligible. After a

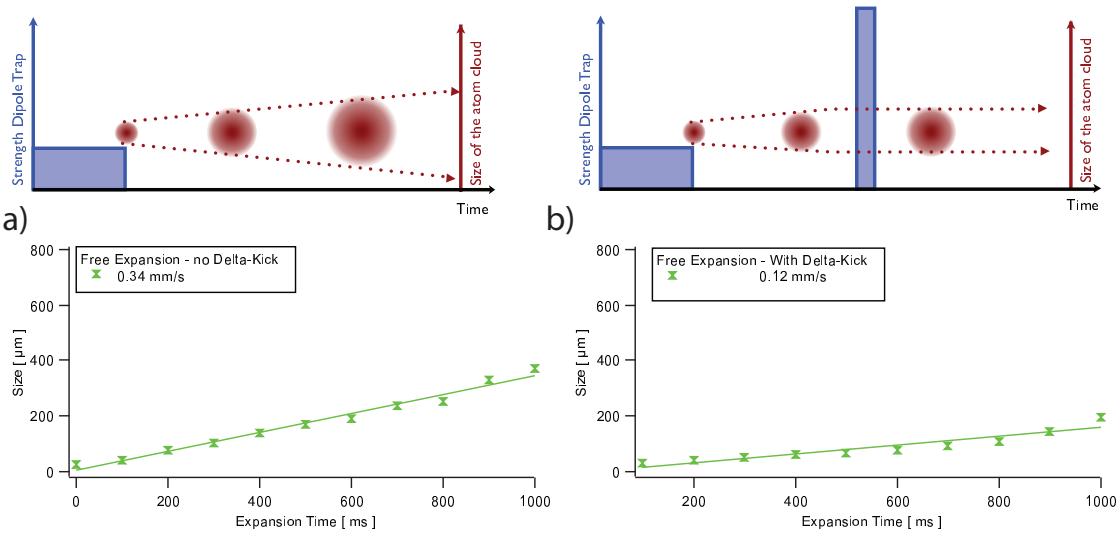

Figure 7.3: **Delta-Kick cooling** a) After switching off the initial trap the atoms expand freely. b) After a time $t_{\rm exp} = 50$ ms we apply again the dipole trap for a time $t_{\rm DK} \approx 0.5$ ms at a trapping frequency $\omega_{\rm DK}/2\pi \approx 29$ Hz. This reduces the velocity spread considerably.

time-of-flight $t_{\rm exp}$ the velocity distribution got transformed into a position distribution $\mathbf{r}_i = \mathbf{v}_i t_{exp}$. At this point we apply a harmonic potential with trapping frequencies $\omega_{\rm DK}$. Actually, we can solve the classical equation of motion and we obtain the velocity in the potential

$$\mathbf{v}(t) = -\mathbf{v}_i t_{exp} \omega_{\rm DK} \sin(\omega_{\rm DK} t) + \mathbf{v}_i \cos(\omega_{\rm DK} t) \ . \tag{7.6}$$

This shows immediately that we can find a time $t_{\rm DK}$, where the motion is frozen out.

$$t_{\rm DK} = \frac{1}{\omega_{\rm DK}} \tan(1/\omega_{\rm DK} t_{exp}) \approx \frac{1}{\omega_{\rm DK}^2 t_{exp}} \text{ for } \omega_{\rm DK} t_{exp} \ll 1 \tag{7.7}$$

We have implemented this technique using our optical dipole trap. After cutting the initial trap, we let the atoms expand for $t_{\rm exp} = 50$ ms. At this point, the velocity distribution got transformed into a position distribution and we can apply the optical dipole trap. The atoms evolve then in the trap with trapping frequency ≈ 29 Hz for ≈ 0.5 ms, verifying well the condition (7.7).This significantly narrows the velocity distribution and the resulting velocity spread $\Delta v_{\rm u} = 0.12 \pm 0.03$ mm/s is just one order of magnitude above the Heisenberg limit ($\Delta r_{\rm u} \cdot m \Delta v_{\rm u} \sim 5\hbar$). In the experiments we are probably limited by the initial size of the cloud, the anharmonicity of the dipole trap and residual roughness of the trapping potential.

7.2.2 The 2D configuration in an elongated disorder

The disordered potential is the dipole potential associated with a laser speckle field (see Ch. 4.1), obtained by passing a laser beam through a rough plate, and focusing it on the atoms (Fig. 7.2). It has an average value $V_{\rm R}$ equal to its standard deviation. In contrast to the experiments performed in the previous chapter we do not superimpose

this speckle field with a second one. Its autocorrelation function is therefore strongly anisotropic, with a transverse shape well represented by a Gaussian of standard half-widths $\sigma_y = \sigma_z = \sigma_\perp \simeq 0.2$ μm, and a longitudinal Lorentzian profile of half-width $\sigma_x \simeq 1$ μm (HWHM) [Piraud 12b]. The laser (wavelength 532 nm) is detuned far off-resonance (wavelength 780 nm), yielding a purely conservative and repulsive potential. The disorder amplitude V_R is homogenous to better than 1% over the atom cloud (profile of half-widths 1.2 mm along y,z, 1 mm along x).

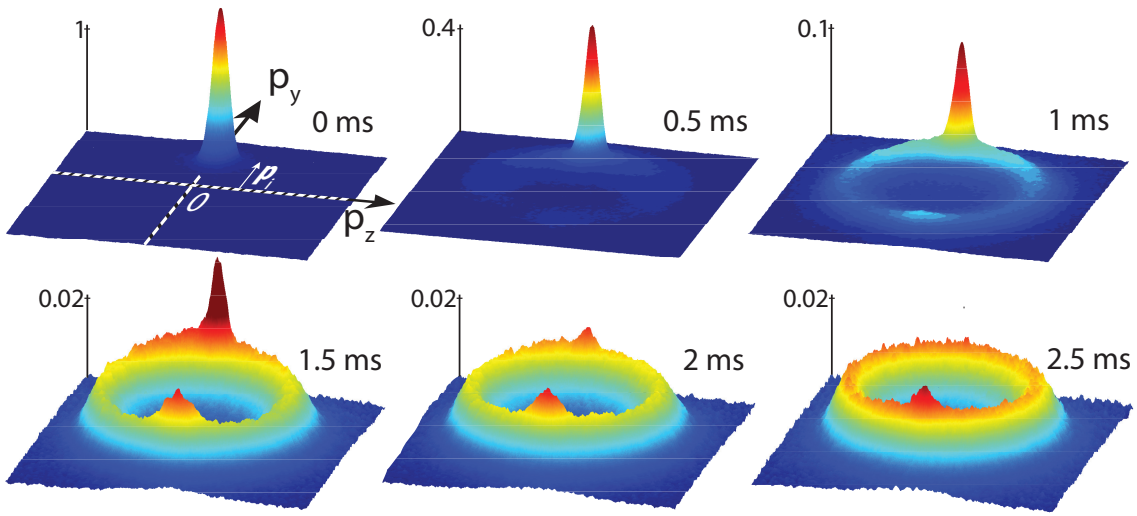

Figure 7.4: **Observed momentum distributions after different propagation times t in the disorder**. The images correspond to an averaging over 20 experimental runs. Note that the scale is different in the three first images (t =0, 0.5, and 1 ms), whereas it is the same in the three last images (t =1.5, 2, and 2.5 ms).

The anisotropy of the speckle pattern (elongated along x with an aspect ratio of 5) allows us to operate in a quasi-2D configuration by launching the atoms perpendicularly to the x-axis. In the transverse y-z plan, the matter wave is scattered by a potential whose spatial fluctuations are shorter than its wavelength, i.e. $k_i\sigma_\perp \simeq 0.9 < 1$. The scattering is therefore isotropic in this plane as discussed in more detail in Sec. 5.4.3. Then the dynamics within this plane develops rapidly, on the typical time scale of a single scattering event.

In contrast, the spatial fluctuations along the x axis are much larger than the wavelength ($k_i\sigma_x \simeq 4.5 > 1$), so that each scattering event is limited to a small angle outside the y-z plane [Kuhn 07, Piraud 12b]. The diffusive dynamics along the longitudinal direction will then take place at a longer time scale. For the short times considered in the following, we will thus neglect the dynamics out of the y-z plane, and consider a pure 2D system in our first analysis.

7.3 Investigations of the momentum distribution

Figure 7.4 shows the time evolution of the momentum distribution for a disorder amplitude $V_R/h = 975 \pm 80$ Hz. As expected for elastic scattering of particles in a conservative

potential, we observe a ring that corresponds to a redistribution of the momentum directions over 2π while the momentum magnitude remains almost constant. The evolution of the initial momentum peak and of the angular ring profile yields the elastic scattering time and the transport time.

The most remarkable feature is the large visibility peak, which builds up in the backward direction. The height and width of that peak, and their evolution with time, are an indisputable signature of CBS, intimately linked to the role of coherence. The incoherent backscattering echo phenomenon reported in the paper by Labeyrie *et al.* [Labeyrie 12], which may hamper the observation of CBS, does not play a role in our case, since the delta kick cooling method that we use suppresses the position-momentum correlation in the atomic sample. Moreover, the large amplitude of our suddenly applied disorder would wash out any residual correlation.

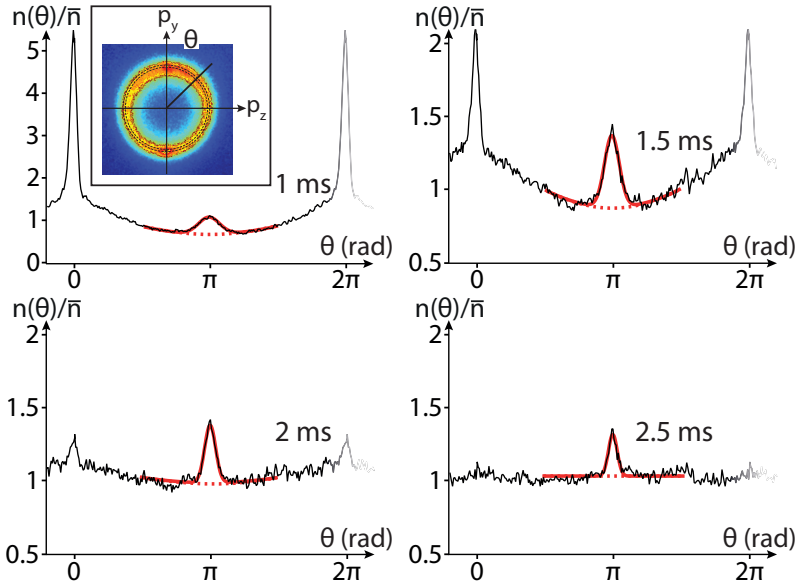

Figure 7.5: Normalized angular profiles $n(\theta, t)/\bar{n}$ corresponding to the distributions shown in Fig. 7.4. The red solid lines correspond to the double structure fit around the backscattering direction [a parabola for the incoherent background (dashed line) and a gaussian for the CBS peak, see text]. Inset: false color representation of the momentum distribution ($t = 2$ ms). The angle θ refers to the scattering direction with respect to the initial direction $\mathbf{k}_i$.

In order to analyze these data quantitatively, we perform a radial integration of the 2D momentum distribution on a thin stripe between $k_\mathrm{i} - \Delta k_\mathrm{res}$ and $k_\mathrm{i} + \Delta k_\mathrm{res}$ (inset of Fig. 7.5) ($\hbar \Delta k_\mathrm{res} = m \Delta v_\mathrm{res}$ is the momentum resolution). This yields the angular profile $n(\theta, t)$, displayed in Fig. 7.5 for increasing diffusion times.

In the following, we extract in a first step the scattering time τ_S and the transport time $\tau^\star$ from the observed momentum profiles. We then turn our attention to the analysis of the CBS peak. Further, we want to note that the experimental results were compared to 2D numerical simulations. Those were performed by Thomas Plisson and are discussed in more detail in his PhD.

7.3.1 The scattering time

First, we extract the elastic scattering time τ_S from the decay of the initial peak. As discussed in Sec. 5.4.1, the scattering time corresponds to the characteristic time of the exponential decay of the initial momentum. Therefore, τ_S can be directly measured in our experiments by the evolution of the number of non-scattered atoms in the initial peak of the momentum distribution by [Cherroret 12]

$$n(\mathbf{k}_i, t) = n_0 e^{-\frac{t}{\tau_S}} \ . \tag{7.8}$$

We have obtained $n(\mathbf{k}_i, t)$ using a heuristic lorentzian fit function, which matches the form of the angular profile rather well (see inset Fig. 7.6). The obtained time evolution, shown in Fig. 7.6, has indeed the predicted exponential decay. We find $\tau_S = 0.33 \pm 0.02$ ms (mean free path $l_s = v_i \tau_S = 1.1$ μm).

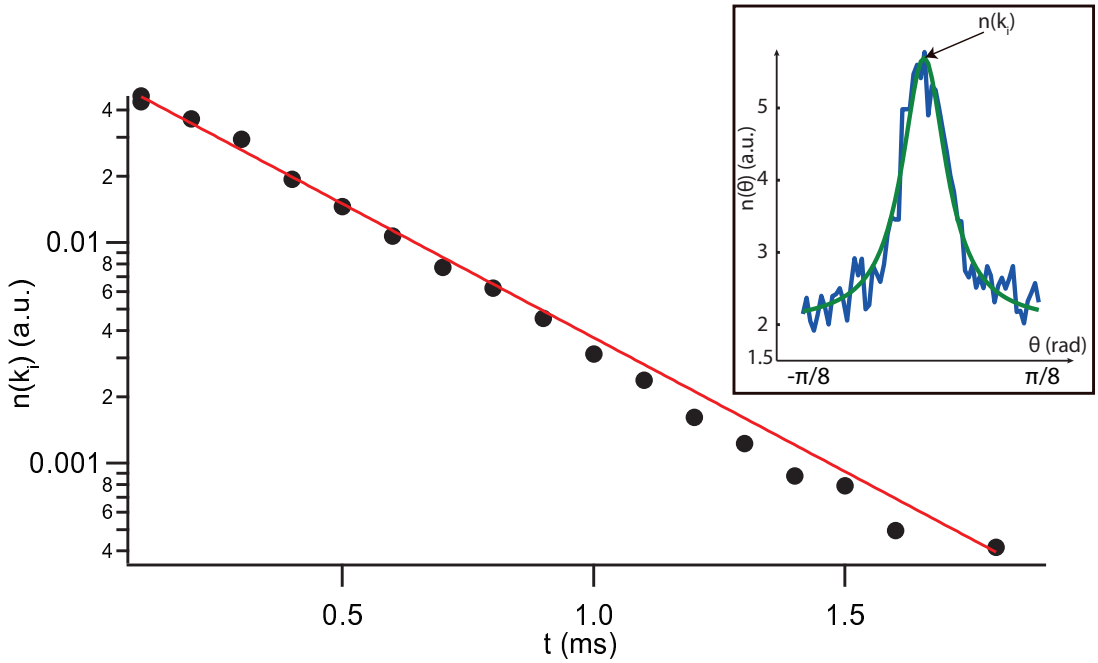

Figure 7.6: **Time evolution of the initial peak**. From the exponential decay of the measured peak height (black dots) we extract the scattering time using an gaussian fit (straight red line). We obtained the height from a gaussian fit including an offset of the angular profile around $\theta = 0$ as shown in the inset.

Note that this quantity also plays a role in the radial width of the ring (inset of Fig. 7.5) which is associated to a Lorentzian energy spread $\Delta E = \hbar/\tau_S$ (HWHM) acquired by the atoms when the disorder is suddenly switched on. Combining the corresponding momentum spread with the resolution of our measurement, we find a width in agreement with the observed ring width. The measured value of τ_S is in accordance with numerical simulations adapted to our configuration, but is about 2 times the value predicted by a perturbative calculation [Piraud 12b]. This is consistent with the fact that we are not fully in the weak disorder regime defined by $\Delta E/E_k = 2/k_i l_s \ll 1$. Here we have $\Delta E/E_k \sim 0.4$ ($k_i l_s \sim 5$).

When approaching the strong disorder regime, the shape of the energy distribution (which is intimately linked to the so-called *spectral functions*, we mentionned in Sec. 5.4.2) departs from a Lorentzian [Yedjour 10]. A detailed analysis of the deviation is an ongoing project.

7.3.2 The transport time

As discussed previously in Sec. 5.4.3, the scattering of the atoms on the speckle grains is not necessarily isotropic. When the typical scattering angle θ_S becomes small, the isotropization of the momentum distribution can take considerably longer than the scattering time. The timescale associated with this isotropization is the important transport time $\tau^\star$, after which, in the absence of coherence, the information about the initial direction would be lost and which is directly linked to the diffusion constant by Eq. (5.7).

In order to calculate the transport time, we decompose the angular profiles shown in Fig. 7.5 in a Fourier series:

$$n(\theta,t) = \sum_{m=0}^{\infty} n_m(t)\cos(m\theta) \tag{7.9}$$

From the exponential decrease of the first Fourier component, we can then extract the transport time (following private communications with Cord A. Müller and [Cherroret 12])

$$n_1(t) = n_1(0)\cdot e^{-t/\tau^\star} \tag{7.10}$$

We find $\tau^\star = 0.4 \pm 0.05$ ms, also in agreement with numerics. Note that $\tau^\star$ takes into account the CBS phenomenon and its calculation must include weak localization corrections. It is only slightly larger than τ_S, as expected for a nearly isotropic scattering probability ($k_\mathrm{i}\sigma_\perp = 0.9$). The transport time sets the time scale of the onset of the diffusive dynamics, which is well established only after several $\tau^\star$. In the experiment, we observe that the momentum distribution has become fully isotropic after $t \sim 2.5$ ms (i.e. $\sim 6\,\tau^\star$), with a steady and flat angular profile of mean value $n(\theta,t) = \bar{n}$, except around $\theta = \pi$ where the CBS peak is still present.

7.3.3 Analysis of the CBS peak

To analyze the evolution of the CBS signal, we fit (see Fig. 7.5) the angular profiles by the function

$$n(\theta) = n_\mathrm{incoh}(\theta,t) + n_\mathrm{coh}(t)\exp[-(\theta-\pi)^2/2\Delta\theta(t)^2]\ , \tag{7.11}$$

where we assume that $n_\mathrm{incoh}(\theta,t)$ has a parabola shape around $\theta = \pi$. This allows us to measure the contrast $\mathcal{C}(t) = n_\mathrm{coh}(t)/n_\mathrm{incoh}(\pi,t)$ and the width $\Delta\theta(t)$ of the CBS peak. Their evolutions are shown in Fig. 7.7. A CBS peak appears as soon as scattering in the backward direction is significant, but the contrast starts decreasing before reaching the ideal value of 1. For the width, we observe the predicted monotonous decrease, but it tends asymptotically towards a non null value rather than zero.

To compare these observations with theoretical predictions, we must take into account our finite resolution. The black line in figure 7.7(b) represents the calculated CBS width that results from the convolution of our resolution $\Delta\theta_\mathrm{res} = \Delta k_\mathrm{res}/k_\mathrm{i} = 0.07$ with the expected CBS width $\Delta\theta_\mathrm{CBS} = \Delta k_{\mathrm{CBS},\alpha}/k_\mathrm{i} = 1/k_\mathrm{i}\sqrt{2Dt}$ in the diffusive regime (the widths

are added quadratically). The diffusion constant is evaluated using the standard relation $D = v_i^2\tau^\star/2$, so that the solid line does not involve any adjustable parameter. We see that the agreement with the data is good when we enter the multiple scattering regime (for $t \gtrsim 1.5$ ms in Fig. 7.7(b)), but not at short times.

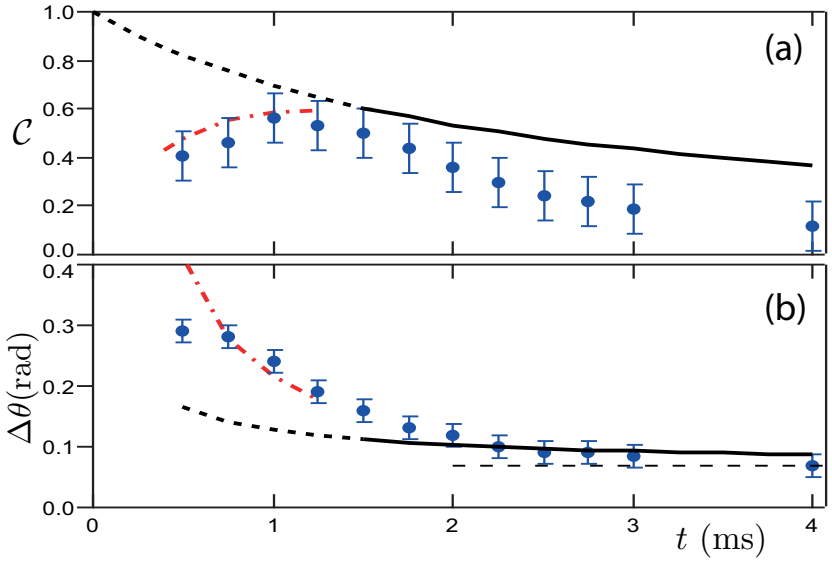

Figure 7.7: **Time resolved dynamics of the CBS peak**: evolution of the contrast $\mathcal{C}$ (a) and the width $\Delta\theta$ (b) versus the scattering time t. The blue points are experimental datas, the solid and dashed black lines are the theoretical predictions for the multiple scattering regime at long times ($t \gtrsim 4\tau^\star$; $\tau^\star = 0.4$ ms). The dashed and dotted red lines corresponds to the calculation of [Gorodnichev 94] at short times (i.e. for $t \sim \tau_S$; $\tau_S = 0.33$ ms), where single scattering events cannot be neglected.

The broadening of the CBS peak by the finite resolution is also responsible for a decrease of the contrast, as represented in Fig. 7.7(a). Here also, we observe that the prediction (which again involves no adjustable parameter) is very different from the observed values at short times, but is in reasonable agreement with the measurements around $t \sim 1.5$ ms. On the other hand, the measured contrast is definitely smaller than the theoretical prediction when t increases yet more. We relate this observation at long times to the onset of the dynamics in the third direction x. Using a second imaging system yielding the momentum distribution in the $x - y$ plane (see Fig. 7.8), we estimate a typical time of 4 ms for this out-of-plane dynamics to become significant, and render the 2D approach invalid.

Deviations at short time were to be expected. Indeed, CBS demands multiple scattering, or at least double scattering, to happen (see inset of Fig. 6.5), whereas single scattering events do not participate to the CBS peak. At short times ($t \sim \tau_S$), the contribution of single scattering to backscattering is not negligible compared to multiple scattering. This entails a reduction of the contrast (see e.g. [Tsang 84]), and a modification of the shape (no longer Gaussian), whose width decreases at this stage as $1/t$

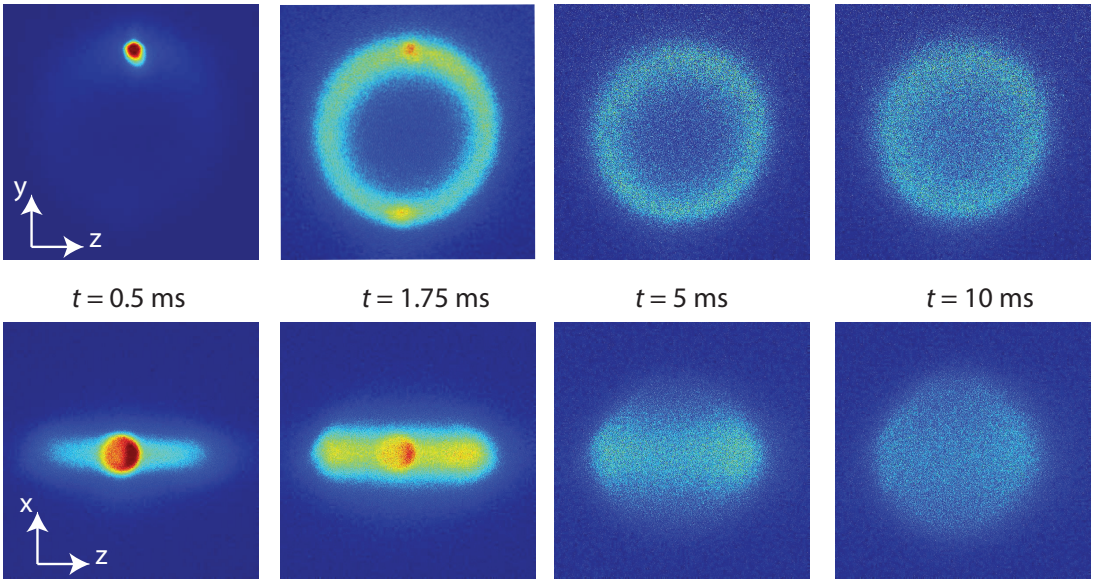

Figure 7.8: **2D-3D crossover**: False color graphs of the momentum distribution for different propagation times. In the upper row we show the evolution in the $y-z$ plane, which is the basis of our discussion in the text. In the bottom row, we show the evolution in the $x-y$ plane using a second imaging system. The initial peak is blurred as it is out of focus of the system. On sees nicely that the scattering out of the initial $y-z$ plane becomes important only after ~ 5 ms.

(ballistic motion between the first two scatterers). In the case of light, a calculation for isotropic scattering [Gorodnichev 94] predicts a short time evolution of the contrast $\mathcal{C} = (2t/\pi\tau_S)/(1+2t/\pi\tau_S)$ and width $\Delta\theta_{\mathrm{CBS}} \sim 3/k_\mathrm{i}l_\mathrm{s}(\tau_S/t)$. This prediction is plotted in Fig. 7.7 and is found in fair agreement with the observations in this time domain. Finally, note that the width around $t \sim \tau_S$ is linked to disorder strength quantified by $k_\mathrm{i}l_\mathrm{s}$. Here we find a maximum value of $\Delta\theta_{\mathrm{max}} \sim 0.3$ rad, that is $\Delta\theta_{\mathrm{max}} \sim 1.5/k_\mathrm{i}l_\mathrm{s}$ ($k_\mathrm{i}l_\mathrm{s} \sim 5$, see above).

7.4 Dependence on the microscopic properties

As mentioned before, it is straightforward in our experiments to vary the disorder strength V_R and the mean kinetic energy of the atoms E_k. This allowed us to compare the dependance of the scattering time, the transport time and the CBS signal on those parameters systematically. In this section, we present preliminary results on the investigation of those dependencies.

7.4.1 The scattering time

The scattering of the atoms in the disordered potential induces an energy spread of the initial state of $\Delta E = \hbar/\tau_S$ (see Sec. 5.4.2). As this energy spread gets larger we approach the strong disorder regime, where theories are still subject to debate. Monitoring the scat-

tering time for different disorder strengths is therefore a great opportunity to investigate the crossover from the weak disorder to the strong disorder limit. In the weak disorder regime, where the Born approximation holds, the dependance of the scattering time takes the simple form (see Sec. 5.4.1)

$$\tau_S(V_R, E_k, E_R) = (E_R/V_R)^2 \cdot f(E_k/E_R) \cdot \tau_R \ , \tag{7.12}$$

where $\tau_R = \hbar/E_R$ is the time scale associated with the correlation energy. $f(E_k/E_R)$ is a dimensionless function which depends on the microscopic details of the disorder and can be calculated within the Green function formalism [Rammer 04]. For the case of the anisotropic speckle disorder, that we use in our experiments, Marie Piraud from the theory team of our group, led by Laurent Sanchez-Palencia, calculated the function $f(E_k/E_R)$ in a wide regime of parameters (see PhD by Marie Piraud).

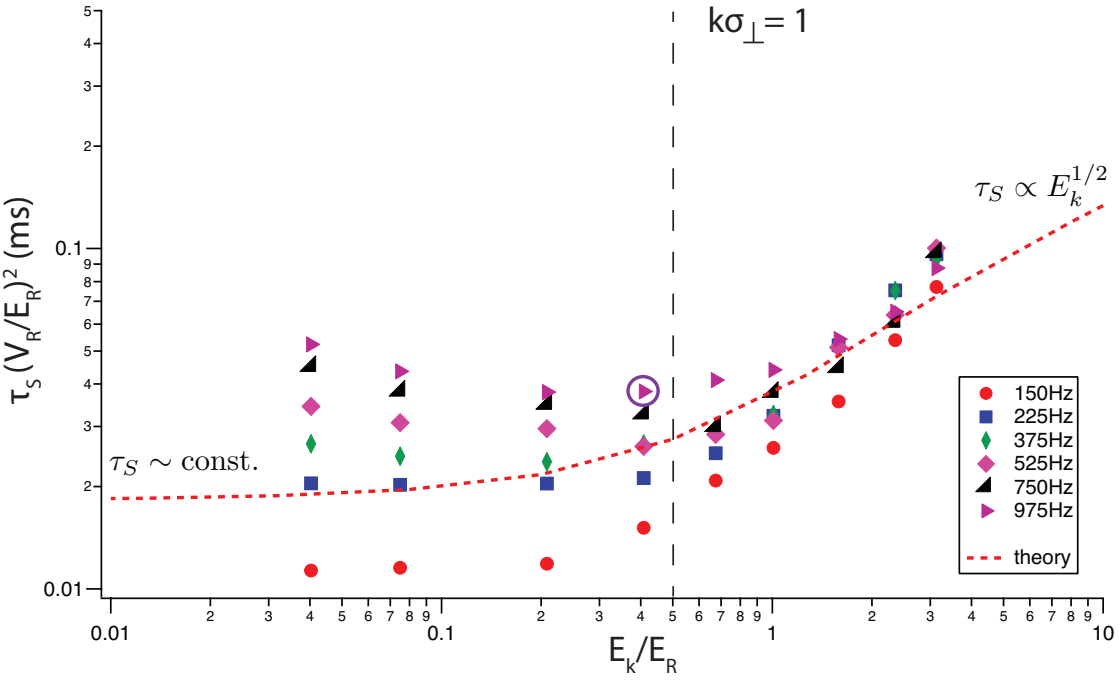

Figure 7.9: **Energy dependent scattering time**. The colored lines correspond to the experimentally observed scattering times, which where renormalized as discussed in the text. The dashed red line represents the theoretical predictions. The encircled point corresponds to the configuration we discussed in section 7.3.

We have tested relation (7.12) by measuring the scattering time, as explained in Sec. 7.3.1, for different kinetic energies and disorder strengths. In Fig. 7.9 we present the measured scattering times rescaled by $(V_R/E_R)^2$. Varying the kinetic energy at fixed disorder amplitude, we can therefore test the predicted dependance $f(E_k/E_R)$. The obtained values are compatible with the theoretical predicition (red dashed line) especially for low disorder amplitudes ($V_R/h \leq 375$ Hz). Note that the form of the experimental curves depends heavily on the precise calibration of the disorder amplitude V_R and the kinetic energy E_k, which makes the following discussions very sensible to possible experimental uncertainties.

For very low energies, the scattering time is predicted to be independent of the kinetic energy of the atoms. This is compatible with our observations. For energies larger than the correlation energy the scattering gets weaker with increasing energy. This can be explained by the fact that the scattering has to fulfill the Bragg condition $|\mathbf{k}_i - \mathbf{k}_f| \leq 2/\sigma_R \sin(\theta_S/2)$ in first order. As the energy increases the condition is more and more restrictive and the scattering is weakened. To be precise, the scattering time is predicted to scale with $\tau_S \propto E_k^{1/2}$ for energies much larger than the correlation length (see Sec. 5.4.1). It would be tempting to observe this dependance by increasing the kinetic energy of the atoms further.

As we increase the disorder amplitude ($V_R/h \geq 525$ Hz), systematic deviations from the theoretical predictions for low kinetic energies are observed. We see this as a clear sign that we reached the strong disorder limit, where the weak disorder development (7.12) breaks down and the V_R^2 scaling is no longer followed. Those experiments might allow to test theories making predictions about the scattering time that go beyond the Born approximation. This work has to be left to the future.

7.4.2 The transport time

The scattering time allows us to differentiate between strong and weak disorder, but the propagation of the atoms is characterized by the transport time $\tau^\star$. A detailed investigation of this transport time for different configurations allows us therefore to approach a more quantitative understanding of the strong disorder regime. In the same way as the scattering time, we can describe the dependance of the transport time in the weak disorder limit by (see Sec. 5.4.3)

$$\tau^\star(V_R, E_k, E_R) = (V_R/E_R)^2 \cdot g(E_k/E_R) \cdot \tau_R \ , \tag{7.13}$$

where $g(E_k/E_R)$ is a another function depending on the microscopic details of the disorder. To test this relation (7.13) we measured the transport time, as explained in Sec. 7.3.2, for different kinetic energies and disorder strengths. At sufficiently low energies the scattering is expected to be isotropic and the transport time should be in the order of the scattering time. This is indeed what we observed in the experiments. As mentioned above, for high energy $E_k \gg E_R$ the scattering is restricted to the forward direction and it takes therefore several scattering events to completely randomize the motion of the atoms. This leads to the observed fast increase of the transport time for high energies.

To go further, we can attempt to compare the measured transport times with theoretical predictions in the weak disorder limit done by Marie Piraud *et al.* [Piraud 12b]. She calculated the diffusion constants in the case of our disorder configuration . We related the results of those calculations to the transport time by $D = 2E_k\tau^\star/d$, where $d = 3$ is the dimension of the system. The resulting predicition (red dashed line), which is valid in the weak disorder regime, is in reasonable agreement with obtained experimental results. In contrast to the scattering time the transport time is predicted to increase with $\tau^\star \propto E^{3/2}$. We extracted experimentally an increase with $\tau^\star \propto E^{1.5\pm0.15}$ from a fit of the experimental datas with a power law. This is in nice agreement with the theory and the deviation of the experiments to the theoretical predictions might be due to problems in the calibration of the energy of the atoms.

Again we observe that the scaling with V_R^2 is not valid at weak energies, indicating that we operate in a rather strong disorder, where the Born approximation is not valid.

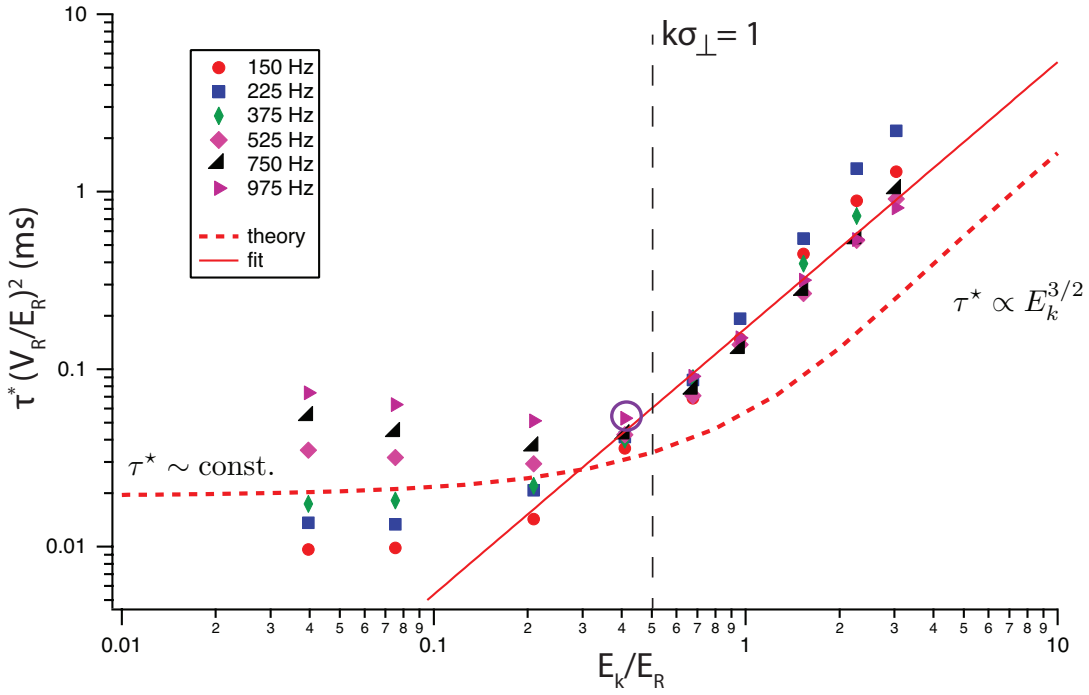

Figure 7.10: **Energy dependent transport time**. The colored lines correspond to the experimentally observed transport times, which where renormalized as discussed in the text. The dashed red line represents the theoretical predictions. Note the strong increase of the transport times for $k\sigma_\perp > 1$. We fitted the obtained experimental datas in this region by a power law $A \cdot (E_k/E_R)^\alpha$. This yields $\alpha = 1.5 \pm 0.15$. The encircled point corresponds to the configuration we discussed in section 7.3.

A detailed investigation of this regime is highly challenging as perturbation theory breaks down at this point. This study is an ongoing project.

7.4.3 The CBS signal

Finally we studied the dependence of the CBS as described in Sec. 7.3.3 for different disorder amplitudes and kinetic energies (see Fig. 7.11). Note that we did this treatment only on data sets, where the CBS signal was clearly visible and that we have therefore less configurations to compare than in the previous two sections. For the treated data we have found a similar agreement between data and theory.

In contrast to the observed moderate changes in the maximum peak contrast ($\mathcal{C}_{\max} \sim 0.5 - 0.7$), the maximum peak width $\Delta\theta_{\max}$ increases significantly with the amplitude of the disorder and the inverse of k_i. The highest observed width of ~ 1.2 rad (from which we infer $k_i l_s \sim 1.3$) suggests that we are close to the strong disorder regime, where AL is expected to be experimentally observable in 2D systems. Such an observation, however, would demand a longer 2D evolution in the disorder, which is limited in the present experiment because of the cross over to the 3D regime. Increasing this time, as for instance in [Robert-de Saint-Vincent 10], will then constitute the next step towards AL, with the possibility to observe the coherent forward scattering peak predicted in [Karpiuk 12].

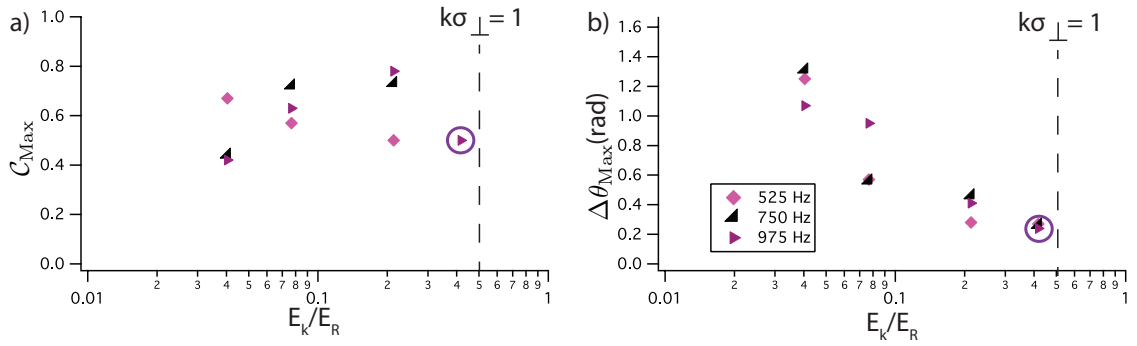

Figure 7.11: **Energy dependent CBS signal**. a) The maximum contrast of the CBS signal b) The maximum width of the CBS signal. The encircled points correspond to the configuration we discussed in section 7.3.

7.5 Conclusions

In conclusion, we have demonstrated experimentally that the time resolved study of the momentum distribution of ultra-cold atoms in a random potential is a powerful tool to study quantum transport properties in disordered media. We have been able to extract the elastic scattering time, the transport time, and to observe the CBS peak. Let us emphasize that the theoretical analysis as well as numerical simulations render an account of the observations not only in the multiple scattering regime but also at short time, during the onset of multiple scattering. Such agreement gives a strong evidence of the fundamental role of coherence in that phenomenon. Further evidences of the role of coherence could be seeked in the predicted suppression of the CBS peak [Golubentsev 84], when scrambling the disorder, or when dephasing the counter-propagating multiple scattering paths using artificial gauge fields [Lin 09], in the spirit of pioneering works in condensed matter physics [Bergmann 84] or optics [Lenke 00]. Finally, this work also opens promising prospects to study the effect of interactions on CBS (see e.g. [Agranovich 91, Hartung 08]).

CHAPTER 8

Conclusion

In this manuscript we have presented our work on the quantum transport of matter waves in a speckle disorder. In particular we have shown evidence for Anderson localization in three dimensions and we reported the direct observation of coherent backscattering of ultracold atoms.

We pointed out how we transposed the successful scheme that allowed for the observation of one-dimensional Anderson Localization to the three dimensional case. Then, we detailed our expansion experiments, where we monitored the three-dimensional expansion of an initial BEC in the presence of a quasi-isotropic laser speckle disorder. We observed an atomic cloud composed of two components: a localized and a diffusive part. These components respectively correspond to energy levels below and above the mobility edge. In those experiments it has not been possible to reach a regime where all the atoms were localized, because of the wide energy distribution of the atoms induced by the disorder. Nevertheless, the existence of a localized fraction is beyond any reasonable doubt. Altogether, those experiments allowed us to report the first evidence of 3D Anderson Localization of ultracold atoms in the presence of a well-controlled optical disorder. This marks a first step towards the precise investigation of the critical behavior around the mobility edge with ultracold atoms.

It is now left to future efforts to achieve a better control and detection of the energy distribution. Further work can be inspired by the experiments on the one-particle excitation spectrum of a strongly interaction Fermi gas by the Jin Group [Stewart 08], which was more recently also applied to the study of the Mott insulator using Bragg diffraction [Clément 09].

Further, we have demonstrated experimentally that the time resolved study of the momentum distribution of ultra-cold atoms in a random potential is a powerful tool to study quantum transport properties in disordered media. We have been able to extract the elastic scattering time, the transport time, and to observe the CBS peak. All the experimental observations were compatible with numerical simulations and microscopic theories without any free parameters. Such studies on the role of coherence could be taken further by scrambling the disorder, which is predicted to lead to asuppression of the CBS peak [Golubentsev 84], or by dephasing the counter-propagating multiple scattering paths using artificial gauge fields [Lin 09]. The most exciting opportunities seems to be the investigation of the very recently predicted Coherent Forward Scattering phenomena, which should be closely linked to Anderson Localization [Karpiuk 12]. An observation of this new phenomena would provide a new tool to study the role of interference played in the strong disorder regime.

Those investigations promise to give deeper insight into the problem of 3D Anderson Localization. This refined understanding of 3D Anderson Localization will help to test possible, microscopic theories of 3D Anderson Localization. A quantitative agreement of

the experimental observations with a microscopic theory is a still-standing goal even after more than 50 years of research on the subject. I am very hopeful that this agreement will be reached in a near future and wish the people who continue to work on it all the best luck...

Appendix A

Atom losses during the expansion in the disorder

In this appendix we discuss the different homogeneous and inhomogeneous atom losses, which occur during the expansion of the atoms in the disorder.

In a first step, we measured the lifetime of the atoms in the trap with the disorder switched on. The decrease of in the trap is well describe by an exponential decay with time constant $\tau \sim 6.2$ s. This lifetime is considerably smaller than the lifetime in the trap of > 10 s when no disorder is applied. So the lifetime in the trap with the disorder applied cannot be explained by collisions with the background gas. We further verified that sponeous emission and three-body losses can also be excluded. Up to now, we do not no the origin of the losses in the trap, but we speculate that it might be related to the spatial modulation of the applied disorder.

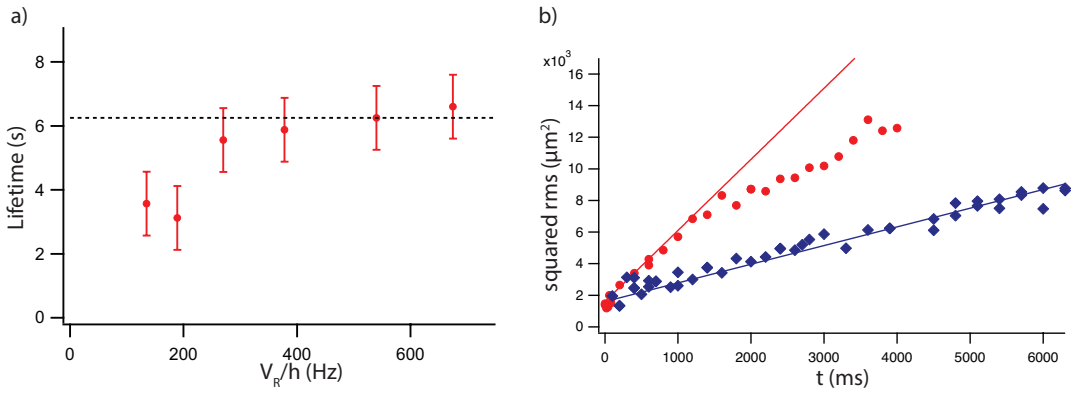

Figure A.1: **Atom losses in the disorder.** a) Lifetime at different disorder strengths. The black dashed line marks the lifetime in the trap with a disorder applied. In a weak disorder the lifetime drops. We explain this with the expulsion of the atoms at the outer part of the cloud. b) rms evolution of the cloud. In a weak disorder (red dots), $V_R/h = 270$ Hz) the variance does no more increase linearly with time. We see this an indication that the atoms explore large distances inhomogeneous losses occur. In a strong disorder (blue squares), $V_R = 680$ Hz, the variance increases linearly over the whole $6s$ of observation time.

However, knowing the lifetime in the trap, we can compare it to the lifetime of the cloud during the expansion in the disorder (see Fig. A.1 a). In a strong disorder,$V_R/h > 400$ Hz the observed lifetimes are consistent with the lifetime, while keeping the atoms trapped (black dashed line). This indicates that the decay is homogeneous. Therefore, we can

compensate these homogeneous losses in the quantitative analysis, performed in section 6.3 , by a simple rescaling to a fixed atom number.

For weak disorder amplitudes on the other hand, $V_R/h < 400$ Hz, the observed lifetime drops below the one measured within the trap. We attribute this decrease to inhomogeneous losses, which are due to the expulsion of the magnetic levitation. The expansion experiments were only made possible by the magnetic levitation, which compensates gravity leaving a harmonic residual potential $V_{res} = -\frac{m\omega^2}{2}r^2$, where r is the distance from the center of the levitation and $\omega/2\pi = 0.35$ Hz (see Sec. 3.4.3). The influence of the levitation can be neglected as long as the acquired potential energy due to the expulsion is smaller than the chemical potential, i.e. for distances $\lesssim 100$ μm for our experimental parameters. Such a large extension of the cloud is only reached in a weak disorder regime. As the atoms diffusive away from the cloud, the expulsion accelerates the atoms at the outer part of the cloud which get therefore rapidly lost. This mechanism can be observed on the time evolution of the rms in a weak disorder as shown in Fig. A.1 a). For short times the evolution is diffusive as discussed in Sec. 6.3.4 . At long times the atoms at the outer part of the cloud are lost and the rms gets saturated. In the strong disorder we did not observe such a marked change in the slope variance.

We therefore concluded, that the levitation induces inhomogeneous losses for weak disorder amplitudes, which cannot be taken into account by a simple rescaling to a fixed atom number. This renders our treatment of the expansions to simplistic in such a weak disorder configuration with $V_R/h < 400$ Hz.

Appendix B

Publications

- A. Bernard, W. Guerin, J. Billy, F. Jendrzejewski, P. Cheinet, A. Aspect, V. Josse & P. Bouyer: *Quasi-continuous horizontally guided atom laser: coupling spectrum and flux limits*, New Journal of Physics **13**, 065015 (2011).
- F. Jendrzejewski, A. Bernard, K. Müller, P. Cheinet, V. Josse, M. Piraud, L. Pezzé, L. Sanchez-Palencia, A. Aspect & P. Bouyer: *Three-dimensional localization of ultracold atoms in an optical disordered potential*, Nature Physics **8**, 398 (2012).
- F. Jendrzejewski, K. Müller, J. Richard, A. Date, T. Plisson, P. Bouyer, A. Aspect & V. Josse: *Coherent Backscattering of Ultracold Atoms*, Physical Review Letters **109**, 195302 (2012). .

Bibliography

[Abrahams 79] E. Abrahams, P. W. Anderson, D. C. Licciardello & T.V. V. Ramakrishnan. *Scaling Theory of Localization: Absence of Quantum Diffusion in Two Dimensions*. Physical Review Letters, vol. 42, no. 10, page 673, 1979.

[Abrikosov 94] A. A. Abrikosov. *Anderson localization in strongly anisotropic metals*. Physical Review B, vol. 50, no. 3, page 1415, 1994.

[Agranovich 91] V. M. Agranovich & V. E. Kravtsov. *Nonlinear backscattering from opaque media*. Physical Review B, vol. 43, no. 16, page 13691, 1991.

[Aharonov 59] Y. Aharonov & D. Bohm. *Significance of electromagnetic potentials in the quantum theory*. Physical Review, vol. 115, no. 3, page 485, 1959.

[Akkermans 86] Eric Akkermans, P.E. E. Wolf & R. Maynard. *Coherent Backscattering of Light by Disordered Media: Analysis of the Peak Line Shape*. Physical Review letters, vol. 56, no. 14, page 1471, 1986.

[Akkermans 07] Eric Akkermans & Gilles Montambaux. Mesoscopic physics of electrons and photons. Cambridge Univ Pr, 2007.

[Allard 12] B. Allard, T. Plisson, M. Holzmann, G. Salomon, A. Aspect, P. Bouyer & T. Bourdel. *Effect of disorder close to the superfluid transition in a two-dimensional Bose gas*. Physical Review A, vol. 85, no. 3, page 033602, March 2012.

[Altshuler 82] B. L. Altshuler, A. G. Aronov, D. E. Khmelnistkii & A. I. Larkin. Coherent effects in disordered conductors, page 130. Mir, Moscow, 1982.

[Ammann 97] Hubert Ammann & Nelson Christensen. *Delta kick cooling: a new method for cooling atoms*. Physical Review Letters, vol. 78, no. 11, page 2088, 1997.

[Anderson 58] P. W. Anderson. *Abscence of Diffusion in Certain Random Lattices*. Physical Review, vol. 109, no. 5, page 1492, 1958.

[Anderson 95] M. H. Anderson, J. R. Ensher, M. R. Matthews, C. E. Wieman & E. A. Cornell. *Observation of Bose-Einstein Condensatin in a Dilute Atomic Vapor.* Science, vol. 269, no. 5221, page 198, 1995.

[Anderson 10] P. W. Anderson, D. J. Thouless, T. V. Ramakrishnan, Peter Wölfle, Dieter Vollhardt, K. B. Efetov & Sudip Chakravarty. 50 Years of Anderson Localization. World Scientific, 2010.

[Aspect 09] Alain Aspect & Massimo Inguscio. *Anderson localization of ultracold atoms.* Physics Today, vol. 62, no. August, page 30, 2009.

[Barabanenkov 73] Yu. N Barabanenkov. *Wave Corrections to the Transfer Equation for Backscattering.* Radiophysics and Quantum Electronics, vol. 1, page 65, 1973.

[Barankov 08] Roman Barankov & Anatoli Polkovnikov. *Optimal Nonlinear Passage Through a Quantum Critical Point.* Physical Review Letters, vol. 101, no. August, page 076801, 2008.

[Barrett 01] M. Barrett, J. Sauer & M. Chapman. *All-Optical Formation of an Atomic Bose-Einstein Condensate.* Physical Review Letters, vol. 87, no. 1, page 010404, June 2001.

[Bayer 93] G. Bayer & T. Niederdränk. *Weak Localization of Acoutic Waves in Strongly Scattering Media.* Physical Review letters, vol. 70, no. 25, page 3884, 1993.

[Beaufils 08] Q. Beaufils, R. Chicireanu, T. Zanon, B. Laburthe-Tolra, E. Maréchal, L. Vernac, J.-C. Keller & O. Gorceix. *All-optical production of chromium Bose-Einstein condensates.* Physical Review A, vol. 77, no. 6, page 061601(R), June 2008.

[Beeler 12] M. C. Beeler, M. E. W. Reed, T. Hong & S. L. Rolston. *Disorder-driven loss of phase coherence in a quasi-2D cold atom system.* New Journal of Physics, vol. 14, no. 7, page 073024, July 2012.

[Bergmann 84] Gerd Bergmann. *Weak localization in thin films: a time-of-flight experiment with conduction electrons.* Physics Reports, vol. 107, no. 1, page 1, 1984.

[Bernard 10] Alain Bernard. *Quantum transport of ultracold atomic matterwaves: Anderson localization and guided atom laser.* PhD thesis, Université Pierre et Marie Curie - Paris VI, 2010.

[Bernard 11] Alain Bernard, William Guerin, Juliette Billy, Fred Jendrzejewski, Patrick Cheinet, Alain Aspect, Vincent Josse & Philippe Bouyer. *Quasi-continuous horizontally guided*

atom laser: coupling spectrum and flux limits. New Journal of Physics, vol. 13, no. 6, page 065015, June 2011.

[Billy 08] Juliette Billy, Vincent Josse, Zhanchun Zuo, Alain Bernard, Ben Hambrecht, Pierre Lugan, David Clément, Laurent Sanchez-Palencia, Philippe Bouyer & Alain Aspect. *Direct observation of Anderson localization of matter waves in a controlled disorder.* Nature, vol. 453, no. 7197, page 891, June 2008.

[Bishop 80] D. J. Bishop, D. C. Tsui & R.C. Dynes. *Nonmetallic Conduction in Electron Inversion Layers at Low Temperatures.* Physical Review Letters, vol. 44, no. 17, page 1153, 1980.

[Bloch 08] Immanuel Bloch, Jean Dalibard & Wilhelm Zwerger. *Many-body physics with ultracold gases.* Reviews of Modern Physics, vol. 80, no. 3, page 885, July 2008.

[Bourdel 04] T. Bourdel, L. Khaykovich, J. Cubizolles, J. Zhang, F. Chevy, M. Teichmann, L. Tarruell, S. Kokkelmans & C. Salomon. *Experimental Study of the BEC-BCS Crossover Region in Lithium 6.* Physical Review Letters, vol. 93, no. 5, page 050401, July 2004.

[Brantut 09] Jean-Philippe Brantut. *Manipulation d'atomes froids dans des potentiels lumineux.* PhD thesis, Université Paris XI, 2009.

[Breit 31] G. Breit & I. I. Rabi. *Mesurement of Nuclear Spin.* Physical Review, vol. 38, no. 11, page 2082, 1931.

[Buggle 04] C. Buggle, J. Léonard, W. von Klitzing & J. Walraven. *Interferometric Determination of the s and d-Wave Scattering Amplitudes in Rb87.* Physical Review Letters, vol. 93, no. 17, page 173202, October 2004.

[Burmistrov 12] I. Burmistrov, I. Gornyi & A. Mirlin. *Enhancement of the Critical Temperature of Superconductors by Anderson Localization.* Physical Review Letters, vol. 108, no. 1, page 017002, January 2012.

[Casati 89] G. Casati, I. Guarneri & D. L. Shepelyansky. *Anderson Transition in a One-Dimensional System with Thre Incommensurate Frequencies.* Physical Review Letters, vol. 62, no. 4, page 345, 1989.

[Castin 96] Yvan Castin & R. Dum. *Bose-Einstein Condensates in Time Dependent Traps.* Physical Review Letters, vol. 77, no. 27, page 5315, 1996.

[Castin 01] Yvan Castin. *Bose-Einstein Condensates in Atomic Gases: Simple Theoretical Results*. In R Kaiser, C Westbrook & F David, editeurs, Coherent atomic matter waves, volume 72 of *Les Houches*, page 1. Springer Berlin / Heidelberg, 2001.

[Chabanov 00] A. A. Chabanov, M. Stoytchev & A. Z. Genack. *Statistical signatures of photon localization*. Nature, vol. 404, no. 6780, page 850, April 2000.

[Chabanov 03] A. A. Chabanov, Z. Zhang & A. Genack. *Breakdown of Diffusion in Dynamics of Extended Waves in Mesoscopic Media*. Physical Review Letters, vol. 90, no. 20, page 203903, May 2003.

[Chabé 08] Julien Chabé, Gabriel Lemarié, Benoît Grémaud, Dominique Delande, Pascal Szriftgiser & Jean Garreau. *Experimental Observation of the Anderson Metal-Insulator Transition with Atomic Matter Waves*. Physical Review Letters, vol. 101, no. 25, page 255702, December 2008.

[Cherroret 12] Nicolas Cherroret, Tomasz Karpiuk, Cord A Müller, Benoît Grémaud & Christian Miniatura. *Coherent backscattering of ultracold matter waves: Momentum space signatures*. Physical Review A, vol. 85, no. 1, page 011604(R), January 2012.

[Chikkatur 00] A. Chikkatur, A. Görlitz, D. M. Stamper-Kurn, S. Inouye, S. Gupta & W. Ketterle. *Suppression and enhancement of impurity scattering in a Bose-Einstein condensate*. Physical review letters, vol. 85, no. 3, page 483, July 2000.

[Chin 10] Cheng Chin, Paul Julienne & Eite Tiesinga. *Feshbach resonances in ultracold gases*. Reviews of Modern Physics, vol. 82, no. 2, page 1225, April 2010.

[Chu 98] Steven Chu. *The manipulation of neutral particles*. Reviews of Modern Physics, vol. 70, no. 3, page 685, 1998.

[Clément 05] D. Clément, A. Varón, M. Hugbart, J. A. Retter, P. Bouyer, L. Sanchez-Palencia, D. M. Gangardt, G. V. Shlyapnikov & A. Aspect. *Suppression of Transport of an Interacting Elongated Bose-Einstein Condensate in a Random Potential*. Physical Review Letters, vol. 95, no. 17, page 170409, October 2005.

[Clément 06] D. Clément, A. F. Varón, J. A. Retter, L. Sanchez-Palencia, A. Aspect & P. Bouyer. *Experimental study of the transport of coherent interacting matter-waves in a 1D random potential induced by laser speckle*. New Journal of Physics, vol. 8, no. 8, page 165, August 2006.

[Clément 09] David Clément, N. Fabbri, L. Fallani, C. Fort & M. Inguscio. *Multi-band spectroscopy of inhomogeneous Mott-insulator states of ultracold bosons*. New Journal of Physics, vol. 11, no. 10, page 103030, October 2009.

[Cohen-Tannoudji 98a] C. Cohen-Tannoudji. *Manipulating atoms with photons*. Reviews of Modern Physics, vol. 70, no. 3, page 707, 1998.

[Cohen-Tannoudji 98b] C Cohen-Tannoudji, J DuPont-Roc & G Grynberg. Atom-Photon Interactions: Basic Processes and Applications. Wiley Science Paperback Series. Wiley, 1998.

[Cornell 02] E. A. Cornell & C. E. Wieman. *Nobel Lecture: Bose-Einstein condensation in a dilute gas, the first 70 years and some recent experiments*. Reviews of Modern Physics, vol. 74, no. 3, page 875, August 2002.

[Couvert 08] Antoine Couvert, T. Kawalec, G. Reinaudi & D. Guéry-Odelin. *Optimal transport of ultracold atoms in the non-adiabatic regime*. Europhysics Letters, vol. 83, no. 1, page 13001, July 2008.

[Dalfovo 99] Franco Dalfovo, Stefano Giorgini, Lev P Pitaevskii & Sandro Stringari. *Theory of Bose-Einstein condensation in trapped gases*. Reviews of Modern Physics, vol. 71, no. 3, page 463, 1999.

[Dalibard 85] Jean Dalibard & C. Cohen-Tannoudji. *Dressed-atom approach to atomic motion in laser light: the dipole force revisited*. Journal of the Optical Society of America B, vol. 2, no. November, page 1707, 1985.

[Dalibard 89] Jean Dalibard & Claude N Cohen-Tannoudji. *Laser cooling below the Doppler limit by polarization gradients: simple theoretical models*. Journal of the Optical Society of America B, vol. 6, no. 11, page 2023, 1989.

[Damski 03] B. Damski, J. Zakrzewski, L. Santos, P. Zoller & M. Lewenstein. *Atomic Bose and Anderson Glasses in Optical Lattices*. Physical Review Letters, vol. 91, no. 8, page 080403, August 2003.

[Davis 95a] K. B. Davis, M. O. Mewes, M. R. Andrews, N. J. Van Druten, D. S. Durfee, D. M. Stamper-Kurn & W. Ketterle. *Bose-Einstein Condensation in a Gas of Sodium Atoms*. Physical Review Letters, vol. 75, no. 22, page 3969, 1995.

[Davis 95b] Kendall B Davis, Marc-Oliver Mewes, Michael A Joffe, Michael R Andrews & Wolfgang Ketterle. *Evaporative cooling of sodium atoms*. Physical Review letters, vol. 74, no. 26, page 5202, June 1995.

[de Wolf 71] David A de Wolf. *Electromagnetic Reflection from an Extended Turbulent Medium : Cumulative Forward- Scatter Single-Backscatter Approximation.* IEEE transactions on Antennas and Propagation, vol. 19, page 254, 1971.

[Deissler 10] B. Deissler, M. Zaccanti, G. Roati, C. D'Errico, M. Fattori, M. Modugno, G. Modugno & M. Inguscio. *Delocalization of a disordered bosonic system by repulsive interactions.* Nature Physics, vol. 6, no. 5, page 354, April 2010.

[Di Castro 03] Carlo Di Castro & Roberto Raimondi. *Disordered Electron Systems.* In G.F. Giuliani & G. Vignale, editeurs, Proceedings of the International School of Physics "Enrico Fermi", page 259, 2003.

[Dolan 79] G. J. Dolan & D. D. Osheroff. *Nonmetallic Conduction in Thin Metal Films at Low Temperatures.* Physical Review Letters, vol. 43, no. 10, page 721, 1979.

[Dries 10] D. Dries, S. Pollack, J. Hitchcock & R. Hulet. *Dissipative transport of a Bose-Einstein condensate.* Physical Review A, vol. 82, no. 3, page 033603, September 2010.

[Economou 83] E. N. Economou & C. M. Soukolis. *Connection of localization with the problem of the bound state in a potential well.* Physical Review B, vol. 28, no. 2, page 1093, 1983.

[Edwards 08] E. E. Edwards, M. Beeler, Tao Hong & S. L. Rolston. *Adiabaticity and Localization in One-Dimensional Incommensurate Lattices.* Physical Review Letters, vol. 101, page 260402, 2008.

[Efros 84] A L Efros & B I Shklovskii. Electronic properties of doped semiconductors:. Springer, 1984.

[Einstein 27] Albert Einstein. *Quantentheorie des einatomigen idealen Gases.* In Sitzungsberichte der Preussischen Wissenschaften Akademie Berlin, 1927.

[Evers 08] Ferdinand Evers & Alexander D Mirlin. *Anderson transitions.* Reviews of Modern Physics, vol. 80, no. 4, page 1355, October 2008.

[Falco 09a] G. Falco, T. Nattermann & V. Pokrovsky. *Weakly interacting Bose gas in a random environment.* Physical Review B, vol. 80, no. 10, page 104515, September 2009.

[Falco 09b] G. M. Falco, T. Nattermann & Valery L Pokrovsky. *Localized states and interaction-induced delocalization in Bose gases with quenched disorder.* Europhysics Letters, vol. 85, page 30002, 2009.

[Fallani 08] Leonardo Fallani, Chiara Fort & Massimo Inguscio. *Bose-Einstein condensates in disordered potentials*. Advances In Atomic, Molecular, and Optical Physics, vol. 56, page 119, 2008.

[Fauquembergue 05] Marie Fauquembergue, Jean-Félix Riou, William Guerin, S. Rangwala, F. Moron, A. Villing, Yann Le Coq, Philippe Bouyer, Alain Aspect & M. Lécrivain. *Partially ferromagnetic electromagnet for trapping and cooling neutral atoms to quantum degeneracy*. Review of Scientific Instruments, vol. 76, no. 10, page 103104, 2005.

[Fauquembergue 07] Marie Fauquembergue. *Realisation d'un dispositif de condensation de Bose-Einstein et de transport d'un échantillon coherent d'atomes*. PhD thesis, Université Paris Sud XI, 2007.

[Fendley 00] Paul Fendley. *Critical points in two-dimensional replica sigma models*. In New Theoretical Approaches to Strongly Correlated, 2000.

[Fisher 89] M. P. A. Fisher, P. B. Weichman, G. Grinstein & D. S. Fisher. *Boson localization and the superfluid-insulator transition*. Physical Review B, vol. 40, no. 1, page 546, 1989.

[Fort 05] C. Fort, L. Fallani, V. Guarrera, J. Lye, M. Modugno, D. Wiersma & M. Inguscio. *Effect of Optical Disorder and Single Defects on the Expansion of a Bose-Einstein Condensate in a One-Dimensional Waveguide*. Physical Review Letters, vol. 95, no. 17, page 170410, October 2005.

[Gavish 05] Uri Gavish & Yvan Castin. *Matter-Wave Localization in Disordered Cold Atom Lattices*. Physical Review Letters, vol. 95, no. 2, page 020401, July 2005.

[Geiger 11] R. Geiger, V. Ménoret, G. Stern, N. Zahzam, P. Cheinet, B. Battelier, a. Villing, F. Moron, M. Lours, Y. Bidel, a. Bresson, a. Landragin & P. Bouyer. *Detecting inertial effects with airborne matter-wave interferometry*. Nature Communications, vol. 2, page 474, September 2011.

[Gershenson 97] M. Gershenson, Yu. Khavin, A. Mikhalchuk, H. Bozler & A. Bogdanov. *Crossover from Weak to Strong Localization in Quasi-One-Dimensional Conductors*. Physical Review Letters, vol. 79, no. 4, page 725, July 1997.

[Giamarchi 88] Thierry Giamarchi & H. J. Schulz. *Anderson localization and interaction in one-dimensional metals*. Physical Review B, vol. 37, no. 1, page 325, 1988.

[Goldenfeld 92] Nigel Goldenfeld. Lectures on Phase transitions and the renormalization group. Perseus, 1992.

[Goldman 98] Allen M Goldman & Nina Markovic. *Superconductor-Insulator Transitions in the Two-Dimensional Limit.* Physics Today, vol. 51, no. 11, page 39, 1998.

[Golubentsev 84] A A Golubentsev. *Suppression of interference effects in multiple scattering of light.* Sov. Phys. JETP, vol. 59, no. 1, page 26, 1984.

[Goodman 07] J W Goodman. Speckle phenomena in optics: theory and applications. Roberts & Co., 2007.

[Gor'kov 79] L. P. Gor'kov, A. I. Larkin & D. E. Khmel'nitskii. *Particle conductivity in a two-dimensional random potential.* JETP Letters, vol. 30, no. 4, page 228, 1979.

[Gorodnichev 94] E. E. Gorodnichev & D. B. Rogozkin. *Coherent backscattering of a light pulse by a slab of disordered medium.* Waves in Random Media, vol. 4, page 51, 1994.

[Greiner 02] Markus Greiner, Olaf Mandel, Tilman Esslinger, Theodor W Hänsch & Immanuel Bloch. *Quantum phase transition from a superfluid to a Mott insulator in a gas of ultracold atoms.* Nature, vol. 415, no. 6867, page 39, January 2002.

[Greiner 03] Markus Greiner, Cindy A Regal & Deborah S Jin. *Emergence of a molecular Bose-Einstein condensate from a Fermi gas.* Nature, vol. 426, no. 6966, page 537, December 2003.

[Grempel 82] D. R. Grempel, Shmuel Fishman & R. E. Prange. *Localization in an Incommensurate Potential: An Exactly Solvable Model.* Physical Review Letters, vol. 49, no. 11, page 833, 1982.

[Grimm 00] R. Grimm, M. Weidemüller & Y. B. Ovchinnikov. *Optical dipole traps for neutral atoms.* Advances in Atomic, Molecular and Optical Physics, vol. 42, page 95, 2000.

[Gross 08] Noam Gross & Lev Khaykovich. *All-optical production of ˆ{7}Li Bose-Einstein condensation using Feshbach resonances.* Physical Review A, vol. 77, no. 2, page 023604, February 2008.

[Guerin 06] William Guerin, Jean-Félix Riou, J.P. Gaebler, Vincent Josse, Philippe Bouyer & Alain Aspect. *Guided quasicontinuous atom laser.* Physical Review Letters, vol. 97, no. 20, page 200402, 2006.

[Gurarie 09] V. Gurarie, L. Pollet, N. V. Prokof'ev, B. V. Svistunov & M. Troyer. *Phase diagram of the disordered Bose-Hubbard model.* Physical Review B, vol. 80, no. 21, page 214519, December 2009.

[Gustavson 01] T. Gustavson, A. Chikkatur, A. Leanhardt, A. Görlitz, S. Gupta, D. Pritchard & W. Ketterle. *Transport of Bose-Einstein Condensates with Optical Tweezers.* Physical Review Letters, vol. 88, no. 2, page 020401, December 2001.

[Hadzibabic 06] Zoran Hadzibabic, Peter Krüger, Marc Cheneau, Baptiste Battelier & Jean Dalibard. *Berezinskii-Kosterlitz-Thouless crossover in a trapped atomic gas.* Nature, vol. 441, no. 7097, page 1118, June 2006.

[Hartung 08] Michael Hartung, Thomas Wellens, Cord A Müller, Klaus Richter & Peter Schlagheck. *Coherent Backscattering of Bose-Einstein Condensates in Two-Dimensional Disorder Potentials.* Physical Review Letters, vol. 101, no. 2, page 020603, July 2008.

[Hauser 92] Matt R Hauser, R. L. Weaver & J. P. Wolfe. *Internacl diffraction of Ultrasound in Crystals: Phonon Focusing at Long Wavelengths.* Physical Review Letters, vol. 68, no. 17, page 2604, 1992.

[Hess 86] H. F. Hess. *Evaporative cooling of magnetically trapped and compressed spin-polarized hydrogen.* Physical Review B, vol. 34, no. 5, page 3476, 1986.

[Hikami 80] S. Hikami, A. I. Larkin & Y. Nagaoka. *Spin–Orbit Interaction and Magnetoresistance in the Two-Dimensional Random System.* Progress of Theoretical Physics, vol. 63, no. 2, page 707, 1980.

[Hu 08] Hefei Hu, A. Strybulevych, J. H. Page, Sergey E Skipetrov & Bart A van Tiggelen. *Localization of ultrasound in a three-dimensional elastic network.* Nature Physics, vol. 4, no. 12, page 945, October 2008.

[Ioffe 60] A F Ioffe & A R Regel. Non-crystalline, amorphous and liquid electronic semiconductors. Numeéro vol.˜4. J.Wiley., 1960.

[Isichenko 92] M. B. Isichenko. *Percolation, statistical topography, and transport in random media.* Reviews of Modern Physics, vol. 64, no. 4, page 961, 1992.

[Jendrzejewski 12a] Fred Jendrzejewski, Alain Bernard, Kilian Müller, Patrick Cheinet, Vincent Josse, Marie Piraud, Luca Pezzé, Laurent

Sanchez-Palencia, Alain Aspect & Philippe Bouyer. *Three-dimensional localization of ultracold atoms in an optical disordered potential*. Nature Physics, vol. 8, no. March, page 398, 2012.

[Jendrzejewski 12b] Fred Jendrzejewski, Kilian Müller, Jeremie Richard, Aditya Date, Thomas Plisson, Philippe Bouyer, Alain Aspect & Vincent Josse. *Coherent Backscattering of Ultracold Atoms*. Physical Review Letters, vol. 109, no. 19, page 195302, November 2012.

[John 88] Sajeev John & Raghavan Rangarajan. *Optimal structures for classical wave localization: An alternative to the Ioffe-Regel criterion*. Physical Review B, vol. 38, no. 14, page 10101, 1988.

[Kaas 08] B. Kaas, Bart A van Tiggelen & A Lagendijk. *Anisotropy and Interference in Wave Transport: An Analytic Theory*. Physical Review Letters, vol. 100, no. 12, page 4, March 2008.

[Kagan 96] Y. Kagan, E. L. Surkov & G .V. Shlyapnikov. *Evolution of a Bose-condensed gas under variations of the confining potential*. Physical Review A, vol. 54, no. 3, page 1753, 1996.

[Karbasi 12] Salman Karbasi, Craig R Mirr, Ryan J Fraizer, Gandomkar Yarandi, Karl W Koch & Arash Mafi. *Detailed investigation of the impact of the fiber design parameters on the transverse Anderson localization of light in disordered optical fibers*. Optics Express, vol. 20, no. 17, page 18692, 2012.

[Karpiuk 12] T. Karpiuk, N. Cherroret, K. L. Lee, Benoît Grémaud, Cord A. Müller & C. Miniatura. *Coherent multiple forward scattering peak unveiled by Anderson localization*. arXiv, page 1204.3451, 2012.

[Katsumoto 87] Shingo Katsumoto, Fumio Komori, Naokatsu Sano & Shunichi Kobayashi. *Fine Tuning of Metal-Insulator Transition in Al_{0.3}Ga_{0.7}As Using Persistent Photoconductivity*. Journal of the Physical Society of Japan, vol. 56, no. 7, pages 2259–2262, 1987.

[Ketterle 99] Wolfgang Ketterle, D. S. Durfee & D. M. Stamper-Kurn. *Making, probing and understanding Bose-Einstein condensates*. In Proceedings of the International School of Physics "Enrico Fermi", page 67, 1999.

[Ketterle 02] Wolfgang Ketterle. *Nobel lecture : When atoms behave as waves : Bose-Einstein condensation and the atom laser*. Re-

views of Modern Physics, vol. 74, no. October, page 1131, 2002.

[Kinoshita 04] Toshiya Kinoshita, Trevor Wenger & David S Weiss. *Observation of a one-dimensional Tonks-Girardeau gas.* Science, vol. 305, no. 5687, page 1125, August 2004.

[Kinoshita 05] Toshiya Kinoshita, Trevor Wenger & David Weiss. *All-optical Bose-Einstein condensation using a compressible crossed dipole trap.* Physical Review A, vol. 71, no. 1, page 011602(R), January 2005.

[Kirkpatrick 73] Scott Kirkpatrick. *Percolation and conduction.* Reviews of Modern Physics, vol. 45, no. 4, page 574, 1973.

[Kondov 11] S. S. Kondov, W. R. McGehee, J. J. Zirbel & B. DeMarco. *Three-Dimensional Anderson Localization of Ultracold Matter.* Science, vol. 334, no. 6052, page 66, October 2011.

[Kramer 93] Bernhard Kramer & Angus Mackinnon. *Localization: theory and experiment.* Reports on Progress in Physics, vol. 56, no. June, page 1469, 1993.

[Kuga 84] Yasuo Kuga & Akira Ishimaru. *Retroreflectance from a dense distribution of spherical particles.* Journal of the Optical Society of America A, vol. 1, no. 8, page 831, August 1984.

[Kuhn 07] R. C. Kuhn, O. Sigwarth, C. Miniatura, D. Delande & Cord A. Müller. *Coherent matter wave transport in speckle potentials.* New Journal of Physics, vol. 9, no. 6, page 161, June 2007.

[Labeyrie 99] G. Labeyrie, F. De Tomasi, J. C. Bernard, Cord A. Müller, C. Miniatura & R. Kaiser. *Coherent backscattering of light by cold atoms.* Physical Review Letters, vol. 83, no. 25, page 5266, 1999.

[Labeyrie 12] Guillaume Labeyrie, Tomasz Karpiuk, Benoît Grémaud, Christian Miniatura & Dominique Delande. *Coherent backscattering of a dilute Bose-Einstein condensate.* Arxiv, page 1206.0845, 2012.

[Lagendijk 09] A. Lagendijk, Bart van Tiggelen & Diederik S. Wiersma. *Fifty years of Anderson localization.* Physics Today, vol. 62, no. 8, page 24, 2009.

[Lahini 08] Yoav Lahini, Assaf Avidan, Francesca Pozzi, Marc Sorel, Roberto Morandotti, Demetrios Christodoulides & Yaron Silberberg. *Anderson Localization and Nonlinearity in One-Dimensional Disordered Photonic Lattices.* Physical Review Letters, vol. 100, no. 1, page 013906, January 2008.

[Landauer 70] Rolf Landauer. *Electrical resistance of disordered one-dimensional lattices.* Philosophical Magazine, vol. 21, no. 172, pages 863–867, 1970.

[Langer 66] J. S. Langer & T. Neal. *Breakdown of the concentration expansion for the impurity resistivity of metals.* Physical Review Letters, vol. 16, no. 22, page 984, 1966.

[Larose 04] E. Larose, L. Margerin, B. van Tiggelen & M. Campillo. *Weak Localization of Seismic Waves.* Physical Review Letters, vol. 93, no. 4, page 048501, July 2004.

[Laurent 06] Ph. Laurent, M. Abgrall, Ch. Jentsch, P. Lemonde, G. Santarelli, A. Clairon, I. Maksimovic, S. Bize, Ch. Salomon, D. Blonde, J.F. Vega, O. Grosjean, F. Picard, M. Saccoccio, M. Chaubet, N. Ladiette, L. Guillet, I. Zenone, Ch. Delaroche & Ch. Sirmain. *Design of the cold atom PHARAO space clock and initial test results.* Applied Physics B, vol. 84, no. 4, page 683, August 2006.

[Laurent 07] David Laurent, Olivier Legrand, Patrick Sebbah, Christian Vanneste & Fabrice Mortessagne. *Localized Modes in a Finite-Size Open Disordered Microwave Cavity.* Physical Review Letters, vol. 99, no. 25, page 253902, December 2007.

[Lee 85] Patrick A. Lee & T.V. Ramakrishnan. *Disordered electronic systems.* Reviews of Modern Physics, vol. 57, no. 2, page 287, 1985.

[Leggett 01] A. J. Leggett. *Bose-Einstein condensation in the alkali gases: Some fundamental concepts.* Reviews of Modern Physics, vol. 73, no. 2, page 307, 2001.

[Lemarié 09] G. Lemarié, B. Grémaud & D. Delande. *Universality of the Anderson transition with the quasiperiodic kicked rotor.* Europhysics Letters, vol. 87, no. 3, page 37007, August 2009.

[Lemarié 10] Gabriel Lemarié, Hans Lignier, Dominique Delande, Pascal Szriftgiser & Jean Garreau. *Critical State of the Anderson Transition: Between a Metal and an Insulator.* Physical Review Letters, vol. 105, no. 9, page 090601, August 2010.

[Lenke 97] R. Lenke & G. Maret. *Coherent backscattering of light in multiple scattering media.* Progress in Colloid & Polymer Science, vol. 104, no. 1, page 126, December 1997.

[Lenke 00] R. Lenke & G. Maret. *Magnetic field effects on coherent backscattering of light.* European Physical Journal B, vol. 17, page 171, 2000.

[Lett 88] Paul D Lett, Richard N Watts, Christoph I Westbrook, William D Phillips, Phillip L. Gould & H. Metcalf. *Observation of atoms laser cooled below the Doppler limit.* Physical Review Letters, vol. 61, no. 2, page 169, 1988.

[Lin 09] Y.-J. Lin, R. L. Compton, K. Jiménez-García, J. V. Porto & I. B. Spielman. *Synthetic magnetic fields for ultracold neutral atoms.* Nature, vol. 462, no. 7273, page 628, December 2009.

[Lin 11] Y.-J. Lin, K. Jiménez-García & I. B. Spielman. *Spin-orbit-coupled Bose-Einstein condensates.* Nature, vol. 471, no. 7336, page 83, March 2011.

[Lopatin 02] A. V. Lopatin & V. M. Vinokur. *Thermodynamics of the Superfluid Dilute Bose Gas with Disorder.* Physical Review Letters, vol. 88, no. 23, page 235503, May 2002.

[Lopez 12] Matthias Lopez, Jean-François Clément, Pascal Szriftgiser, Jean Claude Garreau & Dominique Delande. *Experimental Test of Universality of the Anderson Transition.* Physical Review Letters, vol. 108, no. 9, page 095701, February 2012.

[Lugan 07] P. Lugan, D. Clément, P. Bouyer, A. Aspect, M. Lewenstein & L. Sanchez-Palencia. *Ultracold Bose Gases in 1D Disorder: From Lifshits Glass to Bose-Einstein Condensate.* Physical Review Letters, vol. 98, no. 17, page 170403, April 2007.

[Ma 76] Shang-keng Ma. Modern theory of critical phenomena. Perseus, 1976.

[Massignan 06] Pietro Massignan & Yvan Castin. *Three-dimensional strong localization of matter waves by scattering from atoms in a lattice with a confinement-induced resonance.* Physical Review A, vol. 74, no. 1, page 013616, July 2006.

[Masuhara 88] Naoto Masuhara, J. M. Doyle, J. C. Sandberg, Daniel Kleppner, T.J. Greytak, H. F. Hess & G.P. Kochanski. *Evaporative cooling of spin-polarized atomic hydrogen.* Physical Review Letters, vol. 61, no. 8, page 935, 1988.

[Moore 94] F. L. Moore, J. C. Robinson, C. Bharucha, P. E. Williams & M. G. Raizen. *Observation of Dynamical Localization in Atomic Momentum Transfer : A New Testing Ground for Quantum Chaos.* Physical Review Letters, vol. 73, no. 22, page 2974, 1994.

[Mott 61] N F Mott & W D Twose. *The theory of impurity conduction.* Advances in Physics, vol. 10, no. 38, pages 107–163, 1961.

[Müller 09] Cord A Müller & Dominique Delande. *Disorder and interference : localization phenomena*. In Les Houches 2009 - Session XCI: Ultacold Gases and Quantum Information, 2009.

[Okamoto 96] Takashi Okamoto & Toshimitsu Asakura. *Enhanced backscattering of partially coherent light*. Optics Letters, vol. 21, no. 6, page 369, March 1996.

[Paredes 04] B. Paredes, A. Widera, V. Murg, O. Mandel, Simon Fölling, Ignacio Cirac, G. V. Shlyapnikov, Theodor W. Hänsch & Immanuel Bloch. *Tonks – Girardeau gas of ultracold atoms in an optical lattice*. Nature, vol. 429, page 277, 2004.

[Pasienski 10] M. Pasienski, D. McKay, M. White & Brian Demarco. *A disordered insulator in an optical lattice*. Nature Physics, vol. 6, no. 7, page 677, July 2010.

[Paul 07] T. Paul, P. Schlagheck, P. Leboeuf & N. Pavloff. *Superfluidity versus Anderson Localization in a Dilute Bose Gas*. Physical Review Letters, vol. 98, no. 21, page 210602, May 2007.

[Petrich 95] Wolfgang Petrich, Michael H. Anderson, Jason R. Ensher & Eric A. Cornell. *Stable, Tightly Confining Magnetic Trap for Evaporative Cooling of Neutral Atoms*. Physical Review Letters, vol. 74, no. 17, page 3352, 1995.

[Pezzé 11] L. Pezzé, M. Robert-de Saint-Vincent, T. Bourdel, J.-P. Brantut, B. Allard, T. Plisson, A. Aspect, P. Bouyer & L. Sanchez-Palencia. *Regimes of classical transport of cold gases in a two-dimensional anisotropic disorder*. New Journal of Physics, vol. 13, no. 9, page 095015, September 2011.

[Phillips 82] William D. Phillips & Harold Metcalf. *Laser Deceleration of an Atomic Beam*. Physical Review Letters, vol. 48, no. 9, page 596, 1982.

[Phillips 98] W. D. Phillips. *Laser cooling and trapping of neutral atoms*. Reviews of Modern Physics, vol. 70, no. 3, page 721, 1998.

[Pilati 08] S. Pilati, Stefano Giorgini & N. V. Prokof'ev. *Critical Temperature of Interacting Bose Gases in Two and Three Dimensions*. Physical Review Letters, vol. 100, no. 14, page 140405, April 2008.

[Pilati 10] S. Pilati, Stefano Giorgini, Michele Modugno & N. V. Prokof'ev. *Dilute Bose gas with correlated disorder: a path integral Monte Carlo study*. New Journal of Physics, vol. 12, no. 7, page 073003, July 2010.

[Piraud 12a] Marie Piraud, Alain Aspect & Laurent Sanchez-Palencia. *Anderson localization of matter waves in tailored disordered potentials*. Physical Review A, vol. 85, page 063611, April 2012.

[Piraud 12b] Marie Piraud, Luca Pezzé & Laurent Sanchez-Palencia. *Matter wave transport and Anderson localization in anisotropic three-dimensional disorder*. Europhysics Letters, vol. 99, no. September, page 50003, 2012.

[Polkovnikov 11] Anatoli Polkovnikov & Alessandro Silva. *Colloquium : Nonequilibrium dynamics of closed interacting quantum systems*. Reviews of Modern Physics, vol. 83, no. September, page 863, 2011.

[Pollet 09] Lode Pollet, N. V. Prokof'ev, B. V. Svistunov & Matthias Troyer. *Absence of a Direct Superfluid to Mott Insulator Transition in Disordered Bose Systems*. Physical Review Letters, vol. 103, no. 14, page 140402, September 2009.

[Raab 87] E. L. Raab, M. Prentiss, Alex Cable, Steven Chu & David E. Pritchard. *Trapping of Neutral Sodium Atoms with Radiation Pressure*. Physical Review Letters, vol. 59, no. 23, page 2631, 1987.

[Rammer 04] J Rammer. Quantum Transport Theory. Frontiers in Physics. Westview Press, 2004.

[Reppy 92] John D Reppy. *Superfluid helium in porous media*. Journal of Low Temperature Physics, vol. 87, no. 3, page 205, 1992.

[Riou 06] Jean-Félix Riou. *Etudes des propriétés de propagation d'un laser à atomes*. PhD thesis, Université Paris Sud 11, 2006.

[Roati 08] Giacomo Roati, Chiara D'Errico, Leonardo Fallani, Marco Fattori, Chiara Fort, Matteo Zaccanti, Giovanni Modugno, Michele Modugno & Massimo Inguscio. *Anderson localization of a non-interacting Bose-Einstein condensate.* Nature, vol. 453, no. 7197, page 895, June 2008.

[Robert-de Saint-Vincent 10] M. Robert-de Saint-Vincent, J.-P. Brantut, B. Allard, T. Plisson, L. Pezzé, L. Sanchez-Palencia, A. Aspect, T. Bourdel & P. Bouyer. *Anisotropic 2D Diffusive Expansion of Ultracold Atoms in a Disordered Potential*. Physical Review Letters, vol. 104, no. 22, page 220602, June 2010.

[Roscilde 08] Tommaso Roscilde. *Bosons in one-dimensional incommensurate superlattices*. Physical Review A, vol. 77, no. 6, page 063605, June 2008.

[Rosenbaum 83] T. F. Rosenbaum, R. F. Milligan, M. A. Paalanen, G. A. Thomas, R. N. Bhatt & W. Lin. *Metal-instulator transition in a doped semiconductor.* Physical Review B, vol. 27, no. 12, pages 7509–7523, 1983.

[Roth 03] Robert Roth & Keith Burnett. *Phase diagram of bosonic atoms in two-color superlattices.* Physical Review A, vol. 68, no. 2, page 023604, August 2003.

[Roux 08] G. Roux, T. Barthel, I. McCulloch, C. Kollath, U. Schollwöck & T. Giamarchi. *Quasiperiodic Bose-Hubbard model and localization in one-dimensional cold atomic gases.* Physical Review A, vol. 78, no. 2, page 023628, August 2008.

[Sachdev 11] Subir Sachdev. Quantum Phase Transitions. Cambridge Univ Pr, 2011.

[Sackett 06] C. A. Sackett. *Limits on weak magnetic confinement of neutral atoms.* Physical Review A, vol. 73, no. 1, page 013626, January 2006.

[Sanchez-Palencia 07] Laurent Sanchez-Palencia, David Clément, Pierre Lugan, Philippe Bouyer, G. V. Shlyapnikov & Alain Aspect. *Anderson Localization of Expanding Bose-Einstein Condensates in Random Potentials.* Physical Review Letters, vol. 98, no. 21, page 210401, May 2007.

[Sanchez-Palencia 08] L. Sanchez-Palencia, D. Clément, P. Lugan, P. Bouyer & A. Aspect. *Disorder-induced trapping versus Anderson localization in Bose–Einstein condensates expanding in disordered potentials.* New Journal of Physics, vol. 10, no. 4, page 045019, April 2008.

[Sanchez-Palencia 10] Laurent Sanchez-Palencia & Maciej Lewenstein. *Disordered quantum gases under control.* Nature Physics, vol. 6, no. 2, page 87, 2010.

[Schulte 05] T. Schulte, S. Drenkelforth, J. Kruse, W. Ertmer, J. Arlt, K. Sacha, J. Zakrzewski & M. Lewenstein. *Routes Towards Anderson-Like Localization of Bose-Einstein Condensates in Disordered Optical Lattices.* Physical Review Letters, vol. 95, no. 17, page 170411, October 2005.

[Schwartz 07] Tal Schwartz, Guy Bartal, Shmuel Fishman & Mordechai Segev. *Transport and Anderson localization in disordered two-dimensional photonic lattices.* Nature, vol. 446, no. March, page 52, March 2007.

[Shapiro 12] Boris Shapiro. *Cold atoms in the presence of disorder.* Journal of Physics A: Mathematical and Theoretical, vol. 45, no. 14, page 143001, April 2012.

[Sharvin 81] D. Yu. Sharvin & Yu. V. Sharvin. *Magnetic-flux quantization in a cylindrical film of a normal metal.* JETP Letters, vol. 34, no. 5, page 272, 1981.

[Shklovskii 08] B. I. Shklovskii. *Superfluid-insulator transition in "Dirty" ultracold Fermi gas.* Semiconductors, vol. 42, no. 8, page 909, August 2008.

[Skal 73] A. S. Skal, B. I. Shklovskii & A. L. Efros. *Percolation level in a three-dimensional random potential.* JETP Letters, vol. 17, page 377, 1973.

[Skipetrov 08] Sergey E Skipetrov, A. Minguzzi, Bart A. van Tiggelen & Boris Shapiro. *Anderson Localization of a Bose-Einstein Condensate in a 3D Random Potential.* Physical Review Letters, vol. 100, no. 16, page 165301, April 2008.

[Slevin 99] Keith Slevin & Tomi Ohtsuki. *Corrections to Scaling at the Anderson Transition.* Physical Review Letters, vol. 82, no. 2, page 382, January 1999.

[Smith 79] L N Smith & C J Lobb. *Percolation in two-dimensional conductor-insulator networks with controllable anisotropy.* Physical Review B, vol. 20, no. 9, pages 3653–3658, November 1979.

[Stauffer 94] Dietrich Stauffer & Amnon Aharony. Introduction To Percolation Theory. Taylor & Francis, 1994.

[Steck 06] DA Steck. *Rubidium 87 D line data*, 2006.

[Stewart 08] J. T. Stewart, J. P. Gaebler & D. S. Jin. *Using photoemission spectroscopy to probe a strongly interacting Fermi gas.* Nature, vol. 454, page 744, August 2008.

[Störzer 06] Martin Störzer, Peter Gross, Christof Aegerter & Georg Maret. *Observation of the Critical Regime Near Anderson Localization of Light.* Physical Review Letters, vol. 96, no. 6, page 063904, February 2006.

[Strinati 89] G. Strinati, C. Castellani & C. Di Castro. *Kinetic equation for stongly disordered systems: Noninteraction electrons.* Physical Review B, vol. 40, no. 18, page 12237, 1989.

[Thomas 04] Nicholas R. Thomas, Niels Kjæ rgaard, Paul S. Julienne & Andrew C. Wilson. *Imaging of s and d Partial-Wave Interference in Quantum Scattering of Identical Bosonic Atoms.* Physical Review Letters, vol. 93, no. 17, page 173201, October 2004.

[Thouless 77] D. J. Thouless. *Maximum Metallic Resistance in Thin Wires*. Physical Review Letters, vol. 39, no. 18, page 1167, 1977.

[Tourin 97] Arnaud Tourin, Arnaud Derode, Philippe Roux, Bart van Tiggelen & Mathias Fink. *Time-Dependent Coherent Backscattering of Acoustic Waves*. Physical Review Letters, vol. 79, no. 19, page 3637, November 1997.

[Tsang 84] L Tsang & A Ishimaru. *Backscattering enhancement of random discrete scatterers*. Journal of the Optical Society of America A, vol. 1, no. 8, page 836, 1984.

[van Albada 85] M. P. van Albada & A. Lagendijk. *Observation of Weak Localization in a Random Medium*. Physical Review Letters, vol. 55, no. 24, page 2692, 1985.

[Van Den Dries 81] L. Van Den Dries, C. Van Haesendonck, Y Bruynseraede & G. Deutscher. *Two-Dimensional Localization in Thin Copper Films*. Physical Review Letters, vol. 46, page 565, 1981.

[van Tiggelen 90] Bart A van Tiggelen, Ad Lagendijk & A Tip. *Multiple-scattering effects for the propagation of light in 3D slabs*. Journal of Physics: Condensed Matter, vol. 2, page 7653, 1990.

[van Tiggelen 99] Bart A van Tiggelen. *Localization of Waves*. In Jean-Pierre Fouque, editeur, Diffusive Waves in Complex Media, Numéro 531 de NATO ASI series: Mathematical and physical sciences NATO Advanced Science Institutes Series Volume 531 de NATO Science Series C, page 459. Kluwer Academic Publishers, 1999.

[van Zoest 10] T. van Zoest, N. Gaaloul, Y. Singh, H. Ahlers, W. Herr, S. T. Seidel, W. Ertmer, E. Rasel, M. Eckart, E. Kajari, S. Arnold, G. Nandi, W. P. Schleich, R. Walser, A. Vogel, K. Sengstock, K. Bongs, W. Lewoczko-Adamczyk, M. Schiemangk, T. Schuldt, A. Peters, T. Könemann, H. Müntinga, C. Lämmerzahl, H. Dittus, T. Steinmetz, T. W. Hänsch & J. Reichel. *Bose-Einstein condensation in microgravity*. Science, vol. 328, no. 5985, page 1540, June 2010.

[Vollhardt 80] Dieter Vollhardt & Peter Wölfle. *Anderson Localization in d < 2 Dimensions: A Self-Consistent Diagrammatic Theory*. Physical Review Letters, vol. 45, no. 10, page 842, 1980.

[Vollhardt 92] Dieter Vollhardt & Peter Wölfle. *Self-consistent Theory of Anderson Localization*. In Electronic Phase Transitions. 1992.

[Vreeker 88] R. Vreeker, Meint P. van Albada, R. Sprik & Ad Lagendijk. *Femtosecond time-resolved measurements of weak localization of light.* Physics Letters A, vol. 132, no. 1, page 51, 1988.

[Vynck 12] Kevin Vynck, Matteo Burresi, Francesco Riboli & Diederik S. Wiersma. *Disordered Optical Modes for Photon Management.* arXiv, page 1202.4601, 2012.

[Walraven 10] J. Walraven. *Elements of Quantum Gases : Thermodynamic and Collisional Properties of Trapped Atomic Gases.* In Les Houches - predoc lectures 2010, page 207, 2010.

[Watson 69] Kenneth M Watson. *Multiple Scattering of Electromagnetic Waves in an Underdense Plasma.* Journal of Mathematical Physics, vol. 10, page 688, 1969.

[Webb 85] R. A. Webb, S. Washburn, C. P. Umbach & R. B. Laibowitz. *Observation of h/e Aharonov-Bohm Oscillations in Normal-Metal Rings.* Physical Review Letters, vol. 54, no. 25, page 2696, 1985.

[Wegner 76] Franz J Wegner. *Electrons in Disordered Systems . Scaling Near the Mobility Edge.* Zeitschrift für Physik B, vol. 25, page 327, 1976.

[Weichman 08] Peter B Weichman. *Dirty Bosons: Twenty Years Later.* Modern Physics Letters B, 2008.

[Weinrib 82] Abel Weinrib. *Percolation threshold of a two-dimensional continuum system.* Physical Review B, vol. 26, no. 3, page 1352, 1982.

[White 09] M. White, M. Pasienski, D. McKay, S. Q. Zhou, D. Ceperley & B. DeMarco. *Strongly Interacting Bosons in a Disordered Optical Lattice.* Physical Review Letters, vol. 102, no. 5, page 055301, February 2009.

[Wiersma 95] Diederik S Wiersma, M. P. van Albada, Bart A. van Tiggelen & Ad Lagendijk. *Experimental Evidence for Recurrent Multiple Scattering Events of Light in Disordered Media.* Physical Review Letters, vol. 74, no. 21, page 4193, 1995.

[Wiersma 97] D. S. Wiersma, Paolo Bartolini, A Lagendijk & Roberto Righini. *Localization of light in a disordered medium.* Nature, vol. 390, no. 6661, page 671, 1997.

[Wolf 85] P.E. Wolf & Georg Maret. *Weak Localization and Coherent Backscattering of Photons in Disordered Media.* Physical Review Letters, vol. 55, no. 24, page 2696, 1985.

[Yedjour 10] A. Yedjour & Bart A. van Tiggelen. *Diffusion and localization of cold atoms in 3D optical speckle.* The European Physical Journal D, vol. 59, no. 2, page 249, June 2010.

[Zakrzewski 09] Jakub Zakrzewski & Dominique Delande. *Breakdown of adiabaticity when loading ultracold atoms in optical lattices.* Physical Review A, vol. 80, page 013602, 2009.

[Zallen 71] Richard Zallen & Harvey Scher. *Percolation on a Continuum and the Localization-Delocalization Transition in Amorphous Semiconductors.* Physical Review B, vol. 4, no. 12, page 4471, 1971.

[Zhang 90] Zhao-Qing Zhang, Qian-Jiang Chu, Weige Xue & Ping Sheng. *Anderson localization in anisotropic random media.* Physical Review B, vol. 42, no. 7, page 4613, 1990.

Résumé

Dans cette thèse, nous étudions le transport quantique d'ondes de matière avec des atomes ultrafroids. Ces systèmes d'atomes ultrafroids fournissent un très bon contrôle et une grande flexibilité pour les paramètres du système tels que les interactions, sa dimensionnalité et les potentiels externes. Cela les rend un excellent outil pour l'étude de plusieurs concepts fondamentaux de la physique de la matière condensée.

Nous nous concentrons sur le transport quantique dans les milieux désordonnés. Il diffère du transport classique par le rôle fondamental joué par les phénomènes d'inférence, qui peuvent éventuellement conduire à la suppression du transport; connu comme la Localisation d'Anderson. Nous étudions l'expansion d'un condensat de Bose-Einstein dans un désordre fort et montrons des signes de localisation d'atomes ultrafroids à trois dimensions.

Dans la dernière partie de ce manuscrit, nous discutons l'observation de la rétrodiffusion cohérente d'atomes ultrafroids, ce qui est un signal direct du rôle de la cohérence quantique dans le transport quantique dans les milieux désordonnés. Nous observons l'évolution temporelle de la distribution d'impulsions d'un nuage de atomes ultrafroids, lancé avec une distribution de vitesse étroite dans un potentiel désordonné. Un pic emerge dans le sens rétrograde, correspondant au signal de CBS.

Mots clés

Atomes froids- Onde de matière - Condensat de Bose-Einstein - Désordre - Localisation d'Anderson - Transport quantique - Rétrodiffusion coherente

Abstract

In this thesis we study the quantum transport of matter waves with ultracold atoms. Such ultracold atom systems provide a very good control and a high flexibility of the parameters of the systems like the interactions, its dimensionality and the external potentials. This makes them a great tool for the investigation of several fundamental concepts of condensed matter physics.

We focus on the quantum transport in disordered media. It differs to classical transport by the fundamental role played by inference phenomena, which can eventually lead to the suppression of transport; known as Anderson Localization. Observing the expansion of a Bose-Einstein condensate in a strong light disorder, we show evidence for Localization of ultracold atoms in three dimensions.

In the last part of this manuscript we discuss the observation of Coherent Backscattering of ultracold atoms, which is a direct signal of the role of quantum coherence in quantum transport in disordered media. We observe the time evolution of the momentum distribution of a cloud of ultra-cold atoms, launched with a narrow velocity distribution in a disordered potential. A peak emerges in in the backwards direction, corresponding to the CBS signal.

Key words

Cold Atoms - Matter wave - Bose-Einstein condensate - Disorder - Anderson Localization - Quantum transport - Coherent backscattering